



LUND UNIVERSITY

A Study of Number-Ratio Fluctuations in Gold-Gold Interactions at $\sqrt{s_{NN}}=200$ GeV

Haslum, Eva

2011

[Link to publication](#)

Citation for published version (APA):

Haslum, E. (2011). *A Study of Number-Ratio Fluctuations in Gold-Gold Interactions at $\sqrt{s_{NN}}=200$ GeV*. [Doctoral Thesis (monograph), Particle and nuclear physics].

Total number of authors:

1

General rights

Unless other specific re-use rights are stated the following general rights apply:

Copyright and moral rights for the publications made accessible in the public portal are retained by the authors and/or other copyright owners and it is a condition of accessing publications that users recognise and abide by the legal requirements associated with these rights.

- Users may download and print one copy of any publication from the public portal for the purpose of private study or research.
- You may not further distribute the material or use it for any profit-making activity or commercial gain
- You may freely distribute the URL identifying the publication in the public portal

Read more about Creative commons licenses: <https://creativecommons.org/licenses/>

Take down policy

If you believe that this document breaches copyright please contact us providing details, and we will remove access to the work immediately and investigate your claim.

LUND UNIVERSITY

PO Box 117
221 00 Lund
+46 46-222 00 00

**A Study of Number-Ratio Fluctuations
in Gold-Gold Interactions
at $\sqrt{s_{\text{NN}}} = 200 \text{ GeV}$**

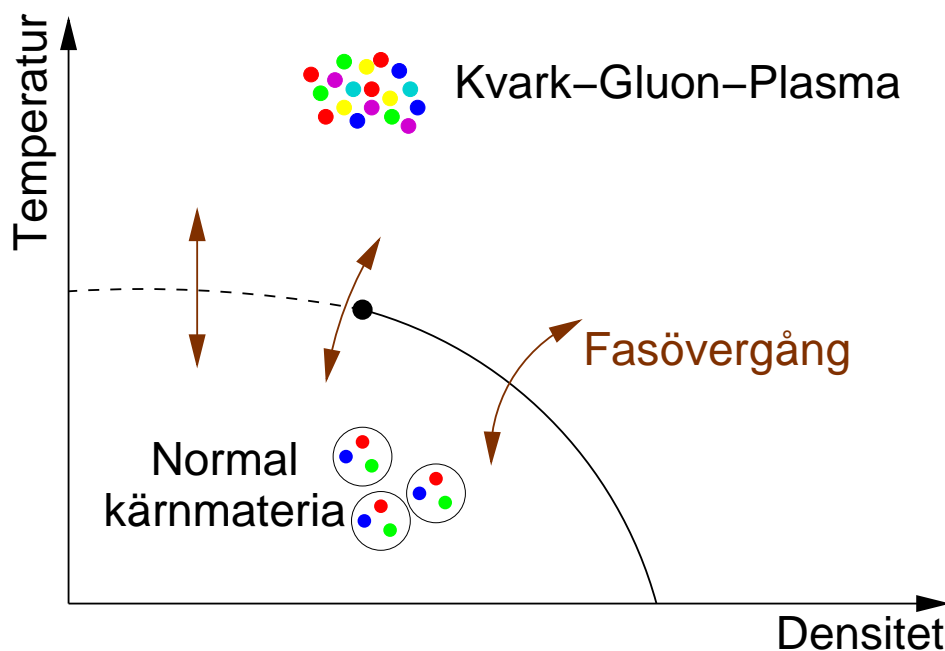
Eva Haslum

DEPARTMENT OF PHYSICS
LUND UNIVERSITY, 2011

Populärvetenskaplig sammanfattning

Kollisioner med tunga joner, så som guld, används i försök till att återskapa de förhållanden som fanns i universum strax efter Big bang genom att i experiment skapa så hög energitäthet som möjligt. Detta skulle göra det möjligt att studera den form av materia som universum bestod av vid den tidpunkten och därmed öka vår kunskap om de grundläggande fysiska lagarna. De tunga jonerna tillförs energi genom att accelereras upp i hastigheter mycket nära ljusets. När de sedan tillåts kollidera koncentreras deras rörelseenergi och massa i kollisionspunkten.

Nedan visas ett diagram som sammanfattar forskningsfältet väldigt bra.



Det är ett fasdiagram för kärnmateria. Som synes är det en väldigt schematisk bild. Dels är det ett försök att förenkla den så mycket som möjligt men

det är även så att vi faktiskt inte vet så mycket om detaljerna. På y-axeln har vi temperatur och på x-axeln densitet, vilket avser nettodensiteten av materia och antimateria. Om det finns lika många partiklar som antipartiklar befinner sig materien längst till vänster i diagrammet oavsett hur stor partikeltätheten är. Det viktigaste i det här diagrammet är kurvan som separerar materien i två olika faser. Precis som vatten har de olika faserna is, vätska och ånga, har kärnmaterien också olika faser.

Kärnmateriens minsta beståndsdelar är kvarkarna som, förutom elektrisk laddning, även bär på något som kallas färgladdning. Under kurvan är kvarkarna alltid uppbundna av *den starka kraften* i färglösa partiklar, exempelvis de protoner och neutroner som bygger upp alla atomkärnor. Det gör att vi normalt inte kan se, eller mäta, kvarkarna, eftersom den starka kraften, som namnet anger, är mycket stark. En egenhet hos den starka kraften är att den blir starkare med ökat avstånd och minskar i styrka vid små avstånd, till skillnad mot vad vi är vana vid med andra, mer vardagliga, krafter så som elektromagnetism eller gravitation. Om temperaturen är väldigt hög bildas det så många kvark-antikvarkpar att avståndet mellan kvarkarna blir tillräckligt litet för att den starka kraften ska tappa i styrka. Kvarkarna uppträder då som fria. Detsamma sker om trycket är så högt att de partiklar som kvarkarna är bundna i börjar överlappa. Då sker en fasövergång, varvid materien passerar över skiljelinjen i diagrammet för att infinna sig i den fas som kallas *kvark-gluon-plasma*. Det är alltså ett färgladdat plasma av kvarkar och gluoner. Gluonerna är de som förmedlar den starka kraften. Detta är det tillstånd som universum befann sig i upp till några miljondels sekunder efter Big bang och det är det vi försöker återskapa i våra experiment.

Fasövergångar kan vara mer eller mindre våldsamma med följd att det kan uppstå fluktuationer i fördelningen av partiklar som materien består av. I exemplet med vatten syns detta tydligt om man studerar kokande vatten i en kastrull. I vattnet bildas bubblor av ånga i varierande storlekar. Hur stora dessa fluktuationer blir beror på vilken typ av fasövergång det är frågan om. Det är sådana fluktuationer som avhandlas här. Förhoppningen är att vi ska lära oss något om detaljerna i diagrammet ovan och därigenom få bättre förståelse för kvarkarna, gluonerna och de lagar som styr deras växelverkan genom den starka kraften. Då kanske vi också kan närma oss svaret på frågan om livet, universum och allting.

Preface

Outline of this thesis

The first part of this thesis gives a general introduction to particle physics, high-energy heavy-ion collisions and fluctuations, covered by chapter 1 and 2. This is followed by a detailed description of the observable used for the study of dynamical fluctuations in particle number ratios, with a Monte Carlo simulation study of the properties of the observable itself and results from a simulation study where an implementation of a physical model of heavy-ion collisions is used, in chapter 3 and 4. The third part deals with the analysis of experimental data. Chapter 5 gives an overview of the physical experiment and its accelerator complex, while the details of the analysis are provided in chapter 6 and 7. The results are discussed in chapter 8. Appended at the end is our theoretical paper that describes thoroughly the observable used in this thesis.

Contribution by the author

During the course of my PhD studies I have participated in the operation of the PHENIX experiment. As a shift taker during data acquisition I have been responsible for monitoring and operation of the high-voltage and low-voltage systems and monitoring of gas systems as well as monitoring on-line data quality and running offline data transfer processes. In the role of subsystem expert of the Pad Chambers I participated, under the guidance of Anders Oskarsson and Hans-Åke Gustafsson from the Lund University division of experimental high-energy physics, EHEP, in diagnostics and maintenance of these detectors and their read-out system.

I developed and implemented the Monte Carlo simulation program with input from Evert Stenlund, also at Lund EHEP, regarding the statistical formalism. This was part of the simulation effort and study of the observable that I use in this analysis, which resulted in a publication, entitled

”Number-ratio fluctuations in high-energy particle production” [50], in collaboration with P. Christiansen and E. Stenlund.

In the analysis of simulated and real data of Gold-Gold collisions I made use of the PHENIX data analysis framework, which provides subroutines for looping through data files, the events therein and the tracks in the events. I have also benefited from calibrations of the data performed by various other members of the PHENIX collaboration.

Acknowledgements

I would like to thank my supervisors, Anders Oskarsson and Evert Stenlund, for their continuous support and patience during the course of my PhD studies that lasted considerably longer than I originally planned. I greatly appreciate the efforts you made to share your knowledge with me and I hope that I have absorbed at least some of it! I am also lucky to have had the opportunity to benefit, if only for a couple of years, from the expertise of Hans-Åke Gustafsson whose tragical death was a great loss to all of us. I am very thankful to Peter Christiansen for all his suggestions and valuable input. Great thanks to all other individuals at the department of Experimental High-Energy Physics who have assisted me in one way or another.

Of course I am also very grateful to all the current and former members of the PHENIX collaboration who have contributed to critical discussions regarding my analysis and whose work I have benefited from.

Last, but not least, I would like to thank my closest family, especially Sandy and my two wonderful little children, Edith and Auguste, for always being a ”*source de joie*”.

Contents

1	Introduction	7
1.1	The standard model	7
1.2	The quark-gluon plasma	10
1.3	High-energy heavy-ion collisions	11
1.4	The equation of state	13
1.5	Terminology	15
1.6	Signals of the quark-gluon plasma	16
2	Studies of fluctuations	25
2.1	Thermodynamics	26
2.2	Phase transitions	26
2.3	Previous PHENIX results on fluctuations	27
3	Dynamical fluctuations in particle production	33
3.1	Fluctuation models	34
3.2	Random number generators	35
3.3	Simulation results	36
4	Fluctuations in physical models	45
4.1	Hijing	45
4.2	Event selection	45
4.3	Particle decays	46
4.4	Results of the Hijing simulation	46
5	The PHENIX experiment	53
5.1	The Relativistic Heavy-Ion Collider facility	53
5.2	Overview of the PHENIX detector system	56
5.3	Detectors for global observables	56
5.4	Tracking system	58
5.5	Detectors for particle identification	62
6	Details of the fluctuation analysis	65
6.1	Event reconstruction in the central arms	66

6.2	Momentum reconstruction	67
6.3	Centrality determination	68
6.4	Event and track selection	71
6.5	Track proximity cuts	72
6.6	Particle identification	73
6.7	Multiplicities of identified particles	74
6.8	Systematic uncertainties	79
7	Quality assurance	86
8	Analysis of Gold-Gold collisions at $\sqrt{s_{\text{NN}}} = 200$ GeV	90
8.1	Centrality dependence of ν_{dyn}	91
8.2	Dependence on momentum and azimuthal acceptance . . .	93
8.3	Charge combinations	97
8.4	Application of sum rules	99
8.5	Error calculation	102
8.6	Summary and outlook	103
A	Rapidity and pseudorapidity	105
B	Details of the particle identification	107
C	Studies of track proximity	112
D	Statistical error in ν_{dyn}	118
	References	119
	Paper I	123

Chapter 1

Introduction

Everything in the Universe is governed by the laws of the fundamental forces: gravity holds the planets and stars in place; the weak force is responsible for the radioactive beta decay; the strong force prevents the atomic nucleus from falling apart and the electromagnetic force explains all electronic devices and chemical processes and most other macroscopic phenomena of every day life.

In order to have an intuitive feeling for the fundamental forces, one can look at their relative strengths listed in table 1.1. Gravity is weak in comparison with the other forces on a subatomic level, although very much noticeable on a larger scale since the strength of the gravitational force depends on the mass of the objects involved. The relative strengths are calculated at an energy scale of 1 GeV, relevant to the high-energy physics scope of this work, but will vary with energy since the coupling constants have a non-uniform energy dependence. It is tempting to believe that the coupling constants of all four forces will converge at some very high energy scale, allowing for the forces to be modelled by a single coherent theory. Currently, most phenomena in high-energy physics are explained in the standard model of particle physics, which does not include gravity but provides a good description of weak and electromagnetic interactions, unified in the electroweak theory, as well as strong interactions.

1.1 The standard model

The standard model is a quantum field theory. It describes the elementary particles and their interactions and it has been very successful in explaining almost all current experimental observations on elementary systems, down to a deep level of detail. Recently, observations have been made which call

Force	Coupling Constant	Relative Strength	Force carrier
Strong	α_S	1	gluon, g
Electromagnetic	α_{EM}	1/137	photon, γ
Weak	α_W	10^{-6}	W^+ , W^- , Z^0
Gravitational	α_G	10^{-39}	graviton

Table 1.1: Relative strengths of the fundamental forces in terms of their respective coupling constants at an energy scale of 1 GeV. For the weak force the value is derived from the difference in observed decay times for strong and weak decays [1]. The gravitational force is in relation to the electromagnetic force between two protons. The graviton is not yet observed.

for explanations beyond the standard model, notably the astrophysical observations of dark energy and dark matter [2]. With the availability of new experiments at higher energies, several theories that predict phenomena beyond the standard model, as well as the standard model itself in a new regime, will be put to test.

Elementary particles This refers to particles with no internal structure. In the standard model the particles are assigned different quantum numbers and all interactions must follow a set of rules which assures the conservation of these numbers, in addition to the usual conservation of energy, momentum, angular momentum and charge. For every elementary particle there is an antiparticle with the same mass but with opposite quantum numbers.

There are two main categories of elementary particles; *fermions* and *bosons*. Fermions are half-integer spin particles which obey Fermi-Dirac statistics where no two particles can occupy the same quantum state at the same time, referred to as the *Pauli exclusion principle*. This results in a sort of rigidity of the medium; the constituents of matter are all fermions. The force carriers, on the other hand, are all bosons, with integer spin, which obey Bose-Einstein statistics and thus do not follow the Pauli exclusion principle.

The fermionic elementary particles are grouped into *leptons* and *quarks*, both of which contain three generations of particles with increasing mass. The particles in the first generation are stable, while the heavier particles in the second and third generation decay, more and more rapidly with increasing mass, into their lighter relatives. As a consequence, all ordinary matter surrounding us is made up of particles from the first generations leptons and quarks.

	Charge	Mass		Charge	Mass
e	-e	0.511 MeV/ c^2	ν_e	0	\sim massless
μ	-e	106 MeV/ c^2	ν_μ	0	\sim massless
τ	-e	1777 MeV/ c^2	ν_τ	0	\sim massless

Table 1.2: Leptons [1]. Antileptons have opposite charge.

	Charge	Mass		Charge	Mass
u	2/3e	1.7—3.3 MeV/ c^2	d	-1/3e	4.1—5.8 MeV/ c^2
c	2/3e	1.3 GeV/ c^2	s	-1/3e	101 MeV/ c^2
t	2/3e	172 GeV/ c^2	b	-1/3e	4.2 GeV/ c^2

Table 1.3: Quarks as listed by the Particle Data Group [1]. The u -, d -, s -, c - and b -quark masses are estimates. The t -quark mass is from direct observations of $t\bar{t}$ events.

Leptons Leptons are of two types, electron-like particles (the electron, e , the muon, μ and the tau, τ) and their respective neutrinos, ν . Charged leptons interact via the electromagnetic or weak force, while the electrically neutral neutrinos only experience weak interactions. The neutrinos are also nearly massless and they are hard to detect as they interact very little while passing through matter. In fact, the standard model considers neutrinos to be massless but recent experimental results suggest that they must have a small mass [3]. Table 1.2 lists all the leptons.

Quarks Quarks come in six flavours: up (u), down (d), charm (c), strange (s), top (t) and bottom (b). Table 1.3 lists the quarks and their respective charge and mass, although the quark masses are approximate since quarks can not be observed as free particles. The quarks carry a fraction of the elementary electric charge carried by the electron, $+2/3e$ or $-1/3e$. In addition they also carry colour charge, named red (R), green (G) and blue (B). Antiquarks (\bar{q}) carry opposite electric charge and anticolour ($\bar{R}, \bar{G}, \bar{B}$). The quarks may be combined into a large variety of colourless composite particles called *hadrons*, with integer electric charge. In addition to the valence quarks, which defines them, the hadrons may also be populated by quantum fluctuations of gluons and $q\bar{q}$ -pairs, so called sea quarks. The quarks and gluons inside the hadrons are collectively referred to as *partons*. Depending on the number of constituent (valence) quarks, hadrons can be either bosons, $q\bar{q}$, in which case they are called *mesons*, or fermions, $qqq(\bar{q}\bar{q}\bar{q})$, called *baryons(antibaryons)*, with their respective spins adding up to an integer or a half-integer. Again, ordinary matter, the nucleons (neutrons and protons) which build up all known nuclei, are fermions and they are composed of the two lightest quarks in the first generation, the u and the d quark. The heavier quarks are unstable and can only be observed

Mesons		Baryons	
$\pi^{+/-}$	$u\bar{d}/d\bar{u}$	p	uud
$K^{+/-}$	$u\bar{s}/s\bar{u}$	n	udd
K_S^0	$d\bar{s} - s\bar{d}/\sqrt{2}$	$\Delta^{++/+0/-}$	$uuu/uud/udd/ddd$
η	$u\bar{u} + d\bar{d} - 2s\bar{s}/\sqrt{6}$	Λ^0	uds
ρ_0	$u\bar{u} - d\bar{d}/\sqrt{2}$	$\Sigma^{+0/-}$	$uus/uds/ddu$
ω	$u\bar{u} + d\bar{d}/\sqrt{2}$	$\Xi^{0/-}$	uss/dss
ϕ	$s\bar{s}$	Ω^-	sss

Table 1.4: Some hadrons and their quark content [1]. Antibaryons are composed of the corresponding antiquarks.

after having been produced in the form of $q\bar{q}$ -pairs. The c , t and b quarks are very heavy and rarely produced, even at the highest energies, while the s quark is more commonly occurring in high-energy experiments. The most common hadrons, relevant to this thesis, and their quark content are listed in table 1.4. All basic hadrons have a number of *resonance states* related to them with the same quark composition, but heavier and in general with very short life-times as they decay by the strong interaction.

Quantum chromodynamics QCD, is the theory that describes the interactions of the strong force that acts on colour charge. A special feature of QCD is that the force mediator, the gluon, itself carries colour. This leads to some important high-energy phenomena. Under normal conditions, quarks are confined by the strong force in the colourless hadrons. However, according to QCD the force gets weaker with increasing energy (shorter distances/higher temperature). As a result, if the energy is high enough the quarks will behave as if they were free, referred to as *asymptotic freedom*.

1.2 The quark-gluon plasma

According to QCD there should exist a phase of colour charged matter with deconfined quarks at high energy density. This phase is called quark-gluon plasma, QGP, and it is assumed to have been present very early in the development of the universe from the Big Bang. The aim of recent experiments with very high-energy heavy-ion collisions is to reproduce the conditions present at this time. A quark-gluon plasma is a very hot and/or dense system of quarks and gluons, ideally in chemical and thermal equilibrium, and if there is nothing to counterbalance the huge pressure in the medium, there will be a rapid expansion during which the temperature and pressure decreases. As the distance between the quarks grows during the

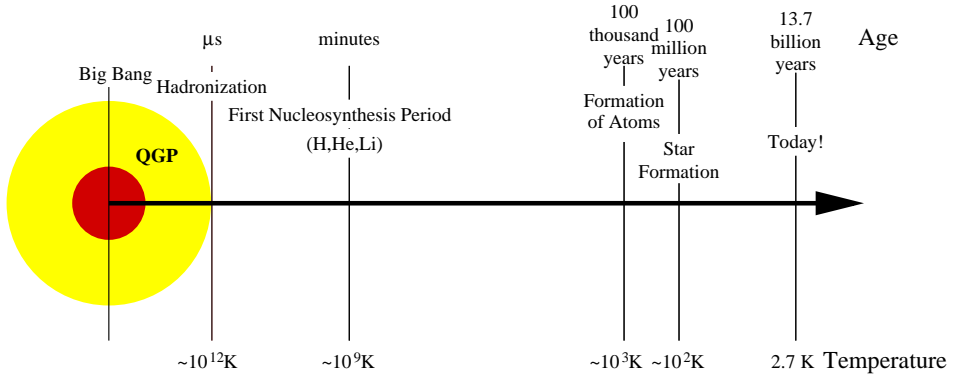


Figure 1.1: Evolution of the Universe following the Big Bang.

expansion, the force between them becomes stronger and eventually they will have to form colourless hadrons. This phase transition occurred during the first microseconds following the Big Bang as illustrated in the timeline in figure 1.1.

A neutron star is an example where the gravitational pressure generated by the mass of the star can be so large that it could contain a very dense, but cold, quark-gluon plasma in its core. The early universe and the neutron star are two natural instances of QGP that occupy opposite extremes in the phase diagram of nuclear matter, fig 1.2, which is a function of temperature, T , and net baryon number density, ρ_B , with the Big Bang at low net baryon density and extreme temperature and neutron stars at extreme net baryon density but low temperature. The curve dividing the diagram in two is approximate and describes the critical energy density where matter goes from being hadronic to QGP-like. Calculations [14] indicate a critical energy density of $\sim 1 \text{ GeV/fm}^3$ at which the phase transition should occur. This is about an order of magnitude larger energy density than for ordinary nuclei. The critical temperature, $T_C \sim 150\text{--}170 \text{ MeV} \approx 10^{12} \text{ K}$ is a hundred thousand times higher than the temperature in the core of the sun.

1.3 High-energy heavy-ion collisions

Experiments with high-energy heavy-ion collisions produce conditions that are somewhere in the middle of the phase diagram in figure 1.2, approaching the Big Bang conditions with increasing energy. Two ideas have been pursued in the creation of the QGP using high-energy heavy-ion collisions.

At the lower part of the relevant energy scale the colliding nuclei are stopped by one another, resulting in a not so hot but net baryon dense system. A QGP is created if the density is high enough that the nucleons start to

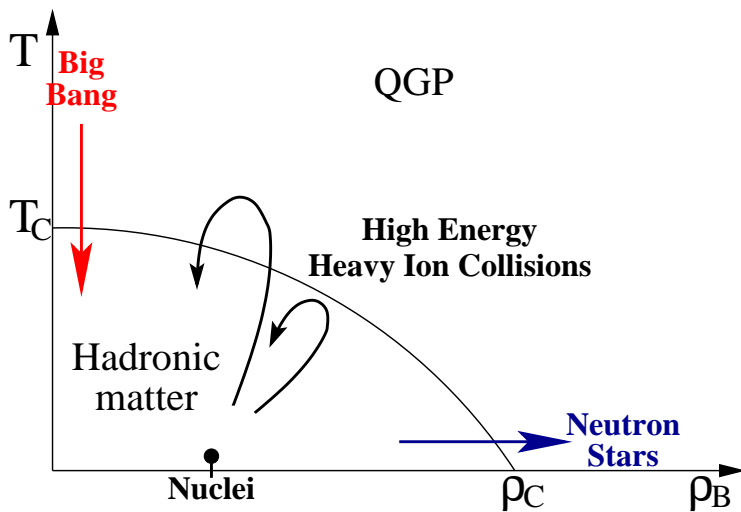


Figure 1.2: The phase diagram of nuclear matter including its major features.

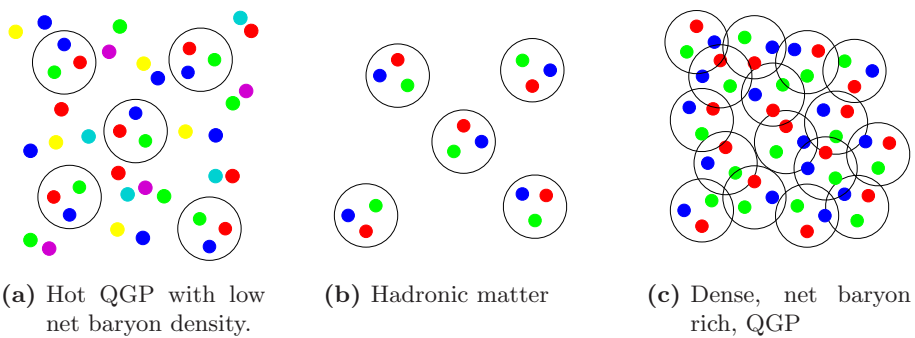


Figure 1.3: Hot and dense QGP in comparison with normal hadronic matter.

overlap, as depicted in figure 1.3c. This is the kind of collisions studied for example in experiments at the Alternating Gradient Synchrotron, AGS, at BNL and at the Super Proton Synchrotron, SPS, at CERN. They will be further studied at the Facility for Antiproton and Ion Research, FAIR, which is being constructed at GSI.

As the collision energy grows, the nuclei become more and more transparent to each other. High energy inelastic collisions between individual nucleons in the nuclei will dominate at first, releasing a large number of partons. These partons will rescatter many times in the dense nuclear material and redistribute a large fraction of the incident kinetic energy in the central region. The result is more like a very hot fireball where quark-antiquark pairs are created out of vacuum energy, as in figure 1.3a. Hence, although the system created in the central region may be dense, it is one with low *net baryon density*. The forward and backward regions are still net baryon rich, reflecting the composition of the incident nuclei which has passed through each other. These types of collisions are currently studied at the Relativistic Heavy-Ion Collider, RHIC, at BNL and at the Large Hadron Collider, LHC, at CERN.

The ratio of antiprotons to protons, \bar{p}/p , can be taken as a measure of the net baryon density. For their respective maximum collision energies, this ratio is 0.06 at SPS and 0.8 at the twelve times higher energies at RHIC, which indicates that heavy-ion collision at RHIC are produced at almost baryon free ρ_B . At yet another factor of ten times higher collision energies at the LHC $\bar{p}/p \approx 1$, which corresponds to $\rho_B=0$ [7, 8]. Thus by varying the collision energy it is possible to study the transition between hadronic and quark matter at different locations in the phase diagram. Table 1.5 summarizes the different accelerators and their maximum collision energies for heavy nuclei. In order to study the phase transition over a larger region of the phase diagram, an energy scan of Gold-Gold collisions down to SPS equivalent energies has been undertaken at RHIC during 2010 and such studies will be further performed in the future RHIC programme.

1.4 The equation of state

If the system is at least in local equilibrium it can be described by thermodynamics and it becomes meaningful to characterize it using such statistical quantities as temperature, pressure, entropy density and energy density. The relations between these quantities are determined by the equation of state, EOS, which reflects the number of degrees of freedom in the medium.

A QGP can be expected to be dominated by two or three active quark flavours, f , (up, down and strange), each with two spin states, s , ($\uparrow\downarrow$),

Accelerator facility	Start. Year	Acc. Species	$\sqrt{s_{NN}}$ (GeV)
CERN SPS	1986	^{16}O	20
BNL AGS	1987	^{28}Si	5
CERN SPS	1992	^{32}S	20
BNL AGS	1994	^{197}Au	4
CERN SPS	1994	^{208}Pb	17
BNL RHIC	2001	$^{197}Au + ^{197}Au$	200
BNL RHIC	2005	$^{63}Cu + ^{63}Cu$	200
CERN LHC	2010	$^{208}Pb + ^{208}Pb$	2750
CERN LHC	2014	$^{208}Pb + ^{208}Pb$	5500
<i>future facilities</i>			
JINR NICA	~2016	$A + A$	4-11
GSI FAIR	>2017	A	2-45

Table 1.5: Summary of HIC experimental programmes [4]. At RHIC and LHC two accelerated beams of ions are collided with one another, while at SPS and AGS one accelerated ion beam was made to collide with a stationary target. The collision energy, $\sqrt{s_{NN}}$, is the maximum available energy in a collision of a nucleon in the projectile with one in the target. The proposed run programme from both NICA and FAIR are low energy scans using a broad range of ions from Hydrogen to Gold and Uranium, respectively [5, 6].

two quark states, q , (quark, antiquark) and three possible colours, c , (red, green, blue), plus gluons which also have two spin states and eight possible colour configurations [4]. This results in a much larger number of degrees of freedom in comparison with hadronic matter. For N_f quark flavours the number of degrees of freedom for a QGP, d_{QGP} , is given by

$$d_{QGP} = N_f \cdot 2_s \cdot 2_q \cdot 3_c \cdot \frac{7}{8} + 2_s \cdot (3_c^2 - 1) \quad (1.1)$$

and for a hadronic gas which can be considered to be made up of only pions it is given by

$$d_\pi = N_f^2 - 1 \quad (1.2)$$

The huge difference in number of degrees of freedom in a QGP and a hadronic gas is illustrated by eqn 1.3. Even with only two quark flavours taken into account, there are twelve times more degrees of freedom in the QGP.

$$\frac{d_{QGP}}{d_\pi} = \frac{2_f \cdot 2_s \cdot 2_q \cdot 3_c \cdot \frac{7}{8} + 2_s \cdot 8_c}{3} = 12 \quad (1.3)$$

As a consequence, one may expect a, sometimes sudden, change of the thermodynamic quantities as matter crosses the phase boundary in either direction, to accommodate for the change in degrees of freedom. For example, the entropy density is proportional to the number of particles per

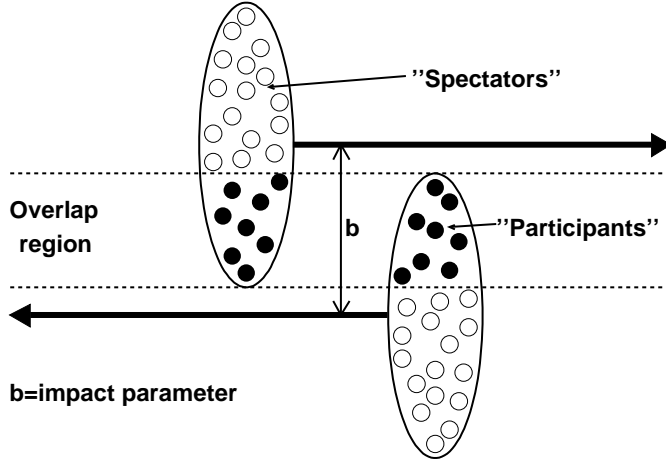


Figure 1.4: Collision geometry. The nuclei appear flattened since they are Lorentz contracted in the laboratory frame when accelerated to relativistic velocities.

unit volume dN/dV . When the quarks are released from the pions as the hadronic gas becomes a QGP, the number of particles will double within a short time frame. In the simplest case this would cause a jump in the entropy density. However, since all the thermodynamic quantities are dependent on each other this effect can be smoothed by other properties changing at the same time.

1.5 Terminology

The geometry of a collision between two ions is illustrated by figure 1.4. The impact parameter, b , which is the distance between the centres of two colliding nuclei, is used to classify the collisions into different centrality classes. The larger the overlap, smaller b , the more central the collision is said to be. The nucleons inside the overlap region are called participants since they participate in the creation of the colliding system, while the nucleons outside of this region, which are called spectators, will continue quite unaffected in their original direction of motion, either as free nucleons or in the form of nuclear fragments.

To describe particles emerging from a collision, a right handed coordinate system is adopted and the longitudinal direction, z , is defined along the beam direction, as drawn in figure 1.5. Often, polar coordinates are used with ϕ and θ as shown.

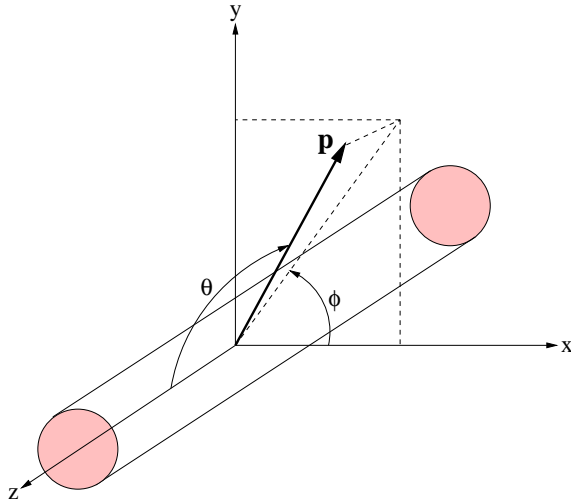


Figure 1.5: Coordinates of a particle of momentum \mathbf{p} moving out from the collision point of the two ions that entered from opposite z directions.

The momentum vector of the particle is decomposed in two parts, one longitudinal in parallel to the beam axis, $p_L = |\mathbf{p}| \cos(\theta)$, and one in the plane transverse to the beam axis, $p_T = |\mathbf{p}| \sin(\theta)$.

Since many particles produced in high-energy collisions have relativistic velocities which are not linearly additive, an alternative boost invariant formulation is introduced to define the movement of particles along the z -axis. It is called rapidity, $y \equiv \tanh^{-1}(\beta) = \frac{1}{2} \ln\left(\frac{1+\beta}{1-\beta}\right)$, with $\beta = \frac{v_z}{c}$. The pseudorapidity, $\eta \equiv -\ln\left(\tan\left(\frac{\theta}{2}\right)\right)$, is an approximate measure for particles with transverse momentum much greater than their mass. In practise it is used as a measure of the rapidity when the mass of a particle can not be determined, since it only requires knowledge of the emission angle of the particle with respect to the beam axis. A derivation of rapidity and pseudorapidity can be found in appendix A.

1.6 Signals of the quark-gluon plasma

A first requirement for the formation of a quark-gluon plasma is that a high enough energy density is produced. Estimates [14] strongly suggest that the energy density created in $\sqrt{s_{NN}} = 200$ GeV Gold-Gold collisions at RHIC is well above the level required for the formation of a quark-gluon plasma. If the system is sustained long enough it will attain a state of equilibrium and one can search for the signs of thermalization and collective behaviour which an equilibrated system should demonstrate.

Since the hot and dense medium we would like to study in these collisions exists for such a brief time before it expands and cools off, it can not be studied directly. Instead, all information about the medium created in the collision must come from particles and radiation observed to originate from the collision region.

As the temperature falls, hadrons are condensed out of the quark-gluon plasma, fixing their hadro-chemical compositions. The abundance of hadrons of different types then reflect the properties and quark balance of the medium at this time, which is called the chemical freeze-out. The thermal equilibrium state, if achieved, will last a little longer, redistributing energy and momentum between the hadrons until they escape the system. This is the thermal freeze-out. The energy and momentum distributions of the observed hadrons will then reflect the properties of the system at this time.

Photons and leptons, such as electrons and muons, can escape the collision system undisturbed because they do not interact strongly with the QGP since they are colour neutral, nor do they interact with the produced hadrons to any larger extent. They can therefore provide information on the initial properties of the system.

Virtual photons are emitted in hard scatterings between partons, quarks or gluons, in the colliding nuclei in the early stages of the collision. These photons can only exist for a brief time before they materialize, commonly into dilepton pairs, like an electron and a positron. If the decay time of the virtual photon is short enough the dileptons will be produced inside the QGP medium and may provide important information on the early stages.

There is also an emission of thermal photons from the hot medium. If the system is in thermal equilibrium the emission spectrum should have the characteristic shape of black-body radiation which is dependent on the temperature. The yield also depends on formation time.

1.6.1 Equilibrium of quark flavors

A sign of chemical equilibrium being established between u , d and s quarks, is an increase in the production of strange particles, i.e. particles containing one or more strange quarks. In statistical production of quark pairs from hard collisions, s quarks are normally disfavoured due to their high mass in comparison with u and d quarks. In a medium with deconfined quarks, equilibrium between gluons and u , d and s quarks can be established. This is often studied through the comparison of experimentally obtained ratios of particle yields with model predictions. An example of such a study can be seen in figure 1.6, which shows a compilation of results from all four RHIC

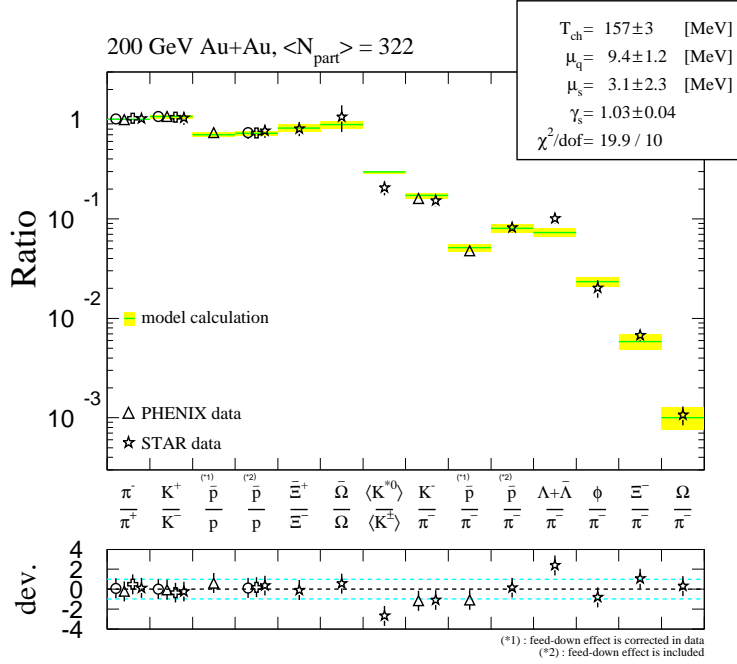


Figure 1.6: Experimentally measured particle ratios in central Au+Au collisions at $\sqrt{s_{NN}}=200$ GeV, in PHENIX (triangles), Star (stars), Phobos (crosses) and Brahms (rings). These are compared with a thermal model prediction (shown as lines) from Kaneta and Xu. The bottom plot shows the deviation of data to the model scaled by the error of the experimental data points. From [9].

experiments [9]. A model fit to this data gives a strangeness saturation factor, $\gamma_S = 1$, which indicates that strangeness is fully equilibrated.

1.6.2 Medium effects

In the study of heavy-ion collisions, results from proton-proton collisions at the same collision energy per nucleon are often used as a baseline. Any pointlike process should then scale with the number of binary nucleon-nucleon inelastic collisions in the colliding nuclei, N_{coll} , in the absence of effects caused by the nuclear medium that could modify the yield. To measure the amount of nuclear medium effects a ratio called the nuclear modification factor is used, defined as

$$R_{AB} = \frac{dN_{AB}^P}{\langle N_{coll} \rangle dN_{NN}^P}, \quad (1.4)$$

where dN_{AB}^P is the differential yield of a pointlike process P in the collision of two nuclei (A and B) and dN_{NN}^P is the corresponding yield in a proton-

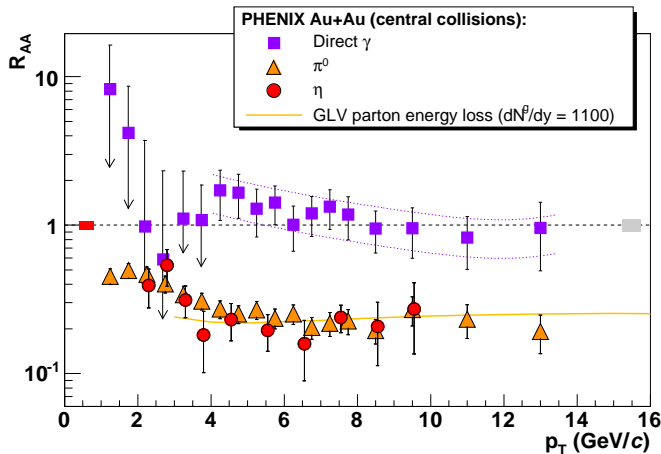


Figure 1.7: Nuclear modification factor of π^0 , η and direct photons(γ) for central (0 – 10%) Gold-Gold collisions at $\sqrt{s_{NN}} = 200\text{GeV}$, measured by PHENIX [13]. GLV is a model calculation based on radiative energy loss of colour charged particles traversing a coloured medium.

proton collision [14]. If the ratio deviates from one it would be due to effects either in the initial or final state of the colliding nuclei. Corresponding studies at SPS energies revealed R_{AA} values in excess of 1. This effect, named Cronin effect, was understood as a result of rescattering.

Figure 1.7 shows R_{AA} as a function of p_T for π^0 's, η and γ 's in central Gold-Gold collisions at $\sqrt{s_{NN}} = 200\text{ GeV}$. The π^0 and the η , which is four times heavier than the π^0 , both exhibit clear nuclear medium effects of the same strength. Directly produced photons, as can clearly be seen, do not exhibit any nuclear medium effects, indicating that these effects are due to the strong force. The fact that R_{AA} for high energy photons flattens out at 1 also verifies that the expected scaling by $\langle N_{coll} \rangle$ is correct.

A jet is a shower of particles produced in a cone around the direction of a leading high-energy particle. The jet particles originate from the fragmentation of a very high energy parton, produced in hard scatterings between partons in the colliding nucleons in the early stages of the collision. When these partons are created in pairs, they will carry a lot of energy and for the sake of momentum conservation they will be travelling in opposite directions to each other, resulting in two back-to-back jets.

As a result of the quarks being deconfined in the QGP, a colour charged particle travelling through the QGP would interact strongly with the surrounding medium and loose energy. This effect can show up as a suppression of high momentum particles. For the case of a hard-scattering quark pair being produced in the surface region of a QGP fireball, one of the quarks may be able to quickly leave the medium outwards, without loos-

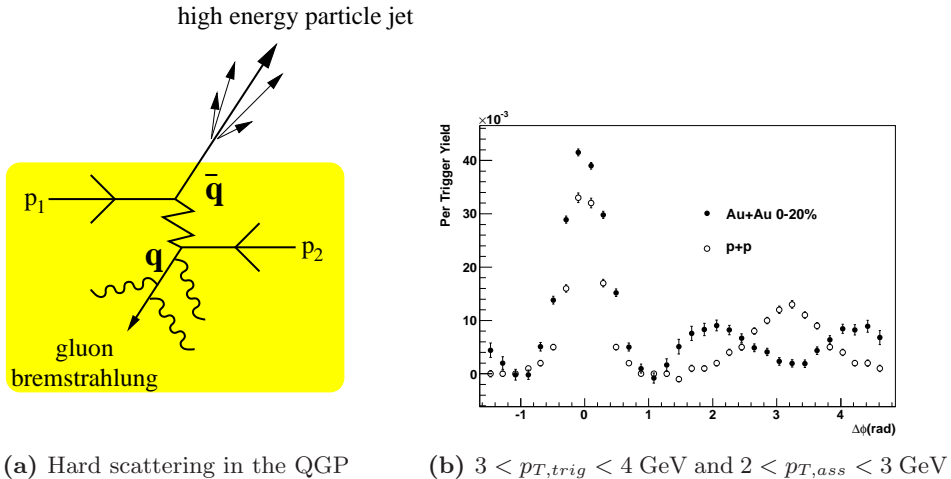


Figure 1.8: The per trigger yield is defined as $(1/N^a)dN^{ab}/d\Delta\phi(rad^{-1})$ [18] for trigger particle a and associated particle b .

ing energy, and produce a jet. The other quark of the pair, however, will have to travel through the full thickness of the QGP medium, where it will lose energy by e.g. gluon bremsstrahlung. The jet in this direction will be quenched, as illustrated by figure 1.8a. Figure 1.8b shows the result of a jet search in central Gold-Gold collisions at $\sqrt{s_{NN}} = 200$ GeV compared with proton-proton collisions at the same collision energy. The back-to-back jet correlation, with $\Delta\phi \approx \pi$, is clearly suppressed in central Gold-Gold collisions and the energy is redistributed in the away side jet. In order to rule out the possibility that the jet is quenched by normal nuclear matter, i.e. a system of colour neutral particles, a control experiment was done with deuteron on gold. This revealed a dijet topology like in proton-proton collisions and a vanishing nuclear modification of high p_T hadrons.

1.6.3 Flow

An example of a collective behaviour is the anisotropic flow of the medium, which in the hydrodynamic model arises if the collision zone has an asymmetric shape. In non-central collisions only parts of the two ions will overlap, creating an almond-shaped collision zone as illustrated by figure 1.9a. The pressure gradient will then be steeper in the direction of the shortest axis, which results in a boosting of particles in this direction. The particle emission as viewed in the plane transverse to the beam axis will therefore have an elliptical distribution relative to the direction of the impact parameter which defines the reaction plane, described by

$$\frac{dN}{d\phi} = N_0(1 + 2v_2 \cos(2(\phi - \Phi))), \quad (1.5)$$

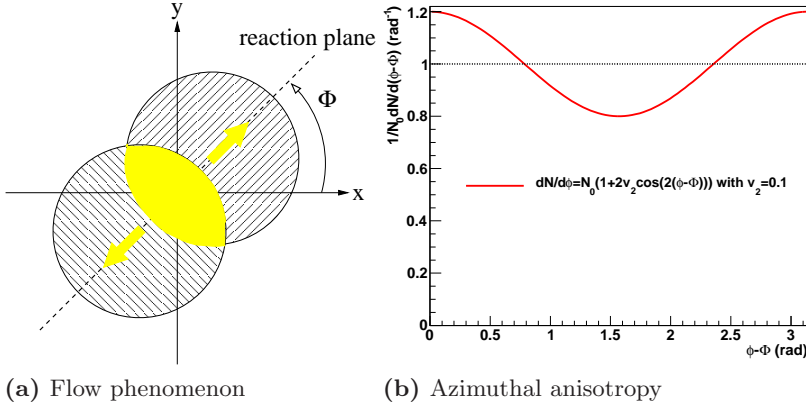


Figure 1.9: Collective behaviour in the system manifested as elliptic flow.

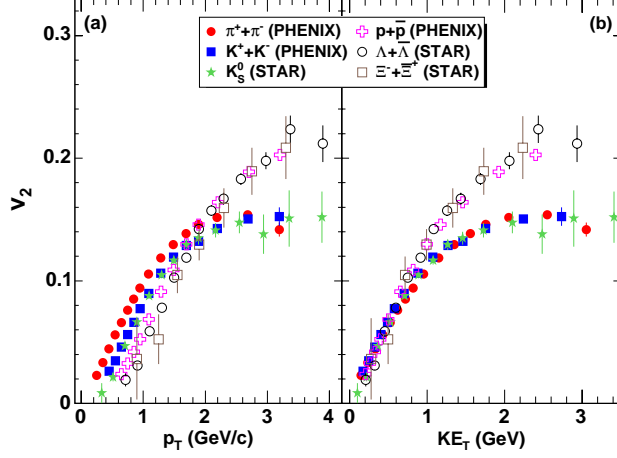
where Φ is the azimuthal inclination angle of the reaction plane as shown in figure 1.9a.

Figure 1.9b illustrates the effect of elliptic flow on the distribution of particles in the azimuthal plane for $v_2 = 0.1$, which is a typical value for light hadrons at $p_T \sim 1$ GeV/c in Gold-Gold collisions at $\sqrt{s_{NN}} = 200$ GeV.

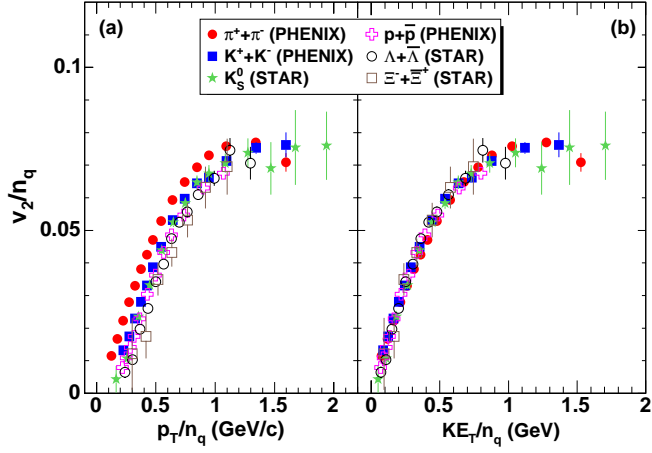
Figure 1.10 shows the anisotropy parameter, v_2 , for identified particles in minimum-bias Gold-Gold collisions at $\sqrt{s_{NN}} = 200$ GeV. Figure 1.10a shows v_2 as a function of p_T compared with v_2 as a function of the transverse kinetic energy, $KE_T = m_T - m$. There is a clear mass ordering at low p_T where all particle species scale with KE_T as predicted by hydrodynamics for a perfect, or almost perfect, fluid, i.e. a fluid with very low viscosity. At higher p_T this scaling is broken with mesons and baryons grouping separately. In figure 1.10b the same results are shown but scaled by the number of constituent quarks, $n_q = 2$ for mesons and $n_q = 3$ for baryons. A perfect scaling is obtained for all particle species when v_2/n_q is shown as a function of KE_T/n_q . This supports the idea that the underlying degrees of freedom are the free quarks and that the quark-gluon plasma created in these collisions is a strongly coupled, nearly perfect, fluid as opposed to a weakly coupled gas.

1.6.4 Direct photons

If the system of QGP is in local equilibrium it can be expected to radiate as a black body. Direct virtual photons, radiated off the charged constituents of the plasma, can be detected via their decay into e^+e^- pairs. Figure 1.11 shows the p_T -spectrum of direct photons in central (0-20%)



(a) PID Scaling



(b) Quark Scaling

Figure 1.10: Azimuthal anisotropy parameter as a function of transverse momentum and transverse kinetic energy for particles identified in $\sqrt{s_{NN}} = 200$ GeV minimum-bias Gold-Gold collisions [16]. In (b) the result is scaled by the number of constituent quarks.

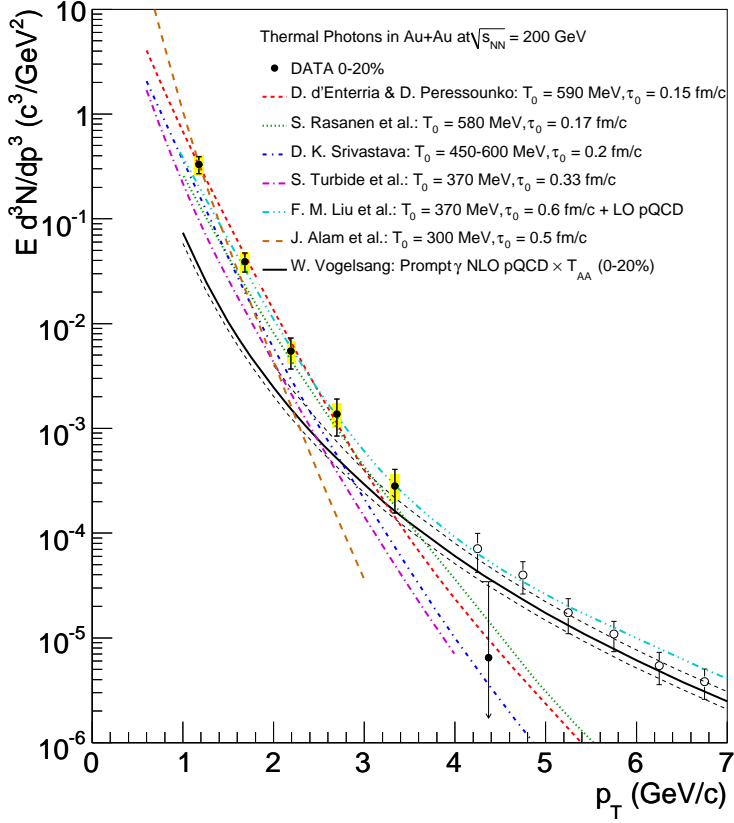


Figure 1.11: Direct photon spectrum extracted from the e^+e^- invariant mass spectrum for 0-20% central Gold-Gold collisions compared with theoretical calculations of thermal photon emission [17].

Gold-Gold collisions compared with several theoretical calculations of thermal photon emission. The black solid line shows a NLO pQCD calculation of the expected yield in $p+p$ collisions scaled by the Glauber nuclear overlap function, T_{AA} , to serve as a baseline comparison for the yield in Gold-Gold collisions of prompt photons from hard initial collisions. The excess over this expected yield at low momentum is interpreted as coming from thermal photon emission in the early stages of the collision. The theoretical hydrodynamical models which can explain the data assumes initial temperatures ranging from 300-600 MeV.

1.6.5 Heavy quarkonia

Dileptons are, among other possibilities, produced from weak decays of hadrons on their way from the collision point to the detector. As such they can be used to reconstruct the mass and momentum of the mother particles.

Especially, neutral heavy mesons consisting of quark-antiquark pairs can be studied via their decay into dileptons. Examples of such particles are the J/ψ and the slightly heavier J/ψ' , which consist of a charm quark-antiquark pair ($c\bar{c}$), and the Υ , which consists of a bottom quark-antiquark pair ($b\bar{b}$). These particles have different life-times which can be used to study the effect of in-medium decays. The suppression of the J/ψ production was one of the first proposed signals of QGP formation [10]. The reason should be colour screening in the medium preventing the c and \bar{c} from binding together to form a J/ψ but rather combining with u and d quarks. However, it is possible that the temperature have to be much higher than the critical temperature for QGP formation for this screening effect to come into play. Lately is has also been suggested that, at high energies, the suppression could be compensated by an increased production of c and \bar{c} quarks in the initial collisions [11].

1.6.6 Effects of the phase transition

The large difference in number of degrees of freedom in a hadronic gas and a QGP could have several implications. For instance there would be a rapid change in energy density, ϵ , or entropy density, s , as the critical temperature is approached. Experimentally these variables correspond to the measured transverse energy, hadron multiplicity and average transverse momentum:

$$\epsilon \sim \frac{dE_T}{dy}, \quad s \sim \frac{dN}{dy}, \quad T \sim \langle p_T \rangle. \quad (1.6)$$

Fluctuations can arise as a result of the phase transition due to discontinuities at the phase boundary. Another approach to fluctuations would be to study the amplitude of fluctuations at varying collision conditions. Both enhanced and decreased fluctuations in a QGP in comparison with a hadronic gas are expected for different observables.

The observations summarized here indicate that a phase transition to a QGP phase takes place with large probability in central heavy-ion collisions at $\sqrt{s_{NN}} = 200$ GeV. Several of these signatures of QGP have been proposed by models while others are surprises. Fluctuations in the medium as a result of the phase transition has been an expected signal of the QGP formation since this field of physics started but so far no significant fluctuations that could be directly related to a phase transition have been observed. This thesis deals with fluctuation studies.

Chapter 2

Studies of fluctuations

One way to characterize a physical system is to study and analyse fluctuations in the system. In doing so, it is important to separate the dynamical fluctuations, which reflect the dynamic evolution, and responses of the system, from fluctuations induced by the measurement, like finite number statistics and limited acceptance. The latter ones need to be fully controlled in order to be able to access the dynamical fluctuations which are of physics interest.

Fluctuations can be studied in a number of different ways. To start with, one can study the fluctuations within one single event. A well known application of this method is the study of microwave background radiation originating from the Big Bang as measured by COBE [33], resulting in new constraints on cosmological parameters. If a larger event sample is available, one can average the fluctuations obtained in each event in order to increase the statistical significance of the observation of fluctuations. This is for example done to extract system volume in nuclear collisions from Hanbury Brown-Twiss correlations [34]. A common approach to fluctuations in heavy-ion collisions, and the one used in this thesis, is to analyse them on an event-by-event basis, i.e. to study how some observable varies from event to event.

Several observables have been proposed for the study of event-by-event fluctuations in ultra relativistic heavy-ion collisions, aiming to explore different aspects of the collision conditions. Some are related to thermodynamical properties of the system while others are sensitive to the critical behaviour which arise as a result of a phase transition. Surveys are made for example as a function of centrality, collision energy or detector acceptance in order to identify any deviation from what is expected in a non-QGP scenario. Ratios of observables, like event averages or ratios of different particle species, are often used in order to avoid the influence of volume

and impact-parameter fluctuations. When both the numerator and the denominator scale up or down by the same amount as the collision volume varies, the effects cancel out in the ratio.

2.1 Thermodynamics

Suppose an equilibrium state of QGP is formed in a collision of two heavy ions. Then the properties of the formed system should differ significantly from what is found for a purely hadronic collision system. Depending on the expansion rate of the system and on the hadronization process, signals of the QGP may remain visible in the distribution of particles produced.

The bulk properties of a system in equilibrium is described by statistical physics. When only a limited region of phase space is studied, as is usually the case in heavy-ion experiments since detectors are mostly placed around mid-rapidity, conserved quantum numbers can be exchanged with the surrounding system. The best statistical model is then the grand canonical ensemble [35], which will be used in section 2.3.3.

2.2 Phase transitions

If a phase transition takes place in a heavy-ion collision so that matter goes from being in a hadronic phase to a QGP phase, density fluctuations can arise. The nature of this transition may influence the observed fluctuations, which can be expected to be either enhanced or reduced [36].

Figure 2.1 shows the principal features of the phase diagram of strongly interacting matter with the temperature, T , versus the baryo-chemical potential, μ_B . At very low baryon density the transition from the hadronic phase to the QGP phase is believed to be a smooth cross-over, while at high density it can be of first order. Somewhere in between there should then exist a critical point, p , in which vicinity the transition is of second order.

At a second order phase transition the specific heat, C_V , diverges and fluctuations in p_T or temperature should be strongly reduced. This fact could be used when searching the phase diagram for the critical point.

Both a smooth cross-over and a first order phase transition can increase fluctuations. In case of a rapid expansion after a first order phase transition it is expected that droplets of deconfined matter with high baryon and energy density will be formed in a background of low-density hadronic matter. This would enhance fluctuations in a number of quantities. Also,

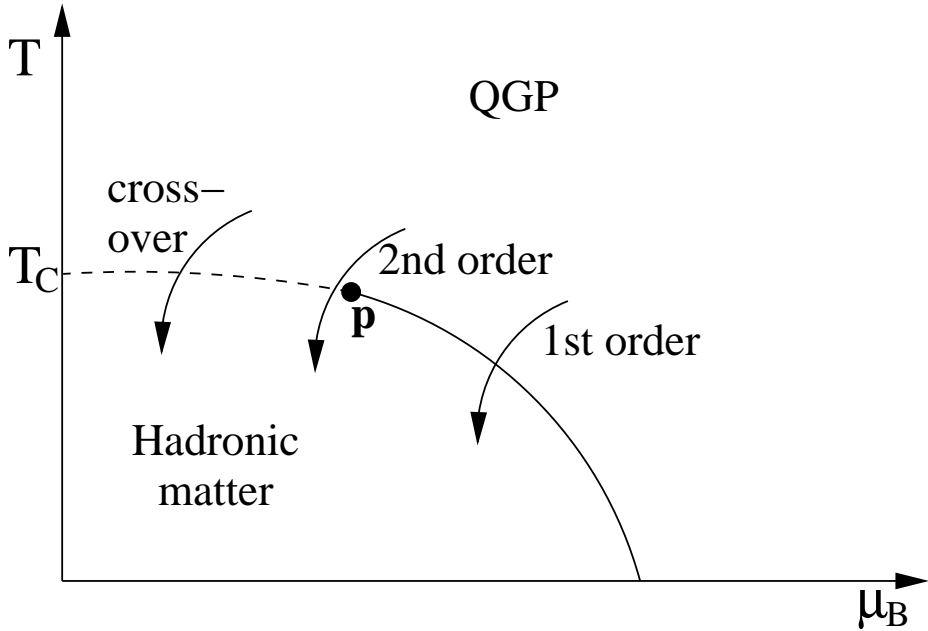


Figure 2.1: Phase diagram of nuclear matter showing the presumed orders of the transition from the QGP phase to the hadronic phase for different regions.

if the transition is a smooth cross-over, initial fluctuations should increase due to a softening of the equation of state but the effect would be much smaller than for a strong first order phase transition.

Although the order of the transition is of importance for the initial fluctuations, the fluctuations in the particle distribution at freeze out will depend on a number of other facts like the transition time of the system, the degree of equilibrium, the hadronization process and the amount of rescattering between hadronization and freezeout. It is possible that the fluctuation signals will be strongly attenuated before the system thermally freezes out.

2.3 Previous PHENIX results on fluctuations

Fluctuations of net charge and average transverse momentum have been studied in PHENIX with results that show little support for anomalous fluctuations or any critical behaviour resulting from a sharp phase transition.

2.3.1 Net-charge fluctuations

One proposed signature [38, 39, 40] of the QGP is a decrease in fluctuations of net charge. This should be due to the fact that the QGP consists of fractionally charged quarks in contrast to the unit charged particles found in hadronic matter. Charges in the QGP will therefore be shared on more carriers and thus statistically more evenly spread out. The addition or removal of one charge carrier will then have less effect than it would in a hadronic gas.

Charge conservation dictates that the net charge, $Q = N_+ - N_-$, of all particles in the full phase space is a constant. This means that there are no net-charge fluctuations and the variance $V(Q) = 0$, since

$$V(Q) = \langle Q^2 \rangle - \langle Q \rangle^2 \quad (2.1)$$

However, in limited regions of phase space, where only a fraction p of N produced particles are observed in a stochastic scenario, the variance is no longer identically zero. With the expected number of charged particles in the region being $n_{ch} = pN$, the normalized variance becomes

$$v(Q) = \frac{V(Q)}{n_{ch}} = 1 - p \quad (2.2)$$

Figure 2.2 [41] shows $v(Q)$ for the 10% most central events as a function of the width of the azimuthal window in degrees of reconstructed tracks, defined at the vertex, $\Delta\phi_r$. For small angular openings, data agree with the stochastic $(1 - p)$ scenario drawn as a solid line in the figure, and the deviation at larger $\Delta\phi$ is well described by RQMD simulations which take into account correlations from resonance decays. Hence, no new physics is implied by the measured net-charge fluctuations. However, it is not clear if net-charge fluctuations in the QGP can survive the hadronization process in these collisions.

2.3.2 Average p_T fluctuations

Fluctuations in average transverse momentum are related to energy and temperature fluctuations. The event averaged p_T is defined as

$$M_{p_T} = \overline{p_T} = \frac{1}{n} \sum_{i=1}^n p_{T_i}, \quad (2.3)$$

for an event with n detected charged particles with transverse momenta p_{T_i} .

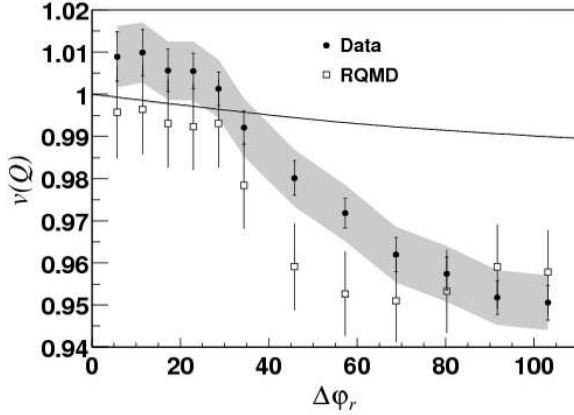


Figure 2.2: Normalized net-charge fluctuations as a function of $\Delta\phi_r$ for the 10% most central events in data and RQMD compared with the expectation from a purely stochastic scenario (solid line) [41].

Mixed events are used as a measure of the statistical fluctuations in M_{p_T} . They are formed by combining tracks from different events so that no two tracks from the same event are found in the same mixed event, reproducing the distribution of charged tracks in the mixed event sample and assuring that $\langle M_{p_T} \rangle$ exactly matches the semi inclusive $\langle p_T \rangle$.

Then the non-statistical fluctuations can be quantized as

$$F_{p_T} = \frac{\omega_{p_T, data} - \omega_{p_T, mixed}}{\omega_{p_T, mixed}}, \quad (2.4)$$

where ω_{p_T} is the normalized standard deviation of M_{p_T}

$$\omega_{p_T} = \frac{\sigma_{M_{p_T}}}{\langle M_{p_T} \rangle} \quad (2.5)$$

Figure 2.3 shows F_{p_T} , the measured non-random fluctuations in average p_T , as a function of centrality, expressed as number of participants, N_{part} , measured in $\sqrt{s_{NN}} = 200$ GeV Gold-Gold collisions by PHENIX [44]. It displays a strong dependence but is consistent with the effect expected from high- p_T jets if jet suppression is taken into account, as demonstrated by the comparison of data with simulated random particle production with the addition of contribution from hard scattering processes.

If assuming that all the non-statistical fluctuations are due to temperature fluctuations in the initial state, $\sigma_T/\langle T \rangle$, the difference in fluctuations between data and mix can be written [43]

$$\omega_{p_T, data}^2 - \omega_{p_T, mix}^2 = \left(1 - \frac{1}{\langle n \rangle}\right) \frac{\sigma_T^2}{\langle T \rangle^2} \quad (2.6)$$

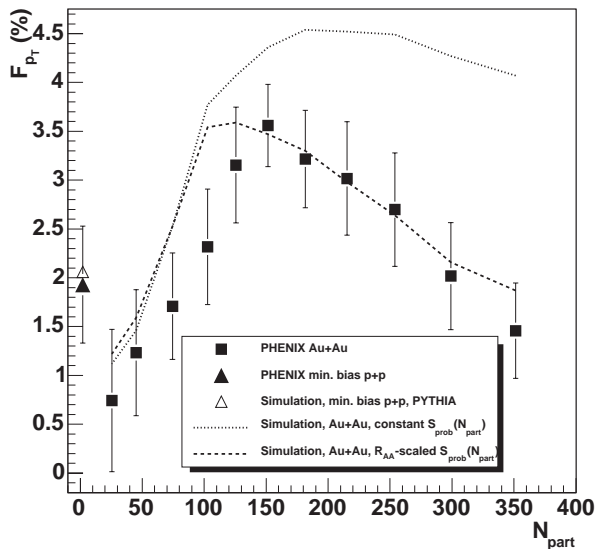


Figure 2.3: Average p_T fluctuations as a function of centrality, compared with simulations of random particle production, including jets with a production probability, S_{prob} [44].

This would yield a value for $\sigma_T/\langle T \rangle$ from PHENIX data of 1.8% for the most central Gold-Gold collisions at $\sqrt{s_{NN}} = 200$ GeV, which puts a strong limit on critical fluctuations from a sharp phase transition but is consistent with a smooth cross-over.

2.3.3 Charged hadron multiplicity fluctuations

A survey over different energies and collision species of event-by-event fluctuations of charged hadron multiplicity has been performed in PHENIX [45], in order to search for evidence of critical phenomena that could confirm the existence of a critical point and narrow down its position in the phase diagram of strongly interacting matter.

The scaled variance of the particle multiplicity, $V[N]$, is used as a measure of multiplicity fluctuations:

$$\omega_N = \frac{V[N]}{\langle N \rangle} \quad (2.7)$$

In the Grand Canonical Ensemble the variance of the particle multiplicity is directly related to the isothermal compressibility, $k_T = -1/V \partial V / \partial P_T$, as:

$$V[N] = \frac{k_B T \langle N \rangle^2}{V} k_T \quad (2.8)$$

where k_B is Boltzmann's constant, T is the temperature and V is the volume. Since the compressibility diverges close to the critical point, multiplicity fluctuations should be a sensitive probe [45] (and references therein).

In this survey, charged hadron multiplicity fluctuations are measured for Gold-Gold collisions at $\sqrt{s_{NN}}=62.4$ and 200 GeV, and Copper-Copper collisions at $\sqrt{s_{NN}}=22.5$, 62.4 and 200 GeV. The particle multiplicity distributions are fitted with negative binomial distributions which describe the data well, from which the mean multiplicity, μ_{ch} , and variance, ω_{ch} , are extracted. Dynamical fluctuations in the charged particle multiplicity are defined as

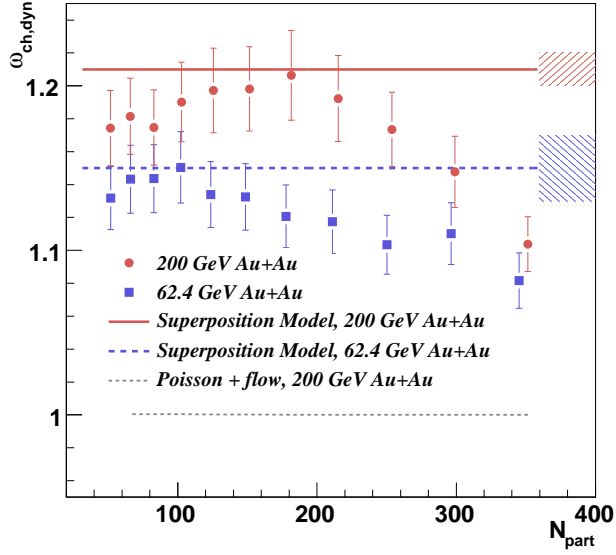
$$\omega_{ch,dyn} = f_{geo}(\omega_{ch} - 1) - 1 \quad (2.9)$$

The fluctuations are corrected for geometry fluctuations due to the width of the centrality bin, with the correction factor

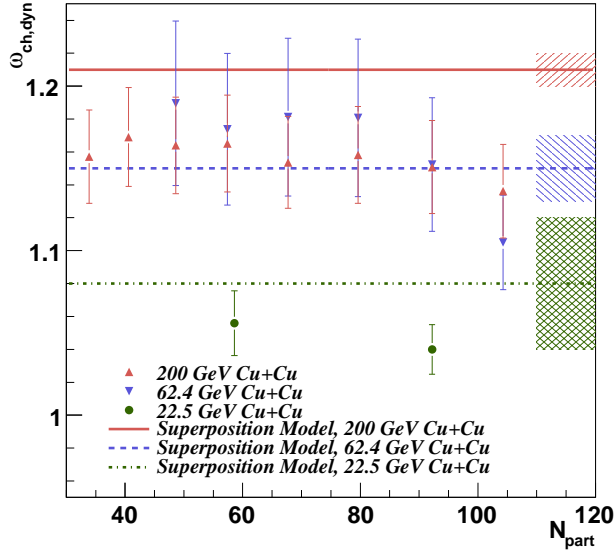
$$f_{geo} = \frac{\omega_{fixed} - 1}{\omega_{Gauss} - 1} \quad (2.10)$$

obtained from Hijing simulations using Gaussian and fixed impact parameters.

The result as a function of centrality are shown in figure 2.4a for Gold-Gold collisions and in figure 2.4b for Copper-Copper collisions, including comparisons with the participant superposition model (wounded nucleon model) [42] based on measured fluctuations in proton-proton collisions. The fluctuations in heavy-ion collisions are not in excess of the superposition model results for any of the collision energies in this survey and consequently there are no signs in this variable of critical behaviour resulting from a phase transition at these collision energies.



(a) Gold-Gold



(b) Copper-Copper

Figure 2.4: The scaled variance of charged hadron multiplicity in the range $0.2 < p_T < 2.0$ GeV, as a function of centrality expressed as the number of participants, N_{part} .

Chapter 3

Dynamical fluctuations in particle production

In the study of fluctuations it is important to disentangle statistical and non-statistical fluctuations originating from dynamical processes. Since the observed number of particles in a heavy-ion collision is limited, the statistical background may dominate over the dynamical fluctuation signal. Also, comparing different centralities, collision species etc., the levels of statistical fluctuations are changing.

There are several ways to address this issue. A sensitive approach to the study of fluctuations in the kaon (or proton) to pion ratio is to look at the distribution of the difference in relative multiplicity [49], given by equation 3.1 for pion and kaon multiplicities, K and π .

$$\Delta n(K, \pi) = \frac{K}{\langle K \rangle} - \frac{\pi}{\langle \pi \rangle} \quad (3.1)$$

The mean value of this distribution is zero by definition. It can be characterized by its variance:

$$\nu(K, \pi) = \left\langle \left(\frac{K}{\langle K \rangle} - \frac{\pi}{\langle \pi \rangle} \right)^2 \right\rangle = \frac{\langle K^2 \rangle}{\langle K \rangle^2} + \frac{\langle \pi^2 \rangle}{\langle \pi \rangle^2} - 2 \frac{\langle K \pi \rangle}{\langle K \rangle \langle \pi \rangle}. \quad (3.2)$$

If the particle production is uncorrelated there will only be statistical fluctuations. In this case the variance in equation 3.2 is reduced to:

$$\nu_{stat}(K, \pi) = \frac{1}{\langle K \rangle} + \frac{1}{\langle \pi \rangle}. \quad (3.3)$$

The dynamical fluctuations can then be calculated as $\nu_{dyn} = \nu - \nu_{stat}$ according to equation 3.4.

$$\nu_{dyn}(K, \pi) = \frac{\langle K(K-1) \rangle}{\langle K \rangle^2} + \frac{\langle \pi(\pi-1) \rangle}{\langle \pi \rangle^2} - 2 \frac{\langle K \pi \rangle}{\langle K \rangle \langle \pi \rangle} \quad (3.4)$$

This is a measure of fluctuations in the absolute number of particles in the event and will therefore be more sensitive to fluctuations in high-multiplicity events. When no dynamical fluctuations are present ν_{dyn} should be zero since it is insensitive to statistical fluctuations. This holds regardless of the underlying multiplicity distribution. Derivations of relations related to the properties and interpretation of ν_{dyn} can be found in the included paper on *Number-ratio fluctuations in high-energy particle production*. In order to confirm these predictions and to better understand the behaviour of ν_{dyn} under different circumstances some elucidating simulation tests were done.

3.1 Fluctuation models

Event samples including non-statistical fluctuations have been generated using two different methods, with and without correlated particle production.

3.1.1 Method 1

In the first method, method 1, two samples with slightly different probabilities that a given particle is a kaon, $\mathbb{P}_1(K)$ and $\mathbb{P}_2(K)$, are mixed together. Both samples lack dynamical fluctuations when analysed individually, but when mixed together positive non-statistical fluctuations are created. This could be the case if the events in a sample are of two types with different kaon cross-section, with and without QGP formation for instance.

For an event sample generated following method 1, ν_{dyn} is described by equation 3.5, provided the two samples have the same multiplicity distribution.

$$\nu_{dyn} = \frac{\langle M(M-1) \rangle}{\langle M \rangle^2} \frac{\xi(1-\xi)(\Delta\mathbb{P}(K))^2}{\overline{\mathbb{P}(K)}^2 \overline{\mathbb{P}(\pi)}^2} \quad (3.5)$$

where $M = \pi + K$ is the total multiplicity. Here ξ and $1-\xi$ are the fraction of events belonging to the two samples, respectively. $\overline{\mathbb{P}(K)}$ and $\overline{\mathbb{P}(\pi)}$ are the overall mean kaon and pion probabilities in the mixed sample given by

$$\overline{\mathbb{P}(K)} = \xi\mathbb{P}_1(K) + (1-\xi)\mathbb{P}_2(K) \quad (3.6)$$

$$\overline{\mathbb{P}(\pi)} = \xi\mathbb{P}_1(\pi) + (1-\xi)\mathbb{P}_2(\pi) \quad (3.7)$$

and

$$\Delta\mathbb{P}(K) = \mathbb{P}_2(K) - \mathbb{P}_1(K). \quad (3.8)$$

3.1.2 Method 2

In the other method, method 2, particle pairs are created. Given kaon and pion probabilities, $\mathbb{P}(K)$ and $\mathbb{P}(\pi)$, in a sample of only kaons and pions, $\mathbb{P}(K) + \mathbb{P}(\pi) = 1$, the probability of a kaon pair is $\mathbb{P}^2(K)$, the probability of a pion pair is $\mathbb{P}^2(\pi) = (1 - \mathbb{P}(K))^2$ and the probability of a mixed pair is $2\mathbb{P}(K)(1 - \mathbb{P}(K))$, if the particle production is uncorrelated. Both positive and negative non-statistical fluctuations can be introduced by adding a correlation parameter, ε , to these probabilities as shown below.

$$\mathbb{P}(\pi + \pi) = \mathbb{P}^2(\pi) + \varepsilon \quad (3.9)$$

$$\mathbb{P}(K + K) = \mathbb{P}^2(K) + \varepsilon \quad (3.10)$$

$$\mathbb{P}(\pi + K) = 2\mathbb{P}(K)(1 - \mathbb{P}(K)) - 2\varepsilon \quad (3.11)$$

In this case, ν_{dyn} is described by equation 3.12.

$$\nu_{dyn} = \frac{\varepsilon}{\langle M \rangle \mathbb{P}^2(\pi) \mathbb{P}^2(K)} \quad (3.12)$$

where M is the total multiplicity.

3.2 Random number generators

Simulations were first attempted using a random number generator integrated in the ROOT [51] framework. This resulted in some unexpected results which lead to further investigations of the influence of the implementation of pseudo random number generators when performing demanding simulations.

Thus, given the high sensitivity of the ν_{dyn} measure, the choice of a random number generator for simulation work needs special attention. Two random number generators based on very different principles, which we can call *pirand* and *urandom*, have been implemented for testing purposes.

Pirand is a type of simple pseudo random number generator (PRNG). As such it is deterministic, given the same input value, or seed, it will always return the same sequence. This is useful when testing a Monte Carlo program with different conditions. Although the numbers are given by the predetermined sequence, they appear to be random as long as a value is returned which have not been used before. When this happens it will recycle the same numbers again. The length of the cycle is called the period.

Pirand in its basic form is described by equation 3.13.

$$a_{x+1} = (\pi + a_x)^3 - \lfloor (\pi + a_x)^3 \rfloor \quad (3.13)$$

where a_x is a value between zero and one. It has nice random properties but has a very limited period of the order 10^6 . In order to increase the period we combine two similar recursive subroutines, one using the power of three as in equation 3.13 and one using the power of four, which will produce two independent random numbers in the range (0,1). We can label them a and b . These two numbers are then added together and the generator returns the fractional part of their sum as given by equation 3.14.

$$r_{x+1} = a_{x+1} + b_{x+1} - \lfloor a_{x+1} + b_{x+1} \rfloor \quad (3.14)$$

If the periods of the two subroutines are relative prime numbers with respect to each other the combined generator will have a much longer period given by the multiplication of these numbers.

Urandom is a semi random generator that makes use of the entropy pool on the Linux system, which gathers environmental noise from device drivers and other sources. Random numbers are created via *dev/urandom*. It is not a true random number source since it returns numbers even if the entropy in the pool is low but it is a good source of true randomness assuming the entropy to be high. It is not as perfectly random as for example radioactive decays or atmospheric noise, since there is a risk that some repetitive component is contributing to the entropy pool, but under normal conditions it should be a good substitute.

Simulations are also performed using the boost c++ library PRNG, mt19937. It is an implementation of a Mersenne twister [52] which is supposed to be sensibly parametrized. It has a period of $2^{19937} - 1$ and good random properties.

In conclusion, results agree for all three generators and the combined *pirand* algorithm performs well as long as the seed is chosen with care to ensure long enough periods. The basic *pirand* implementation in all its simplicity is a nice tool for generating a limited number of random numbers.

3.3 Simulation results

The fluctuations produced by the two methods outlined above have very different properties. In order to obtain comparable results both methods are tested for different input parameters. For this purpose a fixed multiplicity, $M=100$ and an overall mean kaon probability of 10% is used in approximate accordance with experimental results, cf. figure 1.6. Figure 3.1 shows the

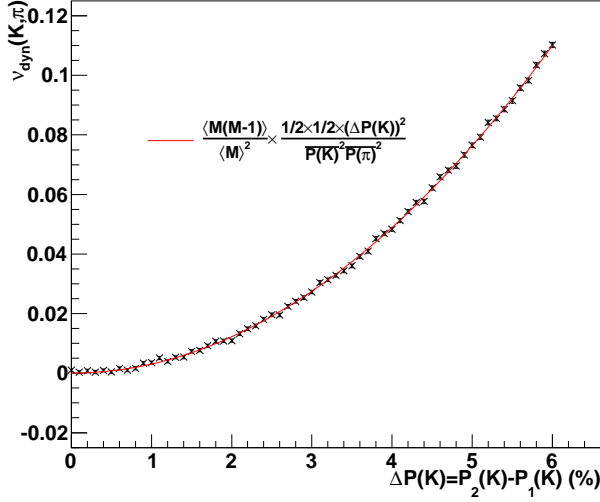


Figure 3.1: Method 1. Variation of ν_{dyn} with different kaon probabilities. The multiplicity is fixed at $M=100$. Kaon probabilities start at 10% for both samples. The kaon level is then decreased step-by-step to 7% for sample 1, $\mathbb{P}_1(K)$, and increased by equal amount for sample 2, $\mathbb{P}_2(K)$, to a maximum of 13%.

resulting fluctuation, ν_{dyn} , for method 1 with varying difference between the kaon probabilities, $\mathbb{P}_1(K)$ and $\mathbb{P}_2(K)$, of two samples containing the same number of events. Figure 3.2 shows ν_{dyn} as obtained with method 2 for varying correlation strength, ε . The fluctuation signal is proportional to the difference in kaon probabilities squared, $\Delta\mathbb{P}(K)^2 = (\mathbb{P}_2(K) - \mathbb{P}_1(K))^2$ for method 1 and proportional to the correlation strength for method 2 in accordance with the equations outlined in section 3.1.

Based on the results in figure 3.2 a correlation strength, $\varepsilon = 0.01$, is chosen as nominal input to method 2, which produces fluctuations that correspond to the level obtained by mixing two subsamples of events with kaon probabilities of 9 and 11%. The ν_{dyn} values obtained using these settings are also of roughly the same order as obtained in the data analysis. For the following results 100M events are produced for each data point, as opposed to figures 3.1 and 3.2 where only 100k events were generated.

3.3.1 Dependence on multiplicity

In the data analysis we study fluctuations as a function of the number of participating nucleons in the collision, which is directly proportional to the multiplicity.

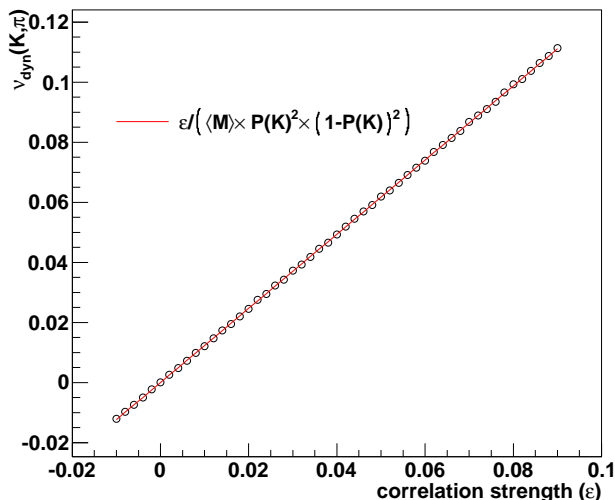


Figure 3.2: Method 2. Variation of ν_{dyn} with ϵ for a fixed kaon probability, $\mathbb{P}(K) = 10\%$ and fixed multiplicity, $M=100$.

Figure 3.3 shows the fluctuation signal as a function of multiplicity. For method 1, the level of fluctuations depends only weakly on multiplicity, cf. equation 3.5. The proportionality between the signal and the inverse multiplicity for model 2 resembles the multiplicity dependence seen in data and is typical of a physical process that scales with the multiplicity. Since the combinatorial background scales with the multiplicity squared, the signal to background ratio will scale as $M/M^2 = 1/M$. For the remaining simulation studies we use model 2.

3.3.2 Detection efficiency

Not all particles are observed when conducting experiments, because of limited acceptance and detection efficiency. The detection efficiency is normally different for different particle types. The detection efficiency may also vary with the momentum of the particles, depending on the properties of the detector and the life-time of the particles. Kaons, for example, tend to decay before they hit the detector, in which case they are not correctly identified. The probability for the kaon to decay in-flight before detection is higher at low momentum. In order to obtain reliable results it is useful to have an observable that is independent of these effects. A reduced detection efficiency has been simulated by randomly rejecting particles. Figure 3.4 shows ν_{dyn} as a function of detection probability, decreased by equal amounts for both pions and kaons. In figure 3.5 only the kaon detection probability is reduced, mimicking losses due to decays, while pions

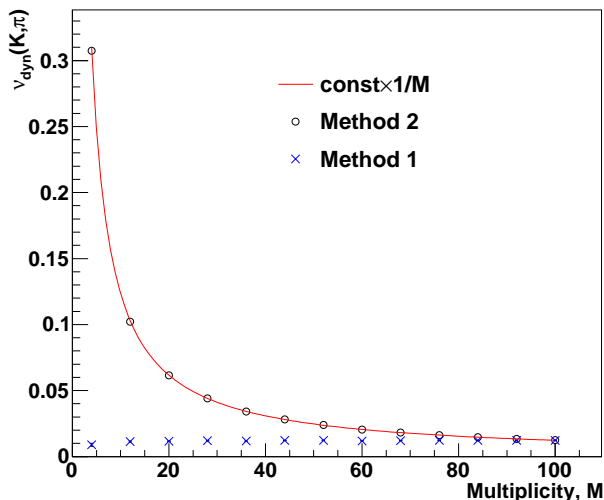


Figure 3.3: Multiplicity dependence of ν_{dyn} for the two methods of simulating fluctuations, with parameters chosen such as to obtain the same ν_{dyn} values at the highest multiplicity. The sample produced by method 1 uses kaon probabilities of 9 and 11% for the two subsamples, respectively. The sample produced by method 2 uses a fixed kaon probability, $\mathbb{P}(K) = 10\%$, with a correlation factor, $\varepsilon = 0.01$.

are detected to 100%. This demonstrates that the fluctuation signal is independent on the detection efficiency, even if it differs for the two particle types, provided that the loss process is purely random.

3.3.3 Azimuthal acceptance

If a limited acceptance only reduces the number of observed particles randomly, this should not affect the fluctuation signal since the ratio of true pairs to combinatorial background remains constant. However, this is not the case if particle pairs are produced with a correlated angular distribution, as would for example be the case for resonance decay products. Figure 3.6 shows the simulated fluctuations as a function of azimuthal acceptance for the three extreme cases where there is no angular correlation, all particles are produced pairwise back-to-back in azimuth and all particles are pairwise aligned in azimuth. This illustrates clearly the fact that if particles in a pair are emitted in directions close to each other, a limited acceptance will tend to either keep or reject both particles. Since the combinatorial background is reduced with the acceptance we will observe increased fluctuations which are inversely proportional to the number of observed particles. As a contrast, if particles in a pair are emitted in op-

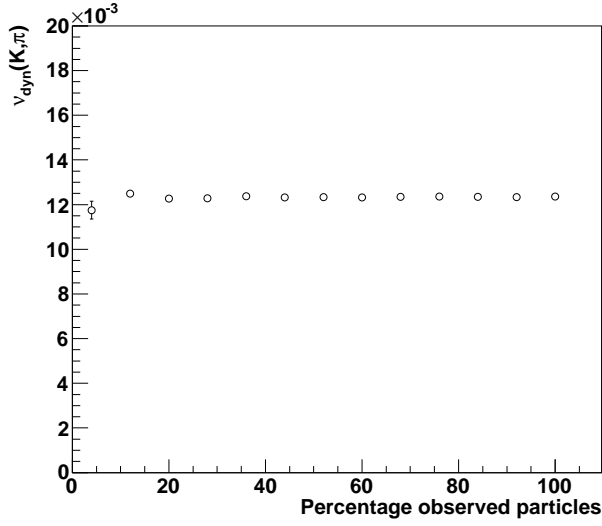


Figure 3.4: Dependence of $\nu_{dyn}(K, \pi)$ on particle detection efficiency with the same probability for detecting both kaons and pions.

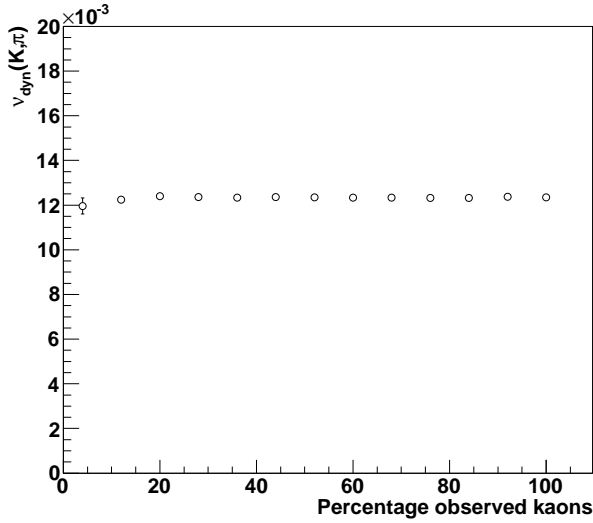


Figure 3.5: Dependence of $\nu_{dyn}(K, \pi)$ on reduced kaon detection efficiency with 100% probability for detecting pions.

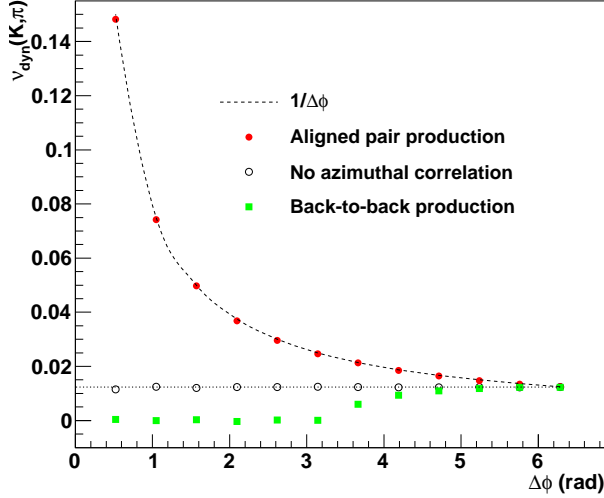


Figure 3.6: ν_{dyn} as a function of azimuthal acceptance for particle pairs produced back-to-back (filled squares), aligned (filled circles) and randomly distributed in the azimuthal space (open circles).

posite directions, a limited acceptance will tend to break all pairs and the fluctuation signal disappears. If there is no azimuthal correlation between particles there is no effect on the observed signal.

A varying angular correlation has also been simulated. First the created particles are randomly distributed in azimuth. Then the opening angle between two particles in a pair, $\Delta\phi$, is increased or decreased by some fraction of $\Delta\phi$ that depends on the value of the azimuthal correlation strength factor, α_ϕ , ranging from -1 to 1, according to:

$$\Delta\phi = \Delta\phi - \alpha_\phi\Delta\phi. \quad (3.15)$$

Thus, $\alpha_\phi = -1$ means that all particles are pairwise produced back to back and $\alpha_\phi = 1$ means that all particles are pairwise aligned. Figure 3.7 shows the fluctuation signal as a function of azimuthal correlation, for a fixed azimuthal acceptance of 180° .

3.3.4 Misidentification

When a particle is assigned an identity in the analysis, there is always a certain risk that the assignment is wrong. The level of misidentification depends on how stringent the criteria are for particle identification. The effect of misidentification on the fluctuation signal varies for different particle types, depending on their relative multiplicities as can be seen from

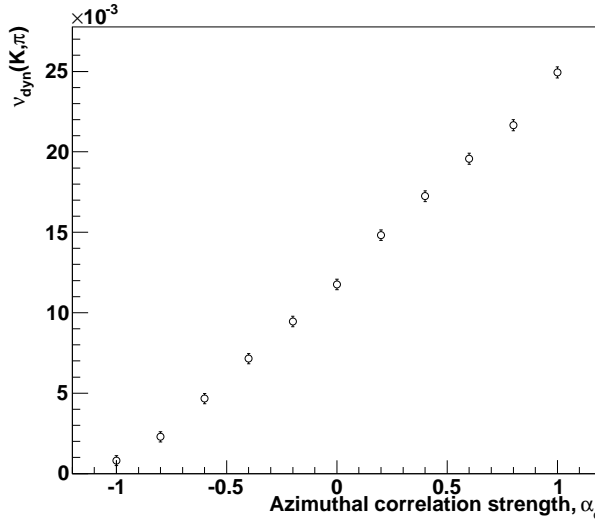


Figure 3.7: ν_{dyn} as a function of the strength of the azimuthal correlation, α_ϕ , for a fixed acceptance of 180° .

figure 3.8, where the effect was simulated by randomly assigning the wrong particle types. The effect on the signal is small if a particle is wrongly assigned the identity of the dominating particle species. However, if a particle is wrongly assigned the identity of the species which is underrepresented, as the kaon in this case, the signal is noticeably reduced. Therefore it is crucial for the analysis to correctly identify kaons.

3.3.5 Ghost tracks

Ghost tracks have been introduced in the sample by randomly double-counting tracks. Figure 3.9 shows the multiplicity dependence of the effect on ν_{dyn} for a fixed ghost level of 5%. The effect grows with reduced multiplicity as can be expected for a signal which is proportional to the multiplicity. If instead the ghost level is proportional to the multiplicity, which may be a more realistic scenario considering that the tracking becomes increasingly difficult with an increasing number of hits in the detector, the result will be a constant shift of the signal as shown in figure 3.10. The latter case resembles the effect seen in the data, cf. figure 6.17.

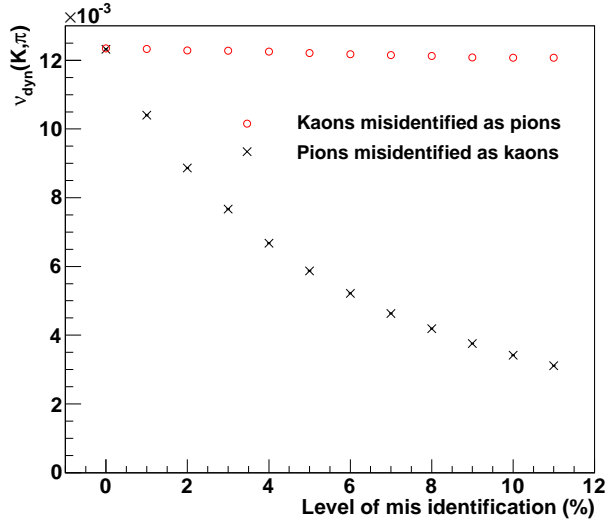


Figure 3.8: ν_{dyn} as a function of the level of misidentification for a fixed underlying event multiplicity, $M=100$, $\mathbb{P}(K) = 10\%$ and $\varepsilon = 0.01$.

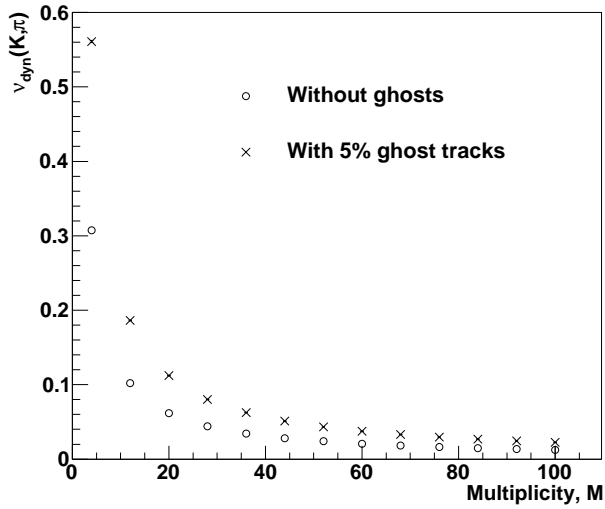


Figure 3.9: Multiplicity dependence of the ghost track effect for a constant ghost fraction.

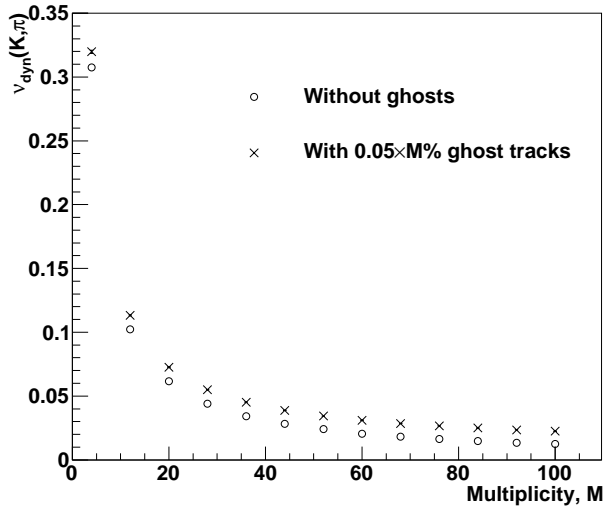


Figure 3.10: Multiplicity dependence of the ghost track effect for a ghost fraction that is proportional to the multiplicity.

Chapter 4

Fluctuations in physical models

In this simulation study Hijing [53] is used to produce events from Gold-Gold collisions at $\sqrt{s_{NN}} = 200$ GeV. The aim is to obtain an understanding of the expected level of fluctuations due to the contributions from particle decays and from fundamental conservation laws.

4.1 Hijing

Hijing (Heavy-Ion Jet INteraction Generator) is an event generator for high-energy hadron-hadron (pp), hadron-nucleus (pA) and nucleus-nucleus (AA) collisions. It uses subroutines from PYTHIA [55] and JETSET [56] in order to obtain a full event description. PYTHIA is used to describe the kinematics of hard scatterings and associated radiation, while JETSET is used to describe the string fragmentation. The effect of flow is not included in Hijing. Particle correlations due to boson interferometric effects, so called HBT, are also not accounted for in Hijing.

4.2 Event selection

For the comparison with data shown in chapter 8, events are produced at three different centralities: central (0-5%), mid-central (30-35%) and peripheral (65-70%). The centrality selection is made by setting limits on the impact parameter in Hijing. To determine these limits a subset of minimum-bias events was produced, which contains all centralities according to the nuclear geometry. From the distribution of impact parameters

of these events, the frequency of events with impact parameter, b_i , less than b as a function of b is obtained. The requested limits as given by this distribution are: $b < 3.4$ fm for central events, $8.4 < b < 9$ fm for mid-central events and $12.3 < b < 12.8$ fm for peripheral events, as displayed in figure 4.1.

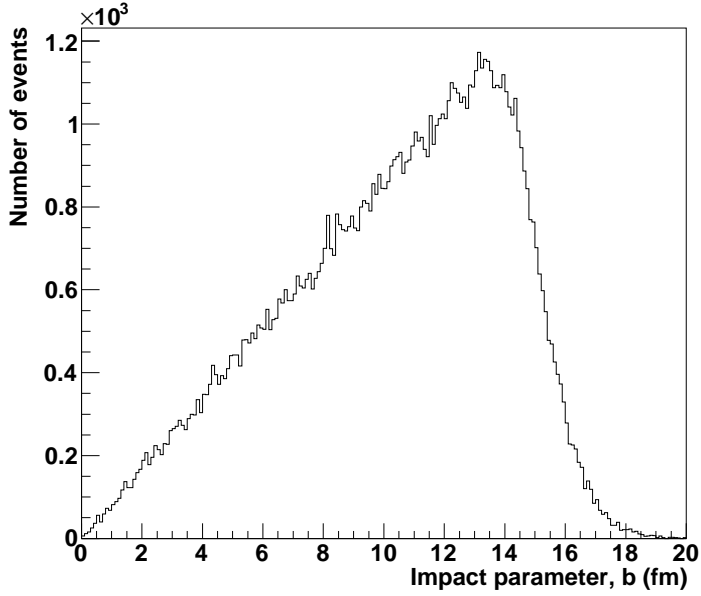
4.3 Particle decays

A number of particle decays contribute to the production of pairs of pions, kaons and protons. Meson resonances like ρ , η , ω and ϕ all decay within nuclear dimensions, since they are strong decays. They produce different combinations of pions and kaons and should therefore influence the observed fluctuations. The most important of these decays is $\phi \rightarrow K^+ + K^-$ which will enhance the fluctuations in K to π . As discussed in chapter 3, one K^+K^- pair will give a relatively larger positive contribution to the observed fluctuation than a $\pi^+\pi^-$ pair due to the small K/π ratio.

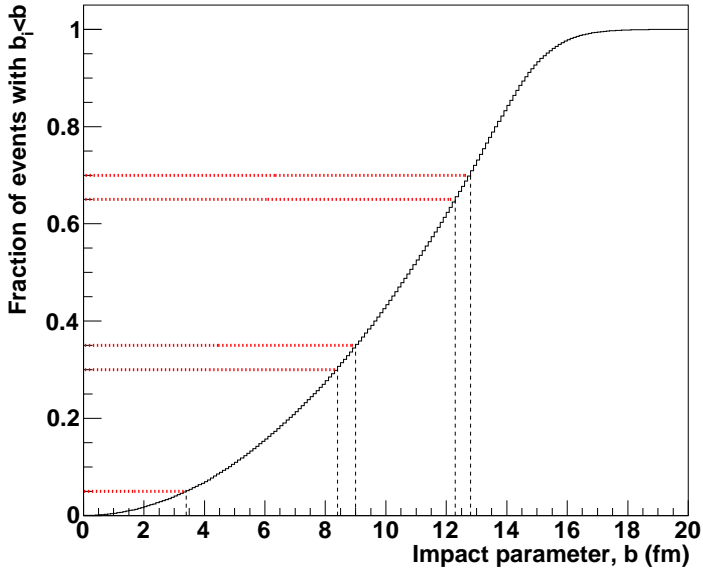
The dominating contributions from decays to $\nu_{dyn}(p, \pi)$ are the strong Δ -resonance decays, which result in $p\pi$ pairs of different charge-state combinations depending on the type of Δ . There will also be feed-down contributions from weak baryon decays, including Ω , Ξ , Σ and Λ . At the end of this decay chain the dominating decay mode is $\Lambda \rightarrow p\pi^-$ ($\bar{\Lambda} \rightarrow \bar{p}\pi^+$), which will decrease the measured fluctuations in the p to π ratio. The effects of these decays in the experimental data can be seen in figures 8.9 and 8.10. Table 4.1 lists the most important contributing decays. One should remember that particles appearing in subsequent generations of a decay chain are also correlated in the particle number. However, their kinematical properties are not closely related since they come from different decays.

4.4 Results of the Hijing simulation

Four samples of Hijing events have been generated, each containing 10 000 events: the first with all relevant decays turned off; the second with only Δ -decays turned on; the third including also meson decays and the fourth with the additional inclusion of weak baryon decays, i.e. with all relevant decays turned on. Figures 4.2 and 4.3 show the relative abundances, in the full acceptance, of the different particle species listed in table 4.1, observed in the sample of central events with all decays turned off.



(a) Distribution of impact parameter, b , for 100k Gold-Gold minimum-bias events.



(b) Summed impact parameter distribution normalized to the maximum value. Horizontal lines mark the selected bins of centrality for this analysis and the vertical lines give the corresponding values of the impact parameter, used in the Monte Carlo production.

Figure 4.1: Event centrality and impact parameter selection.

Particle	Pseudoscalar mesons	p (MeV/c)
η'	$\rightarrow \pi^+ + \pi^- + \eta$	232
	$\rightarrow \pi^0 + \pi^0 + \eta$	239
η	$\rightarrow \pi^+ + \pi^- + \pi^0$	174
K_S^0	$\rightarrow \pi^+ + \pi^-$	206
Vector mesons		
ϕ	$\rightarrow K^+ + K^-$	127
	$\rightarrow K_S^0 + K_L^0$	110
	$\rightarrow \rho + \pi + \pi^+ + \pi^- + \pi^0$	-
ω	$\rightarrow \pi^+ + \pi^- + \pi^0$	327
ρ^0	$\rightarrow \pi^+ + \pi^-$	364
Strong baryon decays		
$\overline{\Delta}^{++}$	$\rightarrow \bar{p} + \pi^-$	229
$\overline{\Delta}^0$	$\rightarrow \bar{p} + \pi^+$	229
Δ^{++}	$\rightarrow p + \pi^+$	229
Δ^0	$\rightarrow p + \pi^-$	229
Weak baryon decays		
$\overline{\Omega}^-$	$\rightarrow \overline{\Lambda} + K^+$	211
	$\rightarrow \overline{\Xi}^0 + \pi^+$	294
	$\rightarrow \overline{\Xi}^- + \pi^0$	290
$\overline{\Xi}^0$	$\rightarrow \overline{\Lambda} + \pi^0$	135
$\overline{\Xi}^-$	$\rightarrow \overline{\Lambda} + \pi^+$	139
$\overline{\Sigma}^0$	$\rightarrow \overline{\Lambda} + \gamma$	74
$\overline{\Lambda}$	$\rightarrow \bar{p} + \pi^+$	101
Ω^-	$\rightarrow \Lambda + K^-$	211
	$\rightarrow \Xi^0 + \pi^-$	294
	$\rightarrow \Xi^- + \pi^0$	290
Ξ^0	$\rightarrow \Lambda + \pi^0$	135
Ξ^-	$\rightarrow \Lambda + \pi^-$	139
Σ^0	$\rightarrow \Lambda + \gamma$	74
Λ	$\rightarrow p + \pi^-$	101

Table 4.1: List of the most frequent decays that may contribute to the measured fluctuations [1]. p is the momentum of a decay product in the rest frame of the decaying particle.

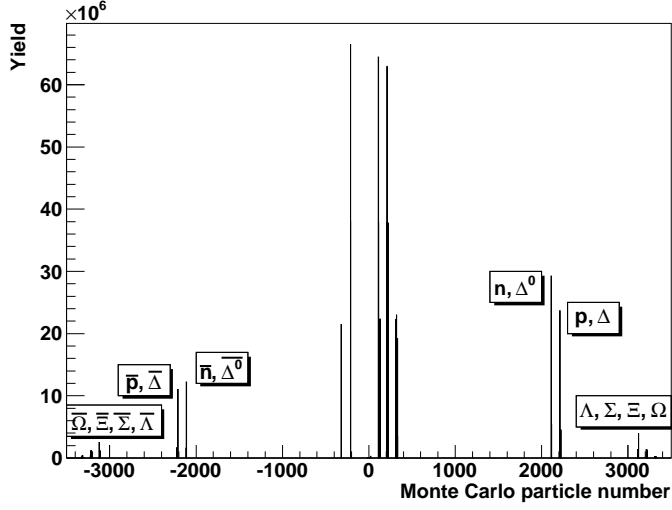


Figure 4.2: Total abundances of particles species in the sample of central Hijing events, identified via their Monte Carlo number.

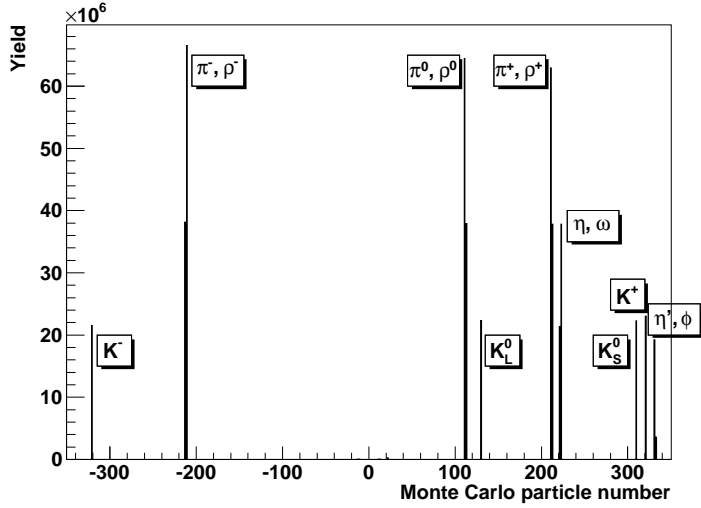
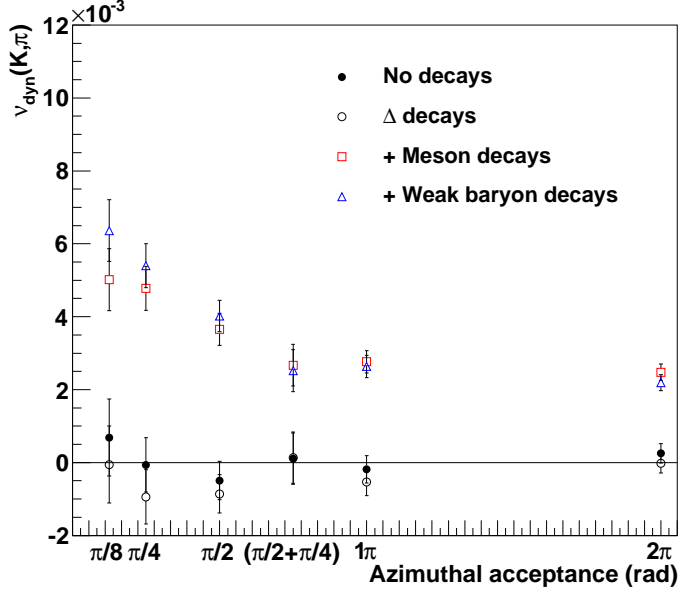


Figure 4.3: Zoom in at small Monte Carlo numbers in figure 4.2.

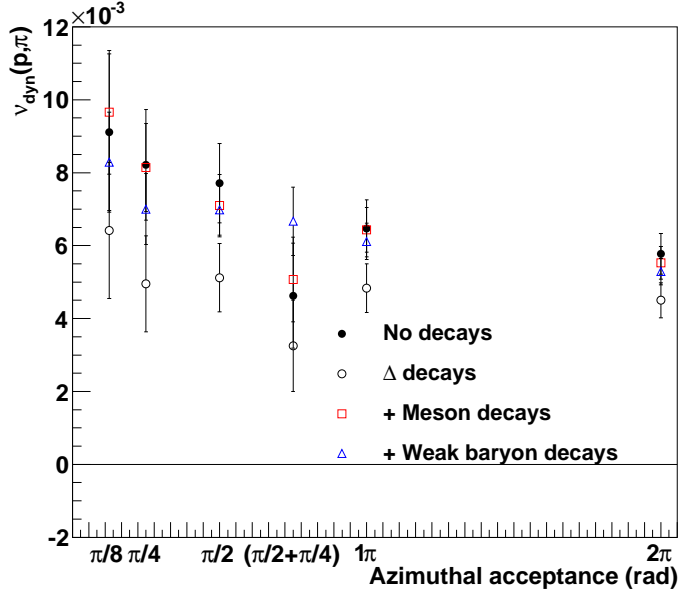
The samples have been analysed at mid-rapidity, $|\eta| < 0.35$, for azimuthal bins of varying size, the smallest bin of $\pi/8$ radians (or 22.5°) corresponding to one sector in the PHENIX central arm detector. The effect of decays on the fluctuation measure can be studied in figure 4.4, for particles with transverse momenta in the range used for particle identification with the EMCal detector in the data analysis of this study. The top picture shows $\nu_{dyn}(K, \pi)$. In the absence of decays there are no measurable fluctuations present. As expected, the Δ -decays do not affect $\nu_{dyn}(K, \pi)$ much. The meson decays introduce positive fluctuations which are only slightly reduced by the inclusion of weak baryon decays. This latter decrease is likely due to the increased particle production from decays which produces a larger uncorrelated background.

The bottom picture shows $\nu_{dyn}(p, \pi)$ which displays a slightly different behaviour. There are non-statistical fluctuations present even though all decays listed in table 4.1 are turned off. When the delta decays are introduced $\nu_{dyn}(p, \pi)$ decreases as expected. The positive contribution from meson decays partially compensates this decrease, while the weak baryon decays give an additional negative contribution similar to the delta decays.

The simulated events are also analysed as a function of transverse momentum, for a sample with all decays turned on. The result is showed in figure 4.5 for the full azimuthal acceptance, for one that corresponds to the EMCal acceptance of the PHENIX detector and for one that corresponds to the acceptance of one sector of the EMCal, or TOF, in the central arms, see chapter 5. With a full azimuthal coverage ν_{dyn} is stable over the full range of transverse momentum. There is no significant difference between the full azimuthal acceptance and the EMCal acceptance. In contrast, there is a clear increase at higher momenta for both $\nu_{dyn}(K, \pi)$ and $\nu_{dyn}(p, \pi)$, when measured in only one sector. This can be understood as an increased probability for both particles in a pion or kaon pair from meson decays to be detected in the same sector and the same p_T bin. As the multiplicity decreases exponentially with increased momentum the combinatorial background reduces, so the signal to background ratio also improves for higher momenta.

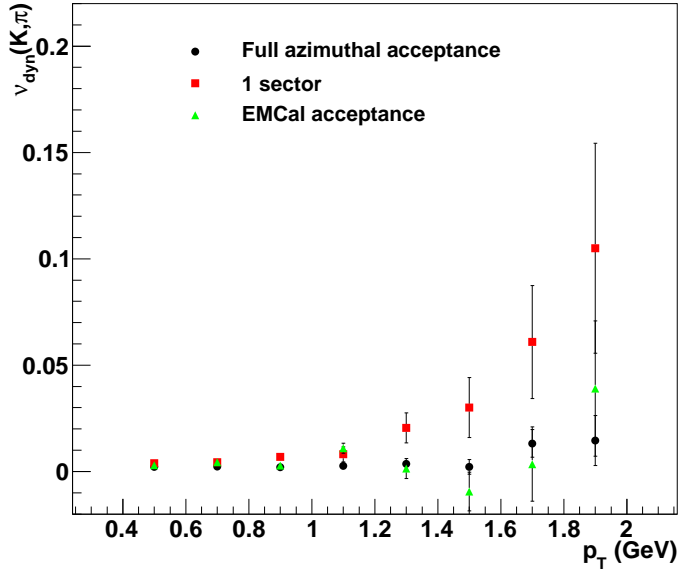


(a) $\nu_{dyn}(K, \pi)$

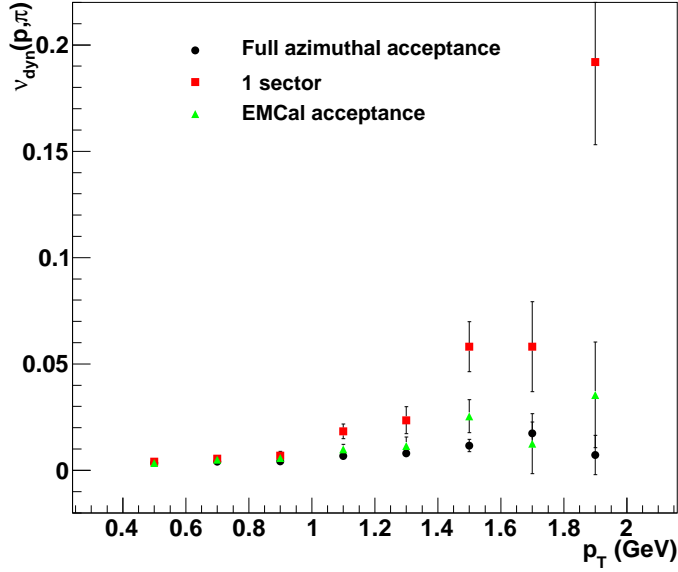


(b) $\nu_{dyn}(p, \pi)$

Figure 4.4: ν_{dyn} at mid-rapidity ($|\eta| < 0.35$) in simulated Gold-Gold central (0 – 5%) Hijing events for four cases; no decays, only Δ decays, Δ decays plus strong meson decays and the last one including also weak baryon decays, as a function of azimuthal acceptance for particles with $0.4 < p_T < 1.0$ GeV for pions and kaons and $0.6 < p_T < 2.0$ GeV for protons. The acceptance $\pi/2 + \pi/4$ corresponds to the full ECal azimuthal acceptance.



(a) $\nu_{dyn}(K, \pi)$



(b) $\nu_{dyn}(p, \pi)$

Figure 4.5: ν_{dyn} at mid-rapidity ($|\eta| < 0.35$) as a function of momentum, in simulated Gold-Gold central (0-5%) Hijing events with all decays turned on, for varying azimuthal acceptance.

Chapter 5

The PHENIX experiment

The Pioneering High-Energy Nuclear-Interaction eXperiment, PHENIX, is operating at one of the collision points at the Relativistic Heavy-Ion Collider, RHIC. RHIC collides ions, from protons to Gold, up to a centre-of-mass energy per primary nucleon-nucleon collision, $\sqrt{s_{NN}}$, of 200 GeV for ions and 500 GeV for protons.

The highest energy Gold-Gold collisions are mainly used to study the quark-gluon plasma. An energy scan down to the lowest energy possible was undertaken in order to study the energy dependence and search the QCD phase diagram for the onset of deconfinement. Collisions with lighter ions are used to study the geometry dependence. Deuteron-Gold and proton-proton collisions, where no QGP is formed, are used as control experiments for reference. Polarized proton beams provide the possibility to study the spin structure of the proton.

Table 5.1 summarizes the collisions produced at RHIC during the first ten years of running. Collisions realized in earlier runs have been repeated in later runs, following upon detector upgrades or in order to collect larger data volumes. The data analysed in this thesis were collected during the Gold-Gold run of 2003-2004.

5.1 The Relativistic Heavy-Ion Collider facility

The Relativistic Heavy-Ion Collider, RHIC, is a dedicated heavy-ion accelerator facility at Brookhaven National Laboratory on Long Island in New York. From the start it hosted four experiments: PHENIX, STAR, BRAHMS and PHOBOS. The two smaller experiments, PHOBOS, which specialized in forward rapidity measurements, and BRAHMS which measured hadron spectra in a wide angular range, are now terminated. Both

	Period	Species and collision energy $\sqrt{s_{NN}}$ (GeV)
Run 1	2000	Au+Au 130
Run 2	2001–2002	Au+Au 200, p+p 200
Run 3	2002–2003	d+Au 200, p+p 200
Run 4	2003–2004	Au+Au 200 and 62.4, p+p 200
Run 5	2004–2005	Cu+Cu 200, 62.4 and 22.5, p+p 200
Run 6	2005–2006	p+p 200, 62.4
Run 7	2006–2007	Au+Au 200
Run 8	2007–2008	d+Au 200, p+p 200
Run 9	2008–2009	p+p 500, 200
Run10	2009–2010	Au+Au 200, 62.4, 39, 7.7

Table 5.1: RHIC operations from the start in year 2000 to the end of run 10 in 2010 [19]

PHOBOS and BRAHMS had small acceptance but high resolution inside this acceptance. In contrast, the two larger, general purpose experiments, PHENIX and STAR, are both undergoing major upgrades for several additional years of operation.

The ions acquire their high energy by passing through a chain of accelerators as shown by figure 5.1. The first accelerator in line is a Tandem Van de Graaff, which uses static electric fields to first accelerate negatively charged ions ($q=-e$), which are then turned into positively charged ions as they are stripped of two atomic electrons, before they are accelerated over a second potential drop to an energy of ~ 1 MeV/u, or approximately 5% of the speed of light.

Then the ions are guided by a beam transfer line to the Booster Synchrotron. Protons, polarized or not, are injected directly into the Booster Synchrotron from a 200 MeV Linac. In the Booster Synchrotron the ions will be accelerated to 95 MeV/u or 37% of the speed of light. A foil at the Booster exit strips all remaining electrons, except the most tightly bound, before they are feed into the Alternating Gradient Synchrotron, which will accelerate them further up to a maximum energy of ~ 10 GeV/u, or 99.7% of the speed of light.

The remaining electrons are stripped off before, finally, bunches of fully ionized ions are injected into the two RHIC rings, in which the ions are circulating in opposite directions. After additional acceleration of the ions in the RHIC to the desired collision energy, ion bunches from the two rings are brought to collide at the six ring crossings [20].

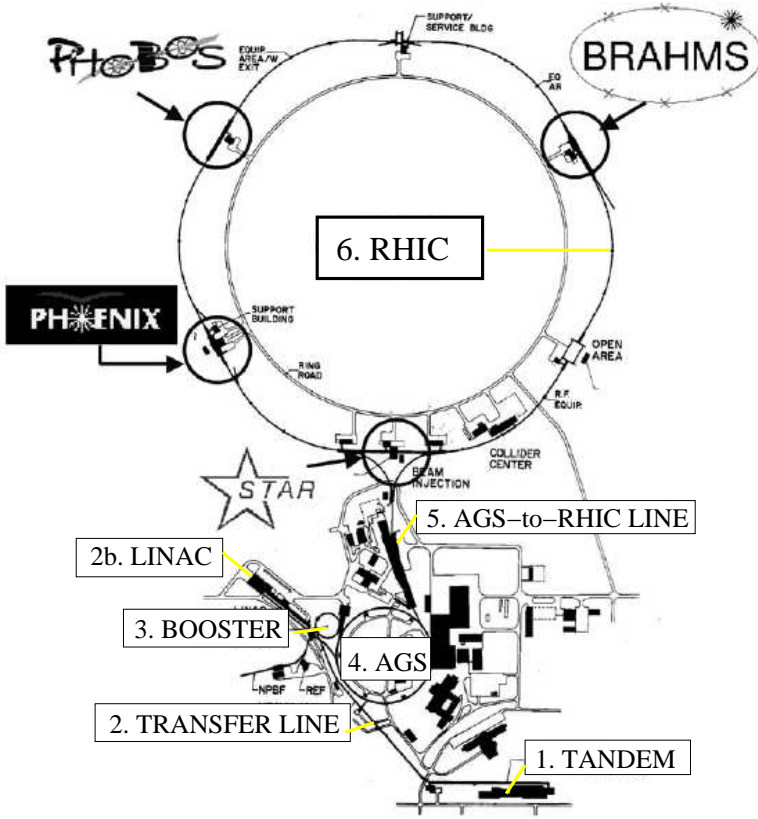


Figure 5.1: RHIC accelerator complex showing the Tandem Van de Graaff (1), the Tandem-to-Booster line (2), the Linear Accelerator (2b), the Booster Synchrotron (3), the Alternating Gradient Synchrotron (4), the AGS-to-RHIC line (5) and RHIC (6) [21].

5.2 Overview of the PHENIX detector system

Figure 5.2 displays the PHENIX detector configuration for Run 4, which forms the basis of the data analysed in this thesis. The collision point is surrounded by the central magnet, which provides a longitudinal magnetic field in the direction of the beam line, and the two central spectrometer arms on opposite sides containing detectors for momentum measurement and for the identification of both charged particles and photons. The main components of the central arms are the Drift Chambers (DC), used for momentum determination of charged particles whose trajectories bend in the magnetic field, and the Pad Chambers (PC), used for tracking particles in three dimensions through to the system of detectors for particle identification. These are the Ring Imaging Čerenkov detector (RICH), the Time-of-Flight detector (TOF) and the Electromagnetic Calorimeter (EM-Cal, PbSc+PbGl). Each spectrometer arm covers 90° in azimuth. The arms are placed with 45° separation on the top and 135° at the bottom, thus allowing a smooth acceptance in relative angles for pairs of particles. The opening in theta angle is $\pm 20^\circ$ corresponding to ± 0.35 units of pseudo-rapidity.

Global detectors, used for the characterization of events, are situated along the beam line in both directions: the Beam-Beam Counters (BBC) and further away the Zero Degree Calorimeters (ZDC), after the dipole magnets. The dipole magnets serve the function of bringing the two beams to cross each other at the interaction point and bending non interacting ions back in orbit after passage of the interaction region.

Finally, two muon arms, consisting of a tracker component inside a magnetic field (MuTr) and an identifier (MuID), reaches out at larger rapidities in both directions extending the acceptance for detecting dilepton decays. The muon arms are not used in this analysis.

5.3 Detectors for global observables

These detectors are used to determine event characteristics, the time and position of the collision and the multiplicity of created particles at large rapidities. They are also used as fast hardware minimum-bias triggers to enable collection of an event. Information on the collision vertex position is provided by the Beam-Beam Counters, which also give the time of collision used as the start time of flight-time measurements [22]. For more peripheral collisions, where the main parts of the ion remnants continue forward without interaction, additional information is obtained from the Zero Degree Calorimeter which is used to detect free neutrons in a small

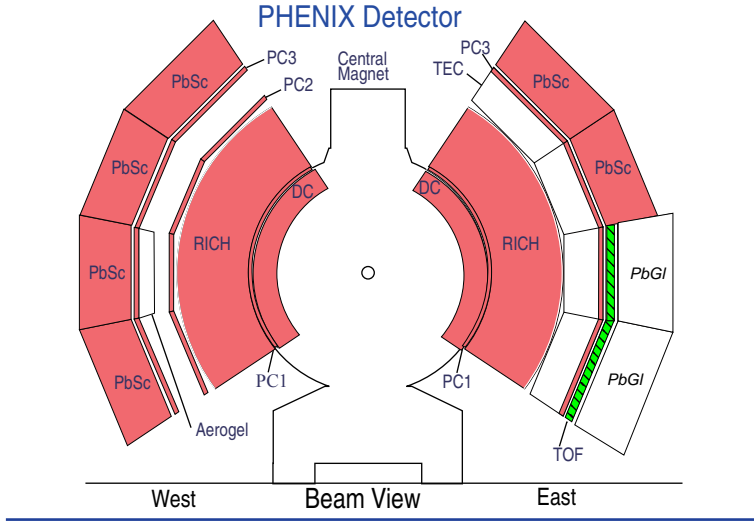


Figure 5.2: PHENIX detector configuration for Run 4. Detector subsystems used in this analysis are coloured.

cone around the beam direction [23]. In particular, combined information from the BBC and the ZDC is used to determine the centrality of a collision as described in section 6.3.

The Beam-Beam Counters The BBC's are situated around the beam pipe at a distance, $L=144$ cm, from the centre of the interaction region in both directions. Each BBC array contains 64 photomultiplier tubes, which detect Čerenkov light formed in a quartz layer mounted on top of the tube. The granularity of the BBC is moderate; normally a central heavy-ion collision produces multiple hits in each detector. The charge signal in a phototube will basically be proportional to the total track length through the quartz. Thus, the signal from a tube will be proportional to the number of particle hits in the quartz detector and the total charge sum, from all photomultiplier tubes, will be proportional to the total multiplicity in the pseudorapidity range covered by the BBC.

Based on detection of fast, $v \approx c$, charged particles, which all produce Čerenkov light, the BBC measures arrival times, T_N and T_S , in the north and south detector array. To avoid fake signals originating from detector noise, these are calculated as truncated means over particle hits in all BBC elements as:

$$T_{S/N} = \frac{1}{N} \sum_{i=1}^N t_i \quad (5.1)$$

Given the arrival times in BBC north and south, the position along the

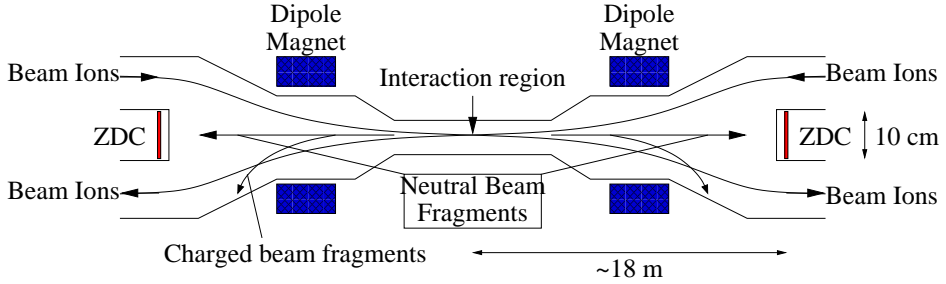


Figure 5.3: Position of the Zero Degree Calorimeter. Note that the transverse and longitudinal scales are very different.

beam axis, z_{vertex} , and the time of the interaction T_0 are given by:

$$T_0 = \frac{T_S + T_N}{2} - \frac{L}{c} \quad (5.2)$$

$$z_{vertex} = \frac{(T_S - T_N)}{2} \times c \quad (5.3)$$

The obtained collision time, T_0 , is used as start time for time-of-flight measurements on particles in the central arms with a resolution of 52 ps for individual modules in the BBC array. This will contribute to the flight-time resolution of the particle identifying detectors.

The Zero Degree Calorimeters The ZDC is a calorimeter used to determine the number of spectator neutrons in a collision, by measuring the total neutral energy within a cone of 2 mrad along the beam line in both directions. The detectors are placed at ~ 18 m from the interaction point, behind dipole magnets which deflect the beam ions and all charged remnants as described in figure 5.3. The ZDC consists of tungsten absorbers, in which the neutrons will start hadronic showers, interleaved with layers of sampling fibres, sensitive to the Čerenkov light emitted by charged shower secondaries. To enable efficient light collection, the layer structure is tilted at 45° to the beam in order to align the optical fibres with the Čerenkov angle for forward particles in the shower.

5.4 Tracking system

Both the Drift Chambers and the Pad Chambers, which are part of the PHENIX central arm tracking system [24], are gaseous detectors filled with a mixture of Argon and Ethane. As a charged particle crosses the gas volume, it will ionize the gas along its track and the created electrons and ions will drift towards the nearest anode and cathode, respectively. In the

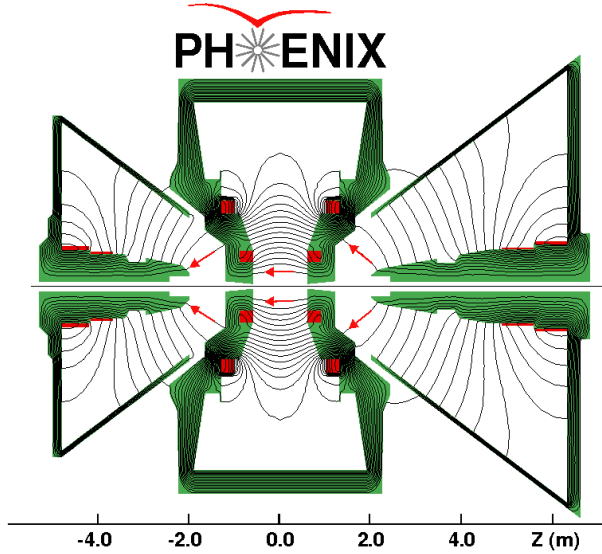


Figure 5.4: Longitudinal cut through the PHENIX magnet system with the field lines produced when the two central coils are run in the same direction [26].

close proximity of anode wires, the electrons will experience the radially increasing electric field strength. Then they will be accelerated and create an avalanche of secondary ionization, which produces signals that can be read out. Avalanche multiplication factors in excess of 10 000 are used in these detectors. Helium bags were installed between the beam pipe and the Drift Chambers during run 4, in order to reduce the amount of material in front of the tracking detectors. This is done for the sake of minimizing the conversion of γ that create electron background and to reduce multiple scattering of charged particles, which limits the momentum resolution, in particular at low momenta.

Central Magnet The central magnet consists of two concentric coils (inner and outer) that can be run separately, together or in opposite current directions, producing magnetic fields in the $\pm z$ direction. The aperture is $70 < \theta < 110^\circ$, which is also the acceptance of the central arm spectrometers. The maximum total integrated field strength at mid-rapidity is 0.78 Tesla-metres for the outer coil alone and from 0.43 (opposite current directions) to 1.15 Tesla-metres (same current directions) for both coils run together [25]. Figure 5.4 shows the field lines of the PHENIX magnets with both coils of the central magnet run in the same direction, which is the configuration used in this analysis. By reversing all currents, the field direction can be reversed which allows the study of charge dependencies in acceptance and efficiency.

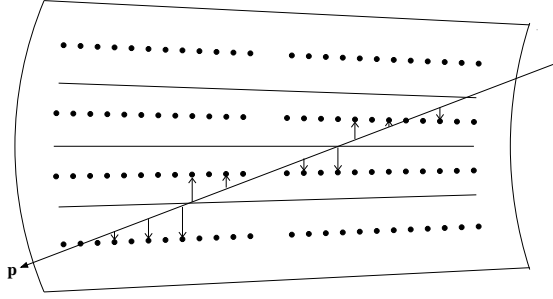
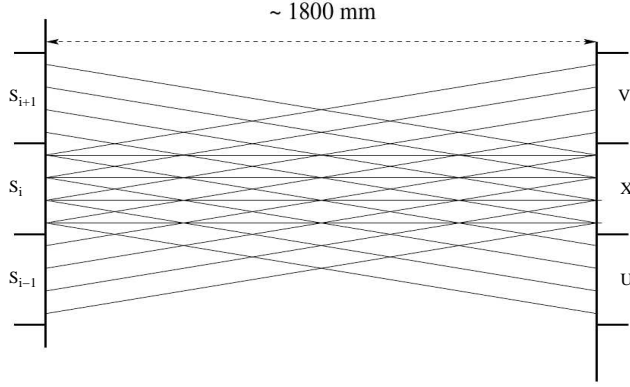


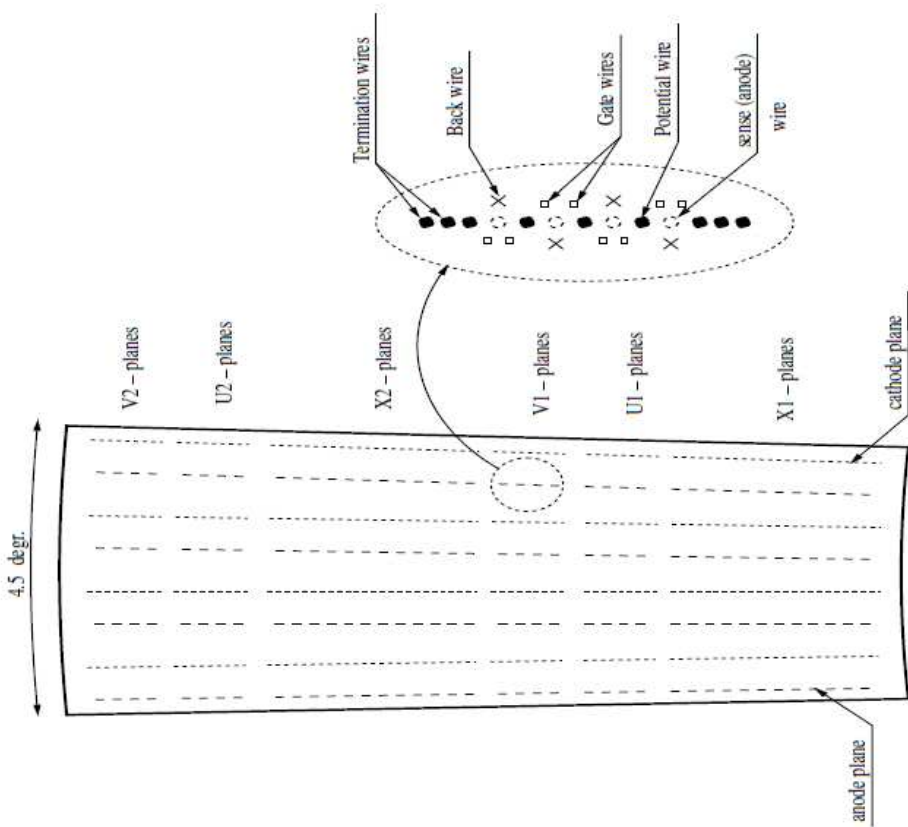
Figure 5.5: Principle of the DC geometry. Electrons from ionization along a particle trajectory, \mathbf{p} , drift towards anode wires in one Drift Chamber sector. Not to scale.

Drift Chambers The DC provides trajectories of charged particles by measuring two-dimensional space points in $r - \phi$ and $r - z$. The spacial coordinates are obtained from the drift times of the ionization electrons, as demonstrated in figure 5.5. Although the DCs are geometrically outside the magnet poles, the region still has a slight stray magnetic field.

The DC system consists of two detectors, one in each arm at a radius of 2.02 m to 2.46 m from the interaction point, with a length of 180 cm in the z -direction and an angular coverage of 90° in ϕ . Figure 5.6 shows the wire configuration of a DC sector. In each detector there are 80 planes of sense (anode) wires distributed in ϕ . Each plane contains two sets, X1 and X2, of twelve radially stacked wires running parallel to the beam. In addition, each plane contains two sets of wires, (U1, V1) and (U2, V2), with an inclination $\phi = \pm 4.5^\circ$ with respect to the X-wires. The U and V wires provide a z -coordinate. The anode wires are surrounded by gate and back wires, as shown in the detailed view of figure 5.6b. This is done in order to eliminate up-down ambiguities by collecting charge from only one side of each wire, with alternating up and down collecting wires. The wires are electrically divided in the middle, $z = 0$, and each half is read out independently at the end of the wire on either side of the detector, in order to minimize double hits in readout channels. This detector configuration results in a single wire spatial resolution of 0.15 mm, a nearby track resolution of 1.5 mm and a z -resolution of 2 mm at a radius of 2.25 m, which is the DC reference radius. Since the stereo wires are few, they will not always provide the z -coordinate for the track. Thus, the z -coordinate is determined from the combined information of the DC and PC systems.



(a) Longitudinal view (z) of one sector. Vertical and horizontal dimensions are not to scale.



(b) Transverse view.

Figure 5.6: Wire configuration in a DC sector consisting of four sense wire planes and four cathode wire planes. U and V wires start in one sector and end in the neighbouring sector as shown in (a) [24].

Pad Chambers The PCs are multi-wire proportional chambers that measure three dimensional spatial points on the straight line charged particle tracks outside the magnetic field.

The PC system consists of five individual detector planes, three in the west arm (PC1, PC2 and PC3) and two in the east arm (PC1 and PC3). The middle plane (PC2) in the east arm was removed from the construction for economical reasons. PC1 is situated just behind the DC at a radius, r , of 250 cm and provides the ϕ - and z -coordinate of the particles. PC2, at $r = 415$ cm, and PC3, situated just in front of the Electromagnetic Calorimeter at $r = 487$ cm, provide ϕ - z -coordinates of the straight tracks of the particles through the spectrometer arms, which enables a more reliable matching of the momentum measurement from DC with hits in other detectors used for particle identification.

Each PC detector contains one single plane of anode wires in the z -direction, sandwiched between two cathode planes, one of which is finely segmented and read out. For PC1 this yields a position resolution in z of ± 1.7 mm and a resolution in ϕ corresponding to the wire spacing of 8.4 mm. PC2 and PC3 are constructed so as to retain the same space angle resolution as PC1.

5.5 Detectors for particle identification

There are three main particle identifying detectors in the central arms. The Ring Imaging Čerenkov detector, RICH, is used to separate electrons from the large number of pions and the Time-of-Flight detector, TOF, is used to identify pions, kaons and protons [27]. The Electromagnetic Calorimeter, EMCal, can identify the same particles as the TOF over a larger acceptance but in a more limited momentum range due to poorer timing resolution. EMCal is primarily intended for the identification of photons and electrons and for measurements of the energy of the electromagnetic particles [28]. Both the TOF and the EMCal use time-of-flight based particle identification and thus rely on the BBC to provide the start time for flight-time measurements.

The Ring Imaging Čerenkov detector The RICH is used to discriminate between electrons and pions at momenta below the Čerenkov threshold for pions. It is operated with CO_2 , which has a Čerenkov threshold for pions of 4.7 GeV/c.

There is one RICH detector in each arm, just behind PC1. Each detector contains a gas volume of 40 m³ and two mirror panels, which focus the

Čerenkov light as rings onto photomultiplier tubes placed on either side of the entrance window, outside the central arm acceptance. In this analysis the RICH is only used as threshold detector for rejecting electrons.

The Time-of-Flight detector The TOF measures the time of flight of charged particles and is used to identify hadrons in a wide momentum range. It has a limited acceptance since it only covers one sector of 22.5° in ϕ . It also partially covers a sector which is situated beneath the first one but since this part complicates the acceptance it is not being used in this analysis. The TOF is installed in the east arm between the PC3 and the PbGl calorimeter, at a radius of 5.1 m.

The TOF detector consists of 960 slats of plastic scintillators, read out by photomultiplier tubes at both ends. With a combined timing resolution of the start time from the BBC and the stop time from the TOF, a flight-time resolution of 96 ps is achieved, which allows a 4σ separation of kaons and pions up to 2.4 GeV/c and of kaons and protons up to 4.0 GeV/c.

The Electromagnetic Calorimeter The EMCal is the outermost detector in both central arms and it is optimized to measure the position and energy of electrons and photons. Light neutral hadrons, neutral pions and η , are detected in EMCal via their decays into two γ . Heavy flavour mesons like J/Ψ and Υ can be identified via their dilepton decays. The EMCal is also used to measure the energy and extension of jets, as well as the global transverse energy.

Charged hadrons can be identified using time-of-flight measurements but with worse timing resolution in comparison with the TOF detector. However, the resolution is sufficient to allow a 2σ charged hadron separation up to 1 GeV/c for pions and kaons and 2 GeV/c for pions and protons.

The EMCal consists of two subsystems based on different detector materials. The Lead-Scintillator (PbSc) calorimeter covers the entire west arm plus the upper half of the east arm and the Lead-Glass (PbGl) calorimeter covers the lower half of the east arm. While the PbGl has better granularity and energy resolution, PbSc provides better linearity and timing. In this analysis only the PbSc is used since it is more straightforward to use for charged particle identification.

PbSc is a sampling calorimeter consisting of 15552 towers made of alternating layers of lead and plastic scintillators. Each tower is read out individually, via wavelength shifting fibres, by photomultiplier tubes at the back of the tower. PbSc has a good flight-time resolution of ~ 100 ps for electromagnetic showers. For hadronic showers the flight-time resolution

is ~ 270 ps. The difference is mainly due to the larger uncertainty in the start position of the shower and large fluctuations in the signal for hadronic showers.

Chapter 6

Details of the fluctuation analysis

All experiments are limited in such a way that the geometrical acceptance is not 100% and the probability to detect and identify a particle correctly inside this acceptance is not 100%. The latter is referred to as the efficiency, or rather inefficiency. Even in a perfect detector, one would not be able to detect all particles correctly since some, like kaons, may decay before detection. The normal procedure is to determine the average loss of particles due to these effects by detector simulations of the particles traversing sensitive and insensitive parts of the detector. Since the simulation programs describe the detector response very well, these average correction factors can be determined and the measured distributions can be corrected to represent the primordial distributions, even if only a small fraction of the particles have been detected.

In an event-by-event fluctuation analysis, such average corrections can not be applied. The only particles that can be used for the fluctuation study are the ones that have actually been detected. The measured spectra may be quite different from the true spectra produced by the physics processes. An evident example is that this fluctuation study contains few low momentum kaons in comparison with the underlying event sample, since a large fraction of the slow kaons decay before detection.

Clearly the fluctuation analysis is sensitive to two particle correlations. In chapter 3, it was illustrated how the fluctuation signal is altered if the acceptance breaks or retains such particle correlations. In particular, dead areas inside the geometrical acceptance can influence the signal in a way that is hard to predict. Thus, one has to make sure that dead areas are small in comparison with the total acceptance and that only data taken with nearly identical acceptance is included. The data quality assurance

aims at an analysis of data taken under the same conditions with regards to varying acceptance.

Data acquisition is made on a run-by-run basis where each run lasts for approximately an hour. Running conditions can be considered to be constant during such a short time frame. Thus, calibrations are also done on a run-by-run basis. As the raw data from all PHENIX subsystems are assembled in events the output of each run is divided into a number of segments. Any file segment is representative of its respective run and can be used to provide calibration parameters or to perform data quality checks, without having to access the entire data for a run.

This analysis is based on particle identification at mid-rapidity using the PHENIX central arm Time-of-Flight, TOF, and Lead-Scintillator Electromagnetic Calorimeter, EMCal (PbSc). Events of Gold-Gold collisions at an energy of $\sqrt{s_{NN}} = 200$ GeV are selected using a minimum-bias trigger, which requires at least two hits in each Beam-Beam Counter array, BBC north and south. In addition, a hit in each Zero Degree Calorimeter, ZDC north and south, is required in order to reject background from beam-gas interactions. Valid hits have timing properties which are consistent with an emission point in the collision diamond of the two beams. The collision vertex is further constrained in the offline reconstruction. This trigger condition accounts for 93% of the total geometric cross-section of the colliding Gold nuclei.

6.1 Event reconstruction in the central arms

The PHENIX central arm spectrometers are designed to reconstruct momentum of charged particle tracks and identify both hadrons and electrons as well as photons, tasks which require them to be composed of many different detectors. The track reconstruction algorithm relates hits in different detectors in order to determine the trajectories of individual particles, the tracks. The axial magnetic field in the central region bends particle trajectories in the plane orthogonal to the beam axis, which allows for the determination of their transverse momentum. However, the central arm detectors are placed outside the magnetic field region, so here the track model assumption is a straight line. Assuming all tracks to originate from the collision vertex, a primary three dimensional momentum vector is provided by the Drift Chamber together with the z -coordinate from the Pad Chamber layer (PC1) attached to the back of the Drift Chamber. The momentum vector at the Drift Chamber forms a track stub which is projected onto the outer detectors. Hits in these detectors are matched to the track stub projection by calculating the residuals, $\delta r = |\vec{r}' - \vec{r}|$, where \vec{r}' is the

coordinate of the track projection and \bar{r} is the reconstructed coordinate of the hit in the detector [29].

The PHENIX setup is specially designed for detection of photons and electrons, in particular from rare processes. Thus triggering on electrons is essential for operation at highest possible luminosity. In order to minimize the number of electrons coming from γ conversions, the PHENIX detector has minimal material close to the beam axis. One even fills the space inside the Drift Chamber by a helium balloon. The drawback is that the momentum measurement is not supported by intermediate tracking detectors in the field but one has to assume that a track stub observed at the DC position was made by a particle coming from the collision point.

6.2 Momentum reconstruction

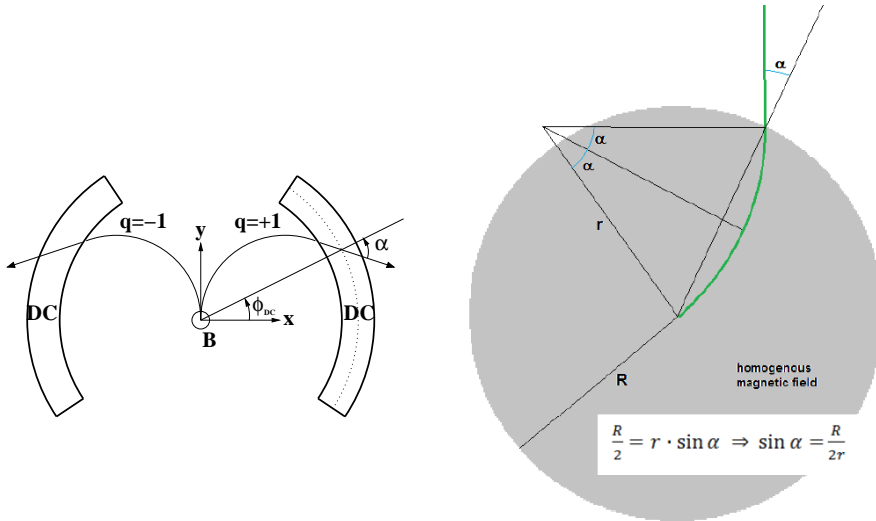
The charge and momentum of a particle can be deduced from the bending of its track in the magnetic field. The force on a charged particle in a magnetic field (eqn. 6.1a) results in an acceleration (eqn. 6.1b).

$$\vec{F} = q\vec{v} \times \vec{B} \quad (6.1a)$$

$$\vec{F} = \frac{\partial \vec{p}}{\partial t} = \gamma m \frac{\partial \vec{v}}{\partial t} \quad \text{since} \quad \frac{\partial \gamma}{\partial t} = 0 \quad (6.1b)$$

With the magnetic field is in the z -direction, the resulting force will be in the transverse plane. For a uniform magnetic field the solution to the above equation system describes a circle with radius $r = p/qB$. Then, as the track exits the magnetic field region, its azimuthal inclination angle, α , with respect to an infinite momentum track originating from the same vertex, as described in figure 6.1a, becomes approximately proportional to the inverse of the transverse momentum, $1/p_T$. It can be shown that $\sin \alpha \propto 1/p_T$, see figure 6.1b, and for small angles $\sin \alpha \approx \alpha$ is a good approximation.

For a non-uniform magnetic field, as in our case, this procedure will not yield exact results. Instead, the azimuthal and polar angles of the track measured at the DC reference radius provide estimates of the momentum, p , and polar angle at the vertex, θ_0 . These are used as input to an iterative procedure where hits associated with the tracks are matched to the track model given by the known field integral, $f(p, \theta_0, r, z)$, using field maps as look-up tables.



(a) Beam view of the inner region.

(b) Relation between azimuthal inclination angle and bending radius of the track [30].

Figure 6.1: Momentum reconstruction in the magnetic field.

6.3 Centrality determination

In this analysis, the data have been divided into 5% wide centrality bins. In PHENIX, the centrality of an event in $\sqrt{s_{NN}} = 200$ GeV Gold-Gold collisions is determined by combining information from the beam-beam counters (BBC), which measure the amount of charged particles produced in the collision at large pseudorapidities, $3.1 < |\eta| < 3.9$, and the zero degree calorimeter (ZDC), which measures fragmentation spectator neutrons. See chapter 5 for a description of the BBC and ZDC detectors. Figure 6.2 shows the BBC charge sum versus the ZDC energy sum for minimum-bias Gold-Gold collisions at a collision energy of $\sqrt{s_{NN}} = 200$ GeV. In central collisions, most of the nucleons in the nuclei participates in the collision and the energy available for particle production is high but few uncharged fragmentation products are released. Thus, the charge deposited in the BBC's is high since it is related to the produced particle multiplicity, while the energy deposit in the ZDC's is low since there are few spectator neutrons. For less central collisions, less energy will be deposited in the overlap region so the charge sum in the BBC's will decrease, since the particle production decreases, but the ZDC's will measure higher values due to an increasing number of fragmentation neutrons from the parts of the nuclei that do not overlap. However, for the most peripheral collisions, the fragmentation spectator products consist mainly of larger charged nuclear fragments. Thus, there will be fewer free neutrons so the signal in the ZDC's will again

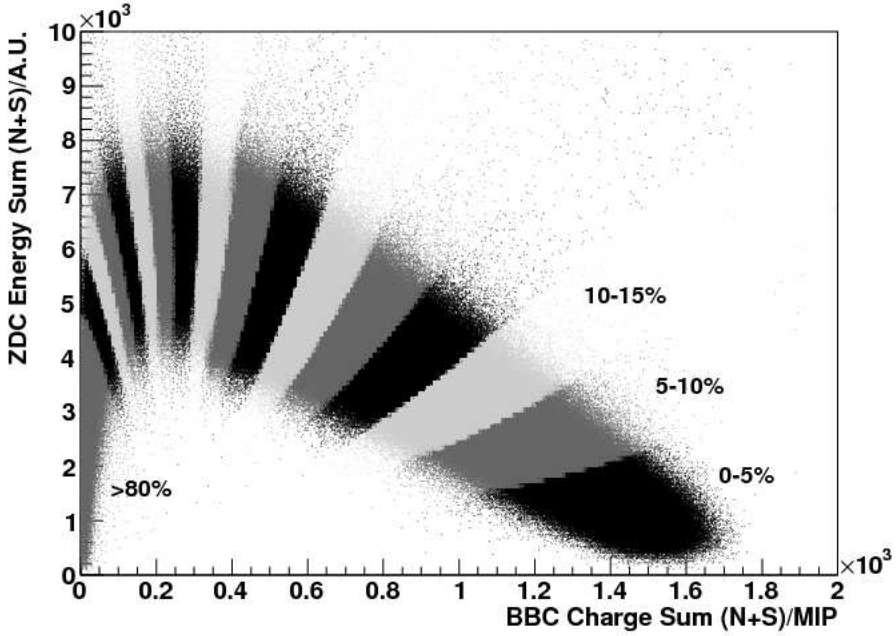


Figure 6.2: BBC Charge Sum vs. ZDC Energy Sum for minimum-bias events divided into 5% wide centrality class slices up to 80% centrality.

decrease. The centrality bins are determined as a selected percentage of the total number of events integrated over the whole histogram, starting from the most central event and assuming a monotonous relation. A description of the centrality definition for the different collisions species and collision energies studied in PHENIX can be found in [31].

For the final results of this analysis, the centrality percentages are converted to number of participants using Glauber Monte Carlo results. In the Glauber Monte Carlo model, independent nucleons of a nucleus are distributed in a three dimensional coordinate system according to a Woods-Saxon density function, which for spherical nuclei is given by equation 6.2. The parameters: the nucleon density in the center of the nucleus, ρ_0 ; the nuclear hard sphere radius, R , and the thickness of the nuclear "skin", a , are obtained from low-energy electron scattering experiments [32]. Figure 6.3 shows the density profile for the Gold ($A=197$) and Copper ($A=63$) nuclei used in the PHENIX experiment.

$$\rho(r) = \frac{\rho_0}{1 + \exp(\frac{r-R}{a})} \quad (6.2)$$

The collision of two nuclei is treated as individual interactions of the constituent nucleons in one nucleus with the ones in the other nucleus. In

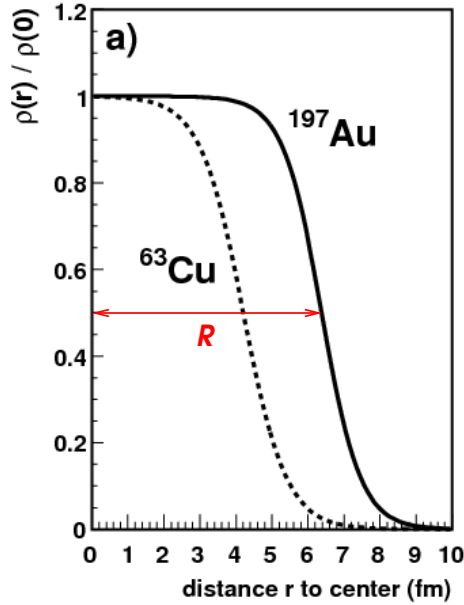


Figure 6.3: Nuclear density profiles of Gold and Copper nuclei used as input to the Glauber Monte Carlo model used in PHENIX [32]

principle, a reaction takes place if the distance between two nucleons in the nucleon-nucleon reaction plane is short enough for them to overlap, with the energy dependent size of the nucleons given by the inelastic nucleon-nucleon cross section, σ_{inel}^{NN} , obtained from measurements of pp collisions. It is assumed that the nucleons move along straight line trajectories independently of each other and irrespectively of its number of collisions with other nucleons according to the frozen straight line approximation.

A sample of nucleus-nucleus collisions is created following the principles outlined above. The advantage of the Monte Carlo approach is that it is straightforward to extract the mean number of participating nucleons, N_{part} , and the mean number of binary nucleon-nucleon collisions, N_{coll} , for any impact parameter interval.

It is also possible to simulate the charged particle multiplicity and other experimentally observable quantities, using an event generating model for particle production like e.g. Hijing [53]. After simulating the detector response of these Monte Carlo events, centrality bins in the resulting particle multiplicity distribution can be mapped to the corresponding bins in the distribution obtained from real data, as indicated in figure 6.2.

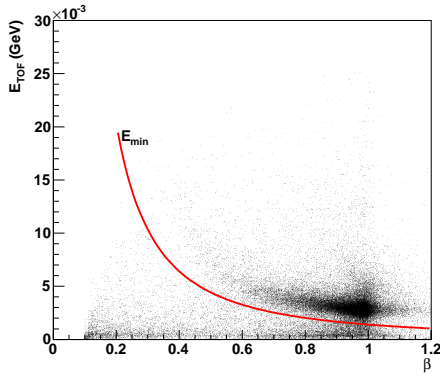
6.4 Event and track selection

Cuts on global and individual track observables are introduced to ensure an accurate data sample. Globally, each event is required to have $|z_{vertex}| \leq 30$ cm and $0 < centrality < 80\%$. The low multiplicities in the more peripheral ($> 80\%$) events result in larger statistical uncertainties than can be compensated by the available data and they do not contribute much information of interest for this study.

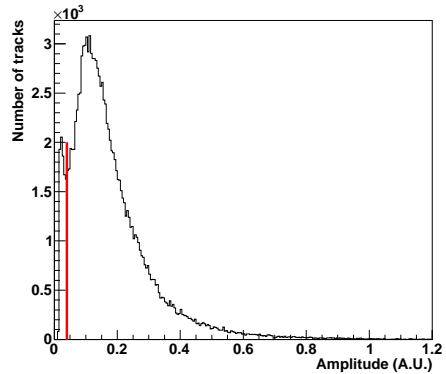
Individual Drift Chamber, DC, tracks are required to have hits in both X-wire sets, X1 and X2, from which the α angle at ϕ is derived. The DC track is required to match a hit in the Pad Chamber, PC1, which gives a z -coordinate that is confirmed by the DC UV stereo wires. The acceptance range at DC/PC1 is limited to $-75 < z < 75$ cm to avoid edge effects. Tracks associated with a Čerenkov ring in the RICH are rejected in order to remove electrons. This also removes other charged particles with momenta above the Čerenkov threshold; muons with $p > 3.5$ GeV, pions with $p > 4.7$ GeV and kaons with $p > \sim 17$ GeV, which is not a problem since these limits are well above the momentum range used for particle identification in this analysis.

Hits in EMCal and TOF are required to be within 2.5σ of the momentum calibrated distribution of track matching residuals. Tracks matched to the EMCal are also required to have a matching hit in the Pad Chamber just in front of it (PC3) within 2.5σ of its distribution of track matching residuals. The TOF does not need this extra matching because of its superior spatial resolution and low sensitivity to photons. It could have been applied for reasons of comparability but the PC3 sector in front of the TOF has a relatively high percentage dead areas and applying such a cut would therefore rather increase the difference in acceptance between the TOF sector and the corresponding EMCal sector.

Additional cuts aimed at improving the track quality include masking out EMCal hits with a hot or dead tower in a three by three tower region around the central tower of the cluster. These towers produce unnaturally high or low signals and the hits are incorrectly reconstructed in their vicinity. There is also a threshold for the energy deposit in the TOF and EMCal in order to reject background. In the TOF a β dependent cut is used with the energy loss parametrized by the Bethe-Bloch formula. The requirement is $E > 0.014 \cdot \beta^{-1.66}$ GeV, figure 6.4a, while a constant threshold cut in the central tower is used for EMCal since there is no visible β dependence of the energy deposit in this case. The threshold is set to the minima in the observed distribution of energy in the EMCal central towers shown in figure 6.4b.



(a) Energy in the TOF.



(b) Amplitude in the EMCal central tower.

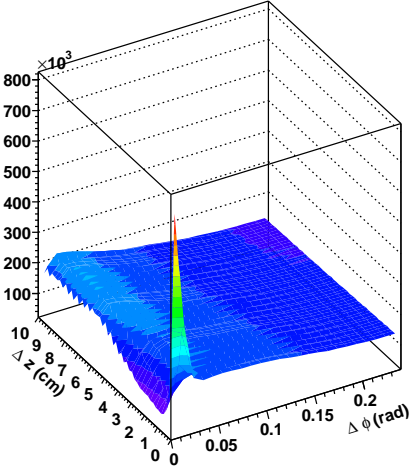
Figure 6.4: Energy deposit in detectors used for particle identification. Solid lines define the applied low energy cut. For EMCal only charged particles with a matching hit in the PC3 are accepted.

6.5 Track proximity cuts

Although the position resolution of the various detectors is high, there will always remain an uncertainty for reconstructed tracks. The data that forms the basis of this analysis was recorded during a time period when there was no operational vertex detector in PHENIX. The vertex z -position was determined by the BBC with a few centimeters resolution. The rather poor resolution of the vertex z -position and the lack of tracking points between the vertex and the Drift Chamber makes the tracking process more difficult and increases the risk of combinatorial mistakes when combining information from inner and outer detectors. Especially when the multiplicity is high tracks can be incorrectly reconstructed. Two possible effects are that two closely situated tracks are merged into one or that one real track is reconstructed as two, creating so called ghost tracks.

Track proximity cuts are used to avoid the problems caused by the limited performance of the tracking for nearby tracks. A first requirement is that no two tracks may be associated with the same EMCal cluster or with hits in the same TOF slat. This is done to make sure that the measurements of timing and energy deposit in the particle identifying detectors are not compromised, since double hits would only give correct time information for the fastest of the two particles. Also the hit position along the slat in TOF and in the EMCal cluster would be incorrectly reconstructed. This cut also removes a large portion of the ghost tracks. In addition, two tracks are rejected if they are separated by less than $\Delta\phi_{DC} = 0.06$ rad and $\Delta z_{PC1} = 1$ cm. These limits are determined from an extensive study of

same sign



opposite sign

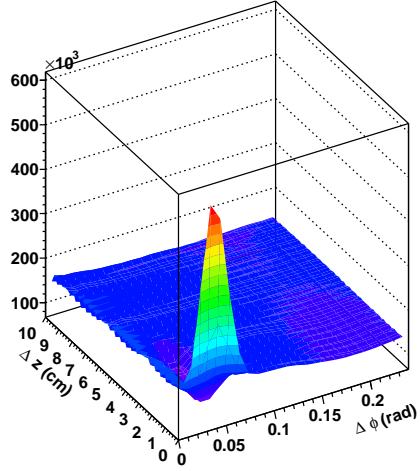


Figure 6.5: Proximity in z_{PC1} vs. ϕ_{DC} for track pairs of same (left) and opposite (right) charge sign.

the topology of the track pair proximity in the DC/PC1 for tracks that pass the other quality cuts outlined above. Figure 6.5 shows the separation in ϕ and z between all pairs of identified particles that are not associated with the same EMCal cluster or TOF slat. For same signed track pairs there is a large peak at small $\Delta\phi$ and Δz . For oppositely signed tracks the peak is displaced and broadened in $\Delta\phi$. Behind the peaks there are valleys of apparently missing tracks extending in Δz . The particle composition in the valley region coincides with the surrounding regions. Therefore these tracks can be kept in the analysis since the assumption can be made that the missing tracks are lost randomly with respect to particle species. The details of the track proximity study can be found in appendix C.

It should be noted that figure 6.5 shows that only an area of about 1×12 cm around a hit is subject to these effects. Since the total detector area used at the DC is about 7m^2 these ghost tracks are indeed a very small fraction of all track pairs. The fact that the ghost tracks have anyway turned out to be of importance for the fluctuation analysis illustrates the extremely high sensitivity of the method.

6.6 Particle identification

Pions, kaons and protons used in this analysis are identified either using the EMCal sectors, which cover an azimuthal angle of $\pi/2$ in the west arm and

	EMCal p_T (GeV/c)		TOF p_T (GeV/c)	
	Min	Max	Min	Max
π	0.4	1.0	0.3	2.2
K	0.4	1.0	0.4	1.8
p	0.6	2.0	0.5	2.2

Table 6.1: Applied cuts in transverse momentum.

$\pi/4$ in the east arm, or in the TOF sector which covers an azimuthal angle of $\pi/8$ in the east arm. The design of the PHENIX experiment is such that the TOF and EMCAL (PbSc) sectors do not overlap. A particle is judged to be of a certain species depending on how much its reconstructed mass, m , deviates from the expected mass of that species. The identification is based on the deviation in m^2 expressed in the unit of standard deviations, σ_{m^2} ,

$$\frac{\delta m^2}{\sigma_{m^2}(p)} = \frac{m^2 - m_X^2}{\sigma_{m^2}(p)} \quad (6.3)$$

where m_X^2 is the expected mass squared of particle species X ($=\pi$, K, p) and m^2 is calculated as

$$m^2 = p^2 \left(\frac{t^2 c^2}{d^2} - 1 \right) \quad (6.4)$$

where p is the particle momentum and d is the distance travelled by the particle along its trajectory, from the collision vertex to the detector where its flight time, t , is measured. Thus, d/t gives the velocity of the particle. The width of the m^2 -distribution, which determines σ_{m^2} , is dependent on momentum, as can be seen from figure 6.6, which shows m^2 of pions, kaons and protons as a function of momentum, divided up in positively and negatively charged particles identified in the TOF and the EMCAL. Also visible is the effect of the better time resolution for hadrons in the TOF, which results in a smaller width in the m^2 -distribution in comparison with the one resulting from EMCAL.

Since the analysis depends on a reliable particle identification, strict cuts in p_T are introduced, as given by table 6.1. The deviation in m^2 must be less than 2σ with a 3σ veto from the neighbouring particle species. With these particle identification, PID, cuts, pions, kaons and protons are well separated in the m^2 - p -plane. Details of the PID is given in appendix B.

6.7 Multiplicities of identified particles

The multiplicity distributions of pions, kaons and protons in central events are shown in figure 6.7. Clearly the identified particle multiplicity is quite

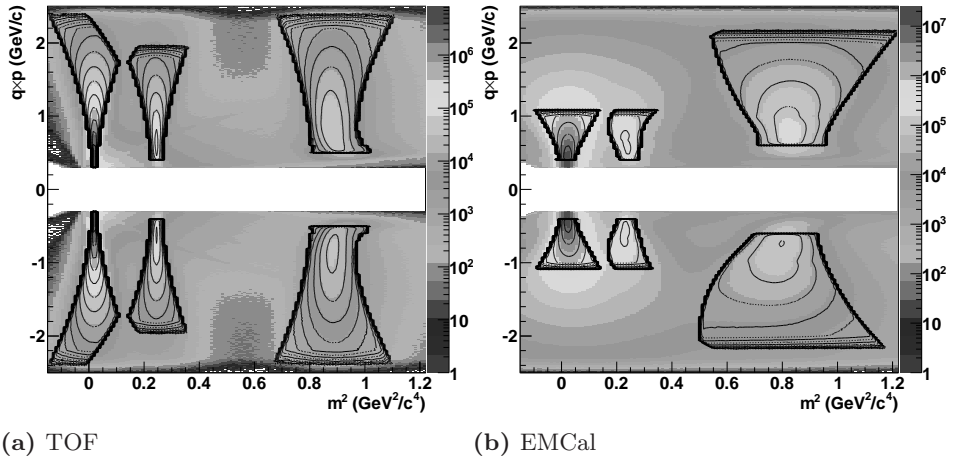


Figure 6.6: Mass squared versus momentum for positively charged ($q = +1$) and negatively charged ($q = -1$) pions, kaons and protons. Limits for particles accepted by the PID cuts used in the analysis are overlaid.

low. Even though the low particle multiplicity is not a problem for the analysis method, it means that a large event sample is needed to obtain results with acceptable statistical significance.

The final raw p_T -spectra of particles identified in the full EMCal acceptance in central (0-15%) collisions are shown in figure 6.8. Note that these spectra are uncorrected, i.e. they represent the p_T distribution of the sample actually used in the fluctuation analysis. As can be seen, the proton spectra is raised above the antiproton spectra due to the net baryon excess. This can be compared with the fully corrected spectra shown in figure 6.9. Only a small fraction of the produced particles can be identified within the requested degree of certainty. The low number of identified kaons is partly due to in-flight decays before they reach the detectors used for identification. The loss of kaons due to this is evidently momentum (velocity) dependent. The large number of cuts used in the particle identification further reduce the observed multiplicities since strict cuts are required at each step, as indicated by the numbers in table 6.2, which shows the effect of the various track cuts on the observed particle multiplicity for central, mid-central and peripheral events with identification in both the TOF and the EMcal. The most important factors are the momentum cut and the loss from the projection of track stubs onto the outer detectors. The momentum range available for particle identification influences the observed multiplicities; due to the steep slope of the p_T -spectra a large fraction of particles are lost if the lower limit is raised.

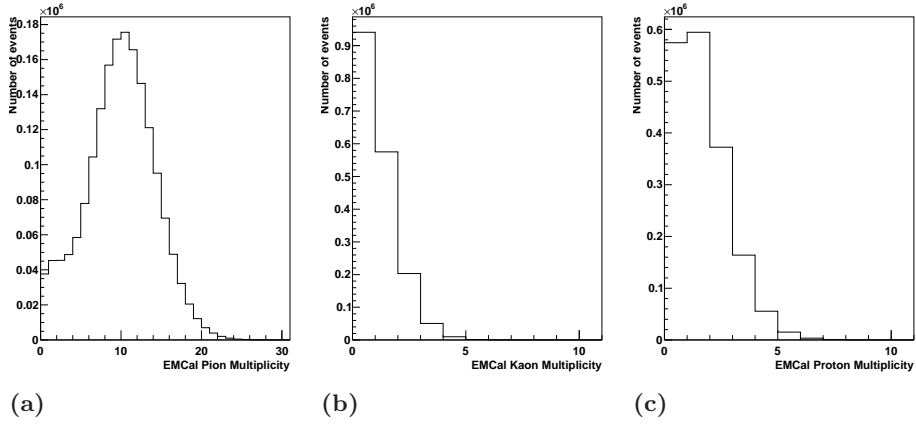


Figure 6.7: Particle multiplicities in the 0-15% most central events identified in the EMCal.

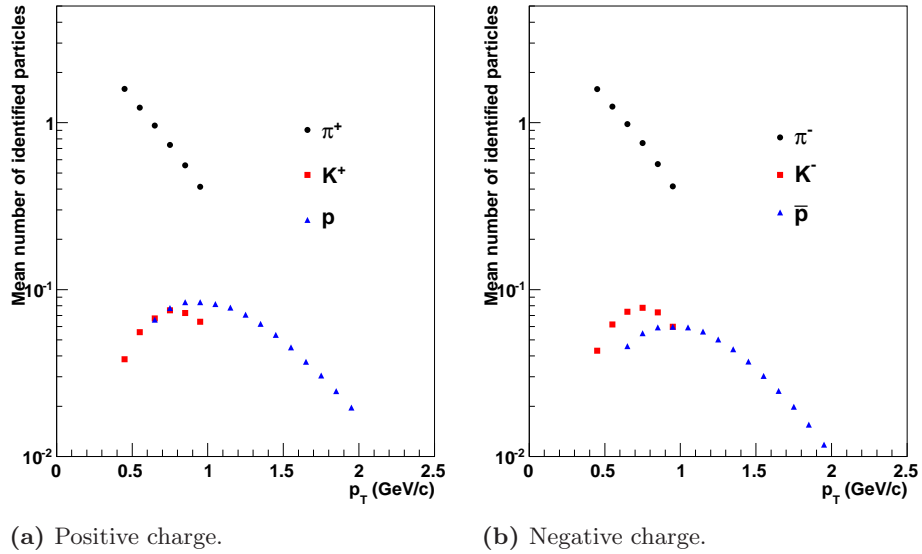


Figure 6.8: Mean pion, kaon and proton multiplicities, in the full EMCal acceptance, as a function of transverse momentum for central Gold-Gold collisions.

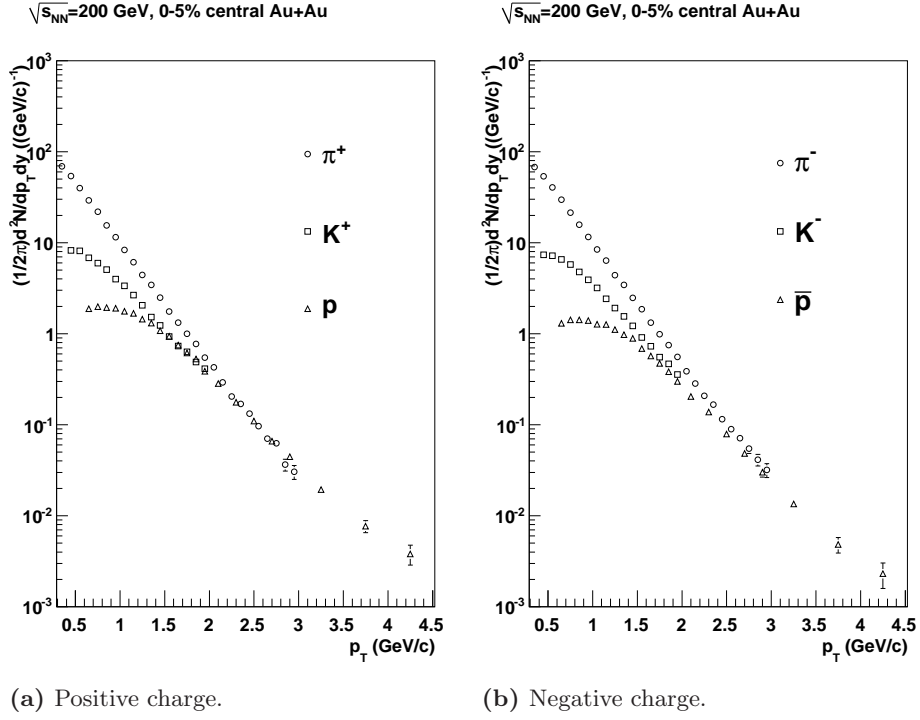


Figure 6.9: Corrected pion, kaon and proton p_T spectra at mid-rapidity, for central Gold-Gold collisions [15].

	central	mid-central	peripheral
All DC track candidates	413.72	132.57	21.05
First p_T -cut: $0.3 < p_T < 2.2$ GeV/c	172.31	55.12	8.13
Good quality track stub	118.21	36.87	4.87
RICH electron rejection	108.70	35.84	4.83
$ z_{PC1} < 75$ cm	102.00	33.63	4.52
<i>EMCal</i>			
PC3 2.5σ Match	37.94	14.96	2.14
Geometrical correction factor %	28.46	11.22	1.60
EMCal 2.5σ Match	25.79	10.32	1.49
Low energy cut	25.38	10.17	1.47
3×3 dead tower cut	23.68	9.48	1.38
3×3 hot tower cut	22.21	8.93	1.30
<i>TOF</i>			
Geometrical correction factor $\frac{1}{8}$	12.75	4.20	0.57
TOF 2.5σ Match	4.63	1.63	0.23
Low energy cut	4.17	1.51	0.21
Identified particles (EMCal+TOF)	18.58	7.53	1.12
Proximity cut	15.96	7.32	1.12
<i>Final average number of pions, kaons and protons</i>			
EMCal π	10.69	4.99	0.79
EMCal K	0.73	0.34	0.05
EMCal p	1.32	0.66	0.09
TOF π	2.67	1.10	0.16
TOF K	0.27	0.11	0.01
TOF p	0.28	0.12	0.02

Table 6.2: Mean number of particles in central (0-5%), mid-central (30-35%) and peripheral (70-75%) collisions after applying various cuts, obtained from a subsample of events. A second p_T cut is included in each PID cut.

6.8 Systematic uncertainties

Due to the construction of the Drift Chamber with longitudinal wires running from the middle ($z=0$) and out, a high-voltage trip in the Drift Chamber extends along at least half and often the full width of the central arm in the z -direction. Therefore it could be located such that it effectively reduces the total azimuthal acceptance differently for negatively or positively charged particles, depending on the direction of the magnetic field. Thus the ratios of positive to negative particle multiplicities will be altered in the events where this type of trip occurs. This effect will be larger for a detector of small acceptance since a tripped high voltage sector constitutes a larger fraction of the acceptance in this case.

In this aspect the TOF is more unreliable than the EMCal, because it has a small azimuthal acceptance and the Drift Chamber in front of it has a high percentage of regions with dead or frequently tripping high voltage channels. Due to these variations in the geometrical acceptance it is difficult to obtain comparable data sets of the EMCal and the TOF.

The inner Pad Chamber layer (PC1) has only about 1% dead area but, as can be seen from the hit patterns in DC/PC1 shown in figures 6.10 and 6.11, there are large dead regions in some parts of the Drift Chamber, which show up as empty bands extended in z (label **a**). Label **b** denotes the sector limits where EMCal/PC3 has a narrow dead band due to mounting. There are also rectangular inactive regions, due to dead or masked out hot towers in the EMCal, but they are probably less significant since they are more localized. In addition there are some dead areas in the outer Pad Chamber layer (PC3), which will further reduce the acceptance since the tracks associated with EMCal hits also require a matching hit in PC3. Small dead areas in the PC3 are not visible in the plot since the curvature of the tracks smears out the effect of the dead area at the DC coordinates.

The effect of imperfections in the acceptance can clearly be seen in figure 6.13 which shows the variation of multiplicities of identified particles, separated in positive and negative charge, over all sectors. Figure 6.14 shows the fractions of kaons, $\langle K/(K + \pi) \rangle$, and protons, $\langle p/(p + \pi) \rangle$, for the same sectors. The sector numbering runs from lower to higher ϕ , as shown in figure 6.12; number 0-5 are EMCal (PbSc) sectors while number 6 is the TOF sector. The ratios in the lowest two EMCal sectors in the west arm, sector 0 and 1, as well as the TOF sector deviate from the overall mean. This could, but will not necessarily, affect the measured ν_{dyn} fluctuations.

Figure 6.15 shows ν_{dyn} as measured in the 0-5% most central events by the different EMCal sectors and the TOF sector. The variation between differ-

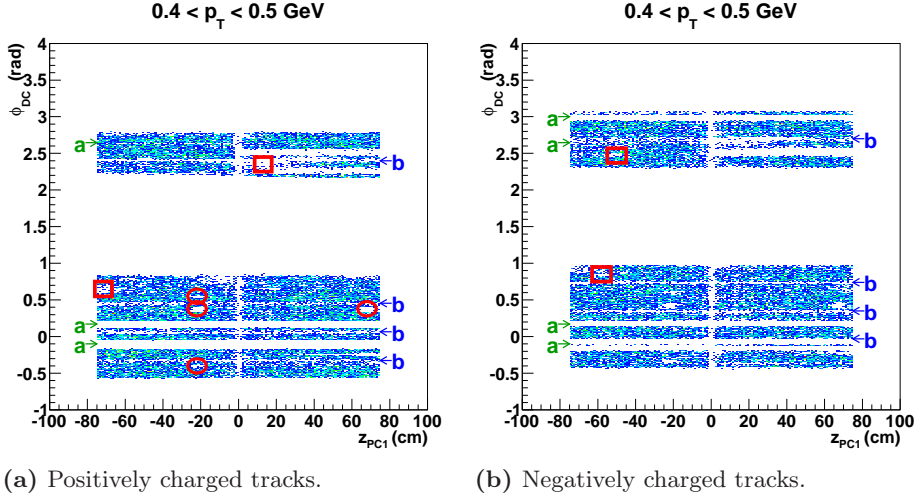


Figure 6.10: Hit pattern in the Drift Chamber (ϕ) and PC1 (z) for particles identified in the east arm (top band) or west arm (bottom band) EMCAL. Arrows labeled **a** point at DC dead areas and arrows labeled **b** point at dead regions in between sectors of the EMCAL/PC3. PC1 dead areas are marked with ellipses and dead areas in the EMCAL or the PC3 are marked with rectangles.

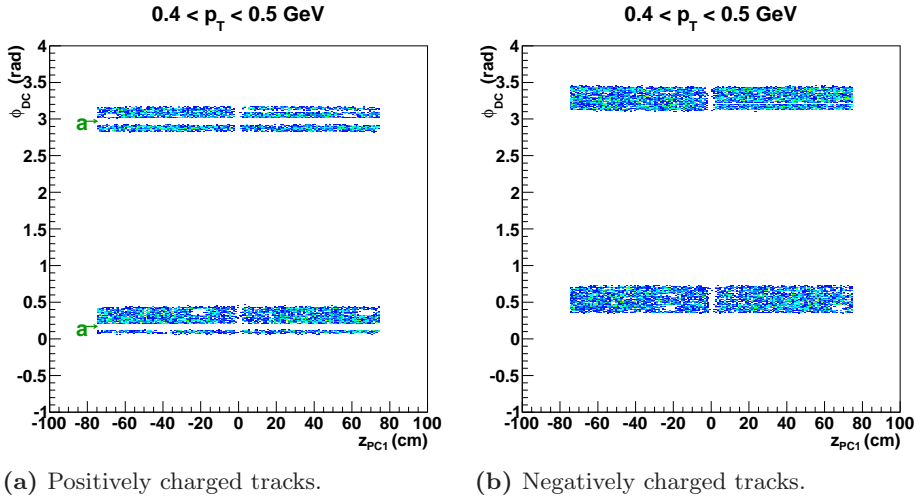


Figure 6.11: Hit pattern in the Drift Chamber(ϕ) and PC1(z) for particles identified in TOF East sector 1 (top band) or EMCAL West sector 2 (bottom band).

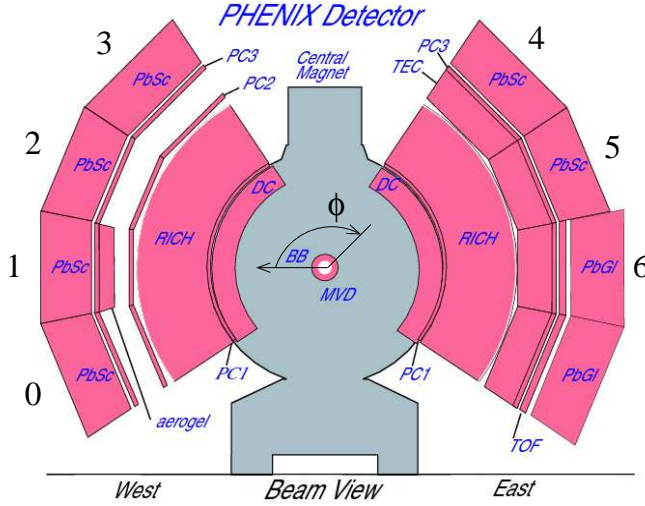


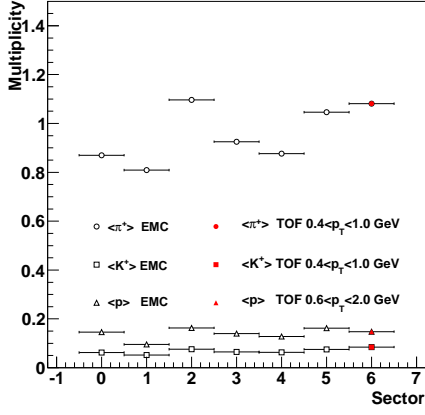
Figure 6.12: EMCal and TOF sector numbering.

ent sectors is quite large, both in between EMCal sectors and in comparison with the TOF sector.

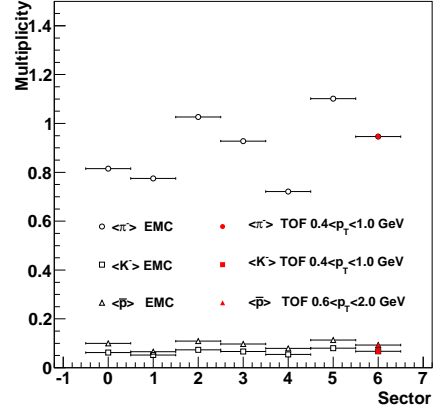
6.8.1 Systematic variation of proximity cuts

In order to test the robustness of the analysis with respect to the selected proximity cuts a series of results were obtained using slightly different cuts, also including additional limits on the proximity in the TOF, the PC3, and the EMCal. Figure 6.16 shows the variation of ν_{dyn} with different proximity cuts for all sectors of EMCal and for the TOF sector.

As discussed above, fluctuation signals tend to be inflated when studied in a smaller acceptance. When the full EMCal aperture is used the differences in ν_{dyn} for varying proximity cuts becomes smaller. Figure 6.17 shows the centrality dependence of ν_{dyn} for three different cases. In the first case no proximity cut is applied. In the second case a strict cut in $\Delta\phi$ - Δz is used which removes the full double peak plus the valley region behind the peaks, corresponding to a region of $\sim 16 \times 8$ cm at the DC reference radius. The third case corresponds to the moderate cut in $\Delta\phi$ - Δz used in the analysis which removes the double peak but not the valley region. The result for the strict cut has slightly larger statistical uncertainty since it is obtained using a smaller event sample but within errors there is no difference between the second and third case.

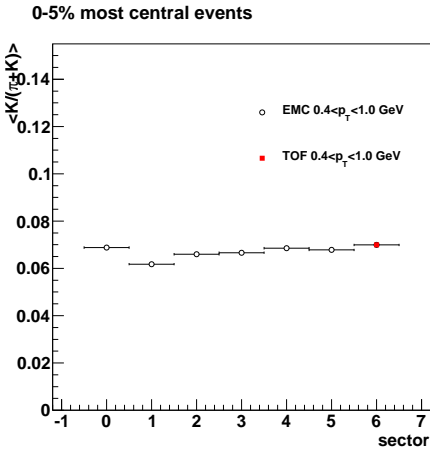


(a) Positive charge.

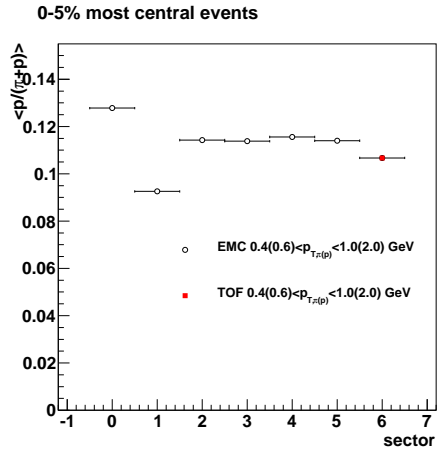


(b) Negative charge.

Figure 6.13: Pion, kaon and proton multiplicity per sector in central 0-5% collisions. Statistical errors are included but vanishingly small.

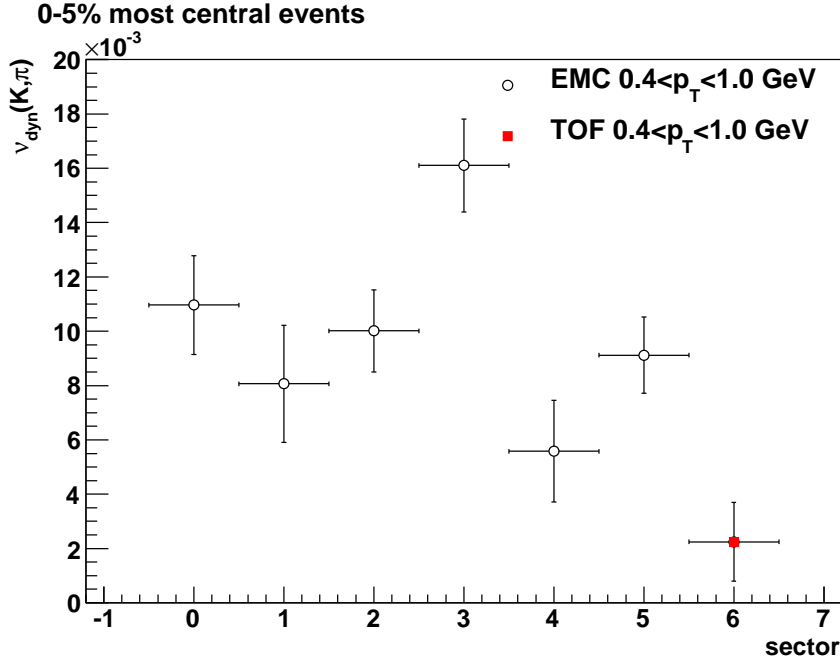


(a) Kaon percentage.

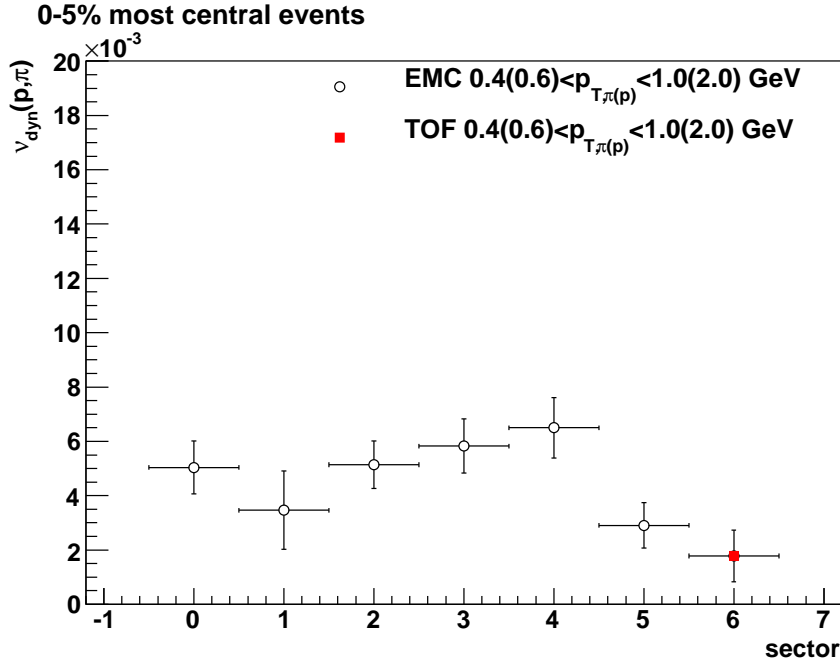


(b) Proton percentage.

Figure 6.14: Kaon and proton fractions per sector. Statistical errors are included but vanishingly small.

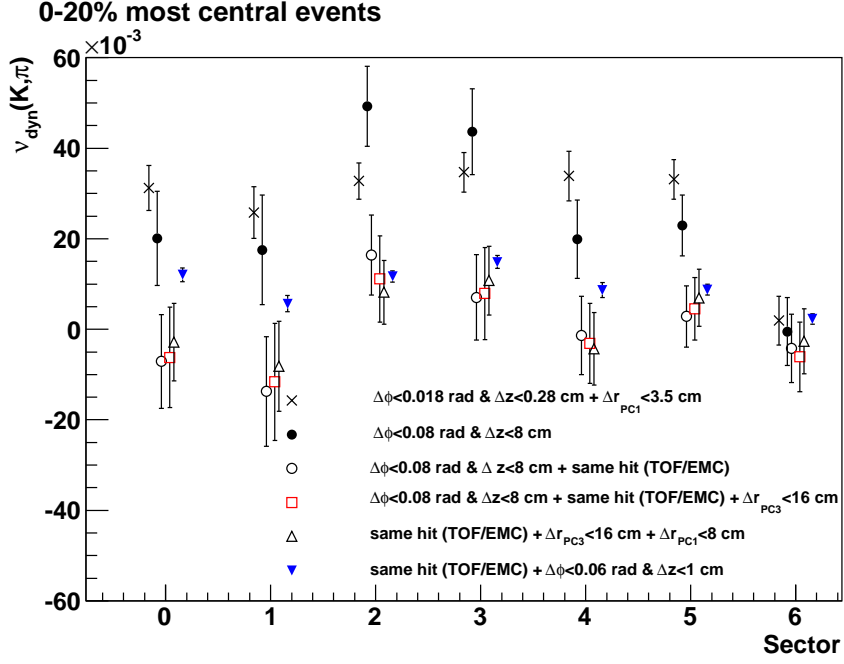


(a) $\nu_{dyn}(K, \pi)$

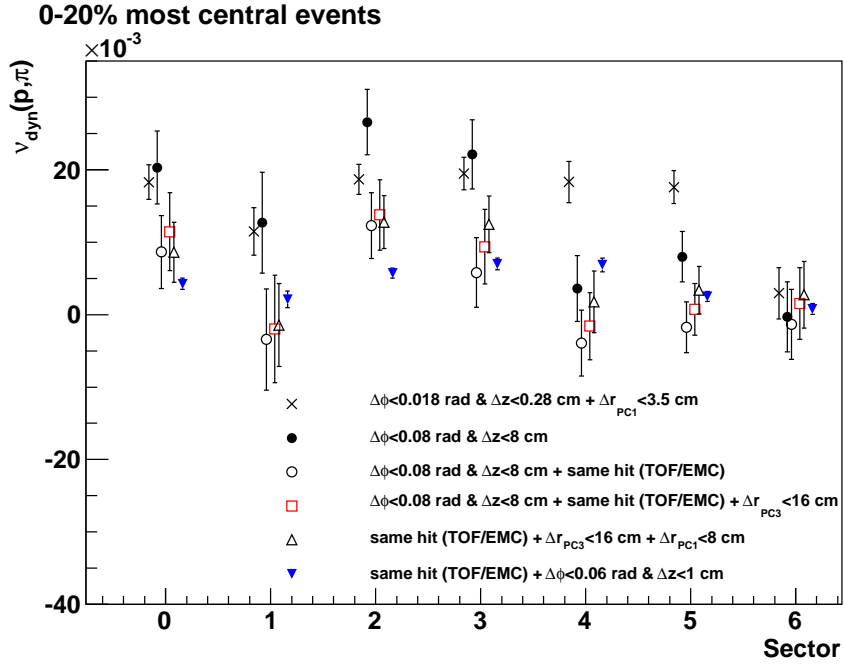


(b) $\nu_{dyn}(p, \pi)$

Figure 6.15: ν_{dyn} per sector.

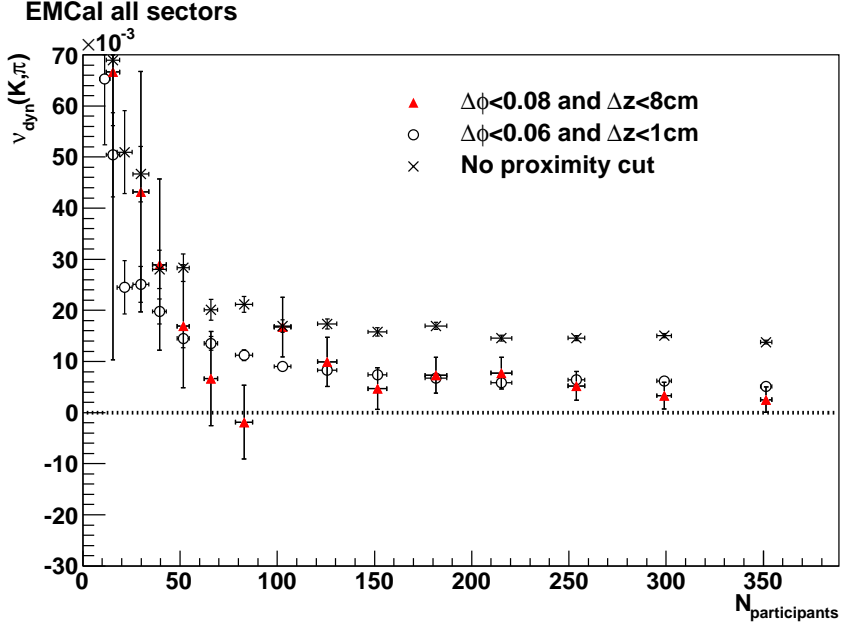


(a) $\nu_{dyn}(K, \pi)$

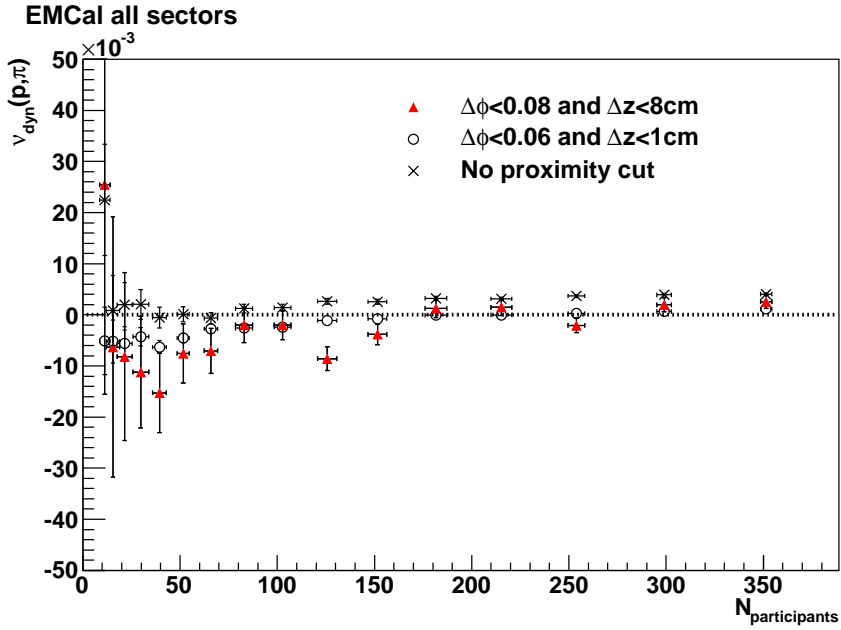


(b) $\nu_{dyn}(p, \pi)$

Figure 6.16: Variation of ν_{dyn} over all sectors for the different excluding proximity cuts listed in the label.



(a) $\nu_{dyn}(K, \pi)$



(b) $\nu_{dyn}(p, \pi)$

Figure 6.17: Variation of ν_{dyn} as a function of centrality for the different excluding proximity cuts listed in the label.

Chapter 7

Quality assurance

Only runs passing certain Quality Assurance, QA, criteria are analysed. This is done to ensure that the data analysis is based on a reliable particle identification under stable conditions. Stable mean values of the number of identified particles per event over the entire range of data is a requirement for obtaining correct results from the ν_{dyn} -method used in this analysis. Changes in the detector performance which leads to variations in the observed multiplicities can modify the results of the analysis and will in the worst case lead to a faulty interpretation of fluctuations. Since the analysis is based on particle identification on an event-by-event basis, one can not apply mean value corrections to the number of identified particles afterwards, as one could in an analysis based on observables extracted from distributions over all events.

Requirements are imposed on the means and widths of runwise distributions of the following parameters, with particles identified in the TOF and the EMCal analysed separately:

- collision centrality
- collision z -vertex
- transverse momentum, p_T , of individual tracks
- time-of-flight of individual tracks
- charged track multiplicity in the 15% most central events
- pion multiplicity in the 15% most central events
- kaon multiplicity in the 15% most central events
- proton multiplicity in the 15% most central events

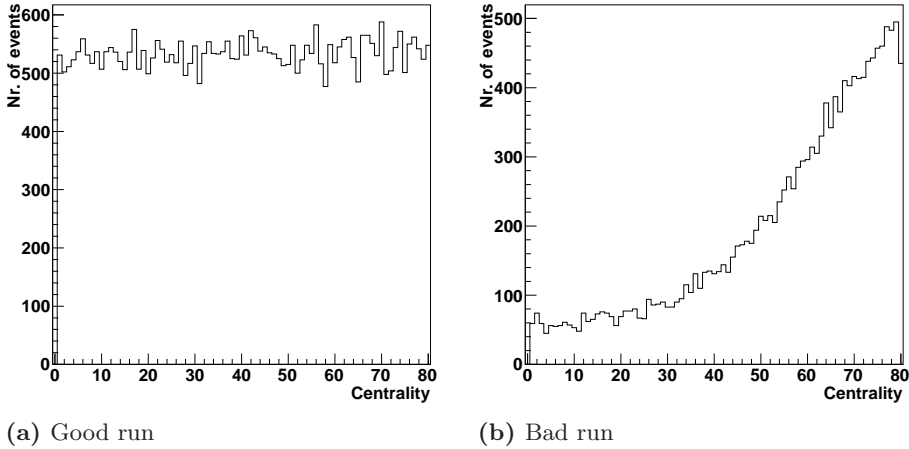


Figure 7.1: Distribution of centrality for two different runs.

Figure 7.1 shows the distribution of event centrality for two different runs. By definition, the distribution should be flat as shown in figure 7.1a, since only minimum-bias events are included in the analysis. If for some reason it is not flat, as shown in figure 7.1b, there is a problem with the centrality determination, which would induce errors in the analysis since fluctuations are studied as a function of centrality. This could for example be the case if the detector settings, like trigger scaledowns, were changed or if the wrong centrality calibration is applied.

Figure 7.2 shows the distribution of charged tracks within EMCal acceptance in 0-15% central events for one representative run and for one run that should be rejected because the multiplicities are too low. The number of charged tracks are counted for each event in the given centrality range. The acceptance for detecting particles is sometimes reduced because parts of the detector is deactivated by high voltage trips or electronics failures. This results in a decrease in the measured multiplicities. If there are any high voltage trips in the detector, these are normally recovered in between runs in order to start every new run with maximum detector coverage. Other problems with the electronics can generally not be solved until the accelerator is shut down at the end of the run period. Thus, the acceptance varies slightly from run to run and over the run period. Another factor that influences the measurements is the tuning of the detector settings, which usually becomes more stable towards the end of the run period.

The mean values of the distributions of all the above mentioned parameters are extracted for selections of data segments belonging to the same run, as well as the standard deviations of these distributions. Next, means and

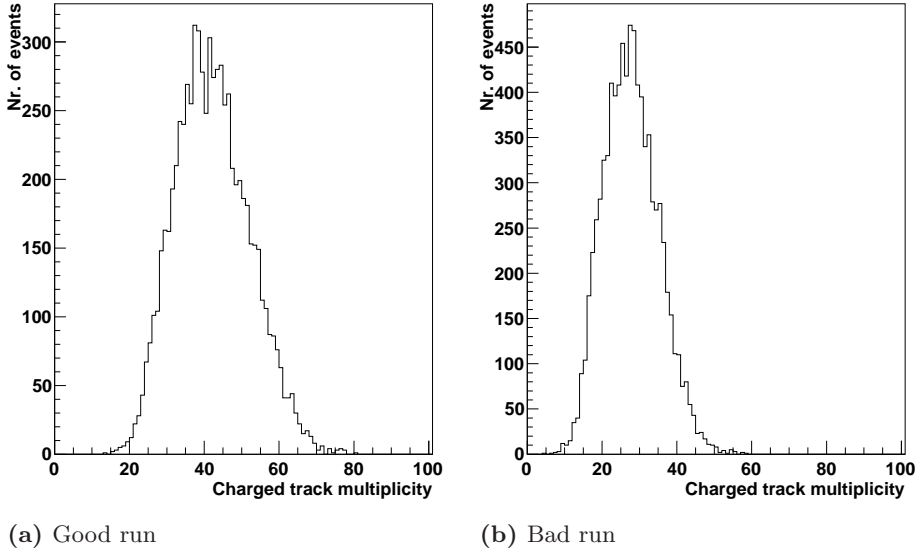
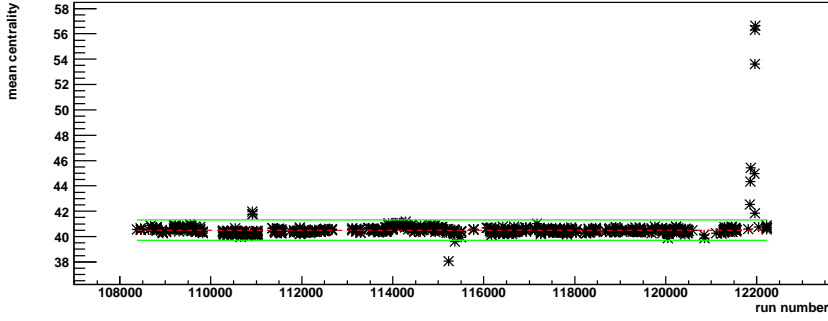
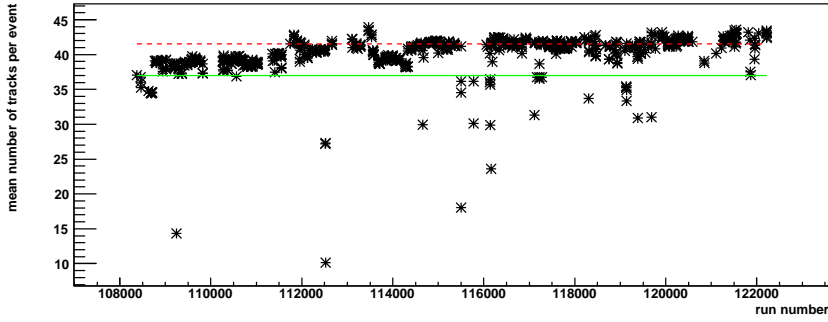


Figure 7.2: Distribution of the number of charged tracks in the 15 % most central events for two different runs.

standard deviations for all the runs are plotted against the run number, like in figure 7.3a, which shows the result for the run-by-run mean event centrality, and figure 7.3b showing the run-by-run mean number of charged tracks per event. One can see that the measurements become more stable as the run period proceeds but also that the detector failures occurs more frequently. Runs that deviate from the overall average behaviour can be identified from these plots. A cross-check is made between the different parameters before a run is excluded from the following analysis.



(a) Mean event centrality



(b) Mean multiplicity in EMCAL

Figure 7.3: Mean values of distributions of multiplicity and centrality as a function of run number. Runs with values below the lower boundary or above the upper, if present, boundary (solid lines) are marked as bad.

Chapter 8

Analysis of Gold-Gold collisions at $\sqrt{s_{NN}} = 200$ GeV

There are two main particle identification capabilities in the PHENIX run 4 central arm detector configuration: the east arm Time-of-Flight, TOF, with one usable sector, and the Lead Scintillator Electromagnetic Calorimeter, EMCal, which covers the full four sectors of the west arm plus the two upper sectors in the east arm. Both were exploited in this analysis in order to take advantage of the large azimuthal acceptance of the EMCal along with the superior resolution of the TOF, which allows identification of particles at higher momenta than in the electromagnetic calorimeter. The detectors are described in more detail in chapter 5.

An advantage of this approach is that when the same analysis is performed using two independent particle identifying detectors the results can be compared and checked for consistency. However, the analysis is sensitive to variations in the geometrical acceptance, i.e. dead areas. Analysis can be done on any azimuthal acceptance as long as there is no azimuthal correlation within particle pairs. If there are correlations the acceptance must enclose these. The effect on the signal of such holes in the geometrical acceptance is not obvious, it depends on what type of signal there is and to what extent particles are lost randomly or not. If there is such an effect, it is sensible to assume that it would be more problematic for a detector with small total acceptance, because *a*) a larger fraction of the particle pairs are affected and *b*) it becomes more probable that particles are excluded in a systematical fashion.

As has been seen in section 6.8 the data in the TOF sector is strongly affected by the dead area in the DC in front of it. Likewise other dead DC areas makes it preferable to do the analysis in the full EMCal acceptance. The analysis method using ν_{dyn} , as defined by equation 3.4, was described

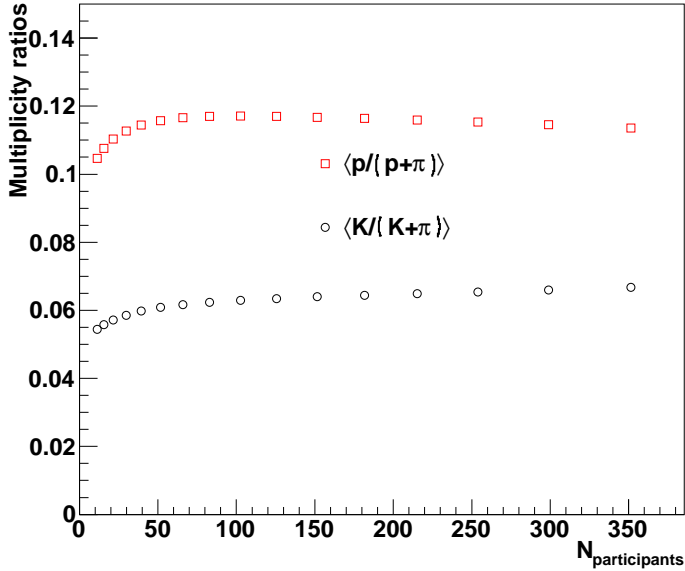


Figure 8.1: Average particle ratios in the analysed sample as a function of centrality for the full EMCal acceptance. Statistical errors are included but vanishingly small.

in chapter 3.

8.1 Centrality dependence of ν_{dyn}

Fluctuations are analysed as a function of collision centrality represented by the number of participating nucleons in the collision, $N_{\text{participants}}$. Figure 8.1 shows the kaon and proton fractions, for the full range of centrality bins used in the analysis, in the kaon plus pion and proton plus pion sample, respectively. Both ratios are reasonably stable with a dip for the most peripheral events. Figure 8.2 shows the corresponding uncorrected multiplicities of the different particle species, with the total multiplicity of identified particles ranging from ~ 13 in central events to ~ 1 in peripheral events.

The centrality dependence of $\nu_{dyn}(K, \pi)$ and $\nu_{dyn}(p, \pi)$ as measured in the full EMCal acceptance can be seen in figure 8.3. A significant difference between (K, π) and (p, π) is observed, where the former increases with decreasing centrality, approximately following $1/N_{\text{participants}}$, while the latter appears flat with values very close to zero.

A comparison with events from a Hijing Monte Carlo simulation is shown

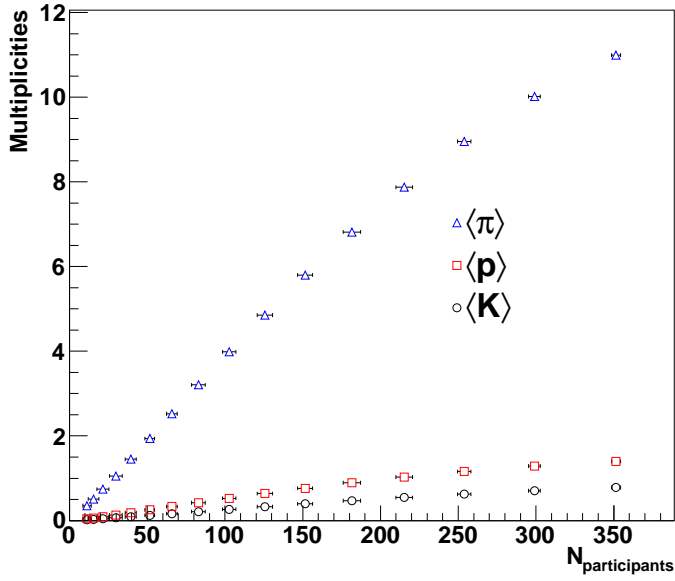


Figure 8.2: Average particle multiplicities in the analysed sample as a function of centrality for the full EMCal acceptance. Statistical errors are included but vanishingly small.

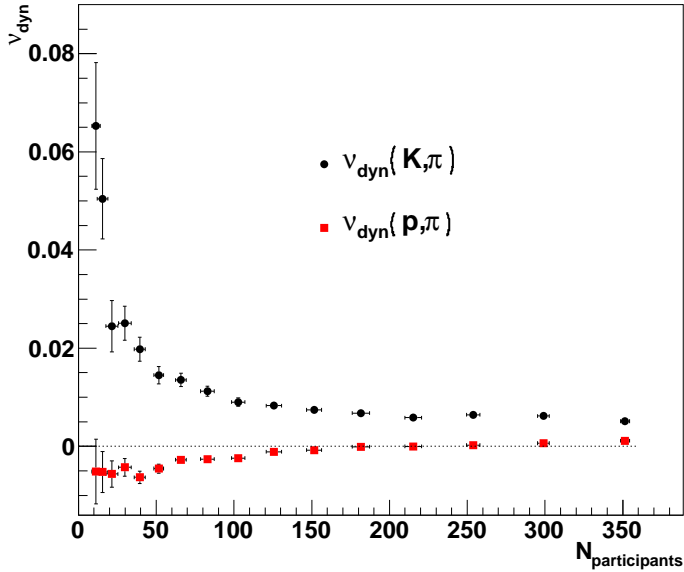


Figure 8.3: Centrality dependence of ν_{dyn} for the full EMCal acceptance. The error bars denote statistical uncertainties.

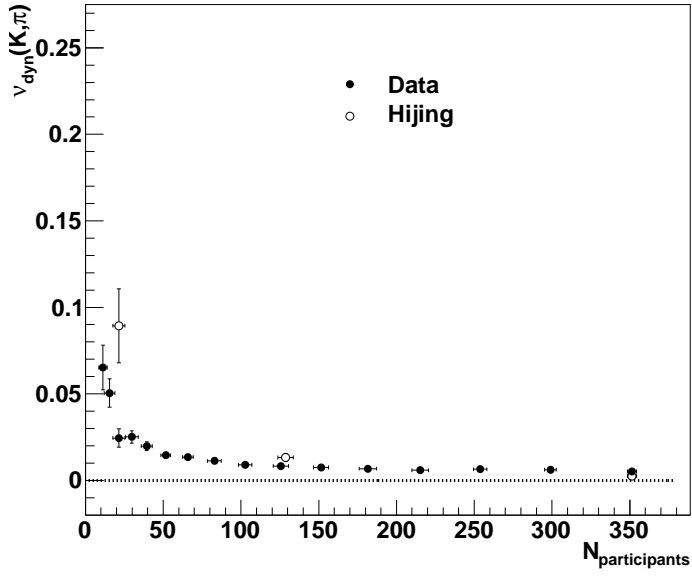
in figure 8.4. There is a good agreement between the analysed data and Hijing events for $\nu_{dyn}(K, \pi)$. In contrast, $\nu_{dyn}(p, \pi)$ obtained from Hijing events displays a completely different centrality dependence than what is observed in data. It should be noted that the Hijing simulation is done with the same geometrical acceptance as the EMCal detector and for the same momentum range as was used in the data analysis but the Hijing events are not filtered through the simulated PHENIX detector. Thus, no other detector effects like detection efficiencies, imperfections in the acceptance or tracking mistakes are included. The fact that Hijing gives such a reasonable description of $\nu_{dyn}(K, \pi)$ indicates that the detector effects which may influence $\nu_{dyn}(K, \pi)$ are random in nature when the full EMCal acceptance is used. There is evidently little room for non statistical fluctuations in K/π apart from those accounted for in Hijing.

The individual terms of ν_{dyn} are included in figures 8.5 and 8.6 for completeness. They show the centrality dependence for the three terms of $\nu_{dyn}(K, \pi)$ and $\nu_{dyn}(p, \pi)$, respectively. All three terms are very similar in behaviour and only the small differences result in a non-zero value of ν_{dyn} .

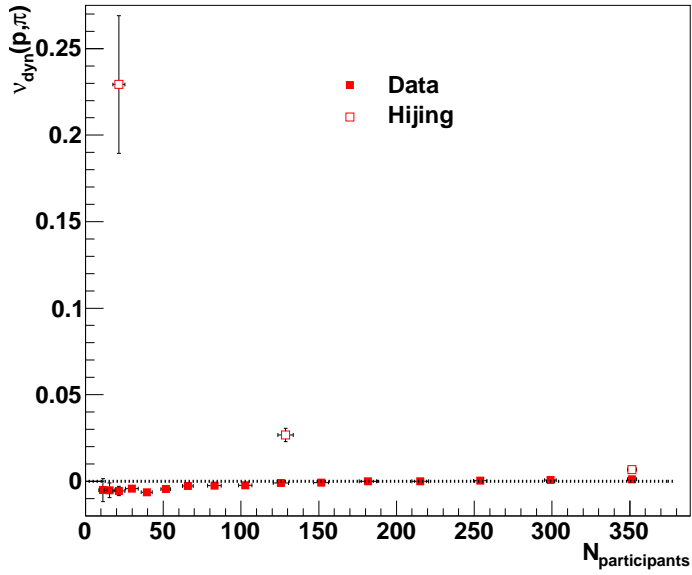
8.2 Dependence on momentum and azimuthal acceptance

The momentum dependence of ν_{dyn} was studied by grouping the particles in 100 MeV/c wide bins of transverse momentum and calculate ν_{dyn} separately for each bin. Thus, only a small fraction of all pairs will be included: pairs consisting of particles that fall into the same p_T -bin. The result is shown in figure 8.7. As can be seen both $\nu_{dyn}(K, \pi)$ and $\nu_{dyn}(p, \pi)$ increase with increasing p_T . A weaker but similar trend is seen in the Hijing simulation, cf. figure 4.5. This is expected if pair correlations are strongest for particles with similar transverse momenta. For a limited p_T -bin many correlated pairs will survive, when at the same time the number of combinatoric pairs decreases. This effect will increase ν_{dyn} with increasing p_T , due to the falling slope of the p_T -distribution.

The azimuthal acceptance affects the observed fluctuations as can be seen in figure 8.8, where $\nu_{dyn}(K, \pi)$ and $\nu_{dyn}(p, \pi)$ for the full EMCal acceptance is compared with the result for one EMCal sector, obtained as the mean over all sectors. There is an increase of ν_{dyn} with decreased azimuthal acceptance. The dependence on azimuthal acceptance is not as strong as $1/\Delta\phi$ expected if particles in a pair are fully aligned, cf. figure 3.6, but still indicates an angular correlation between particles from correlated production.



(a) $\nu_{dyn}(K, \pi)$



(b) $\nu_{dyn}(p, \pi)$

Figure 8.4: Comparison of the centrality dependence of ν_{dyn} in data with corresponding results from Hijing.

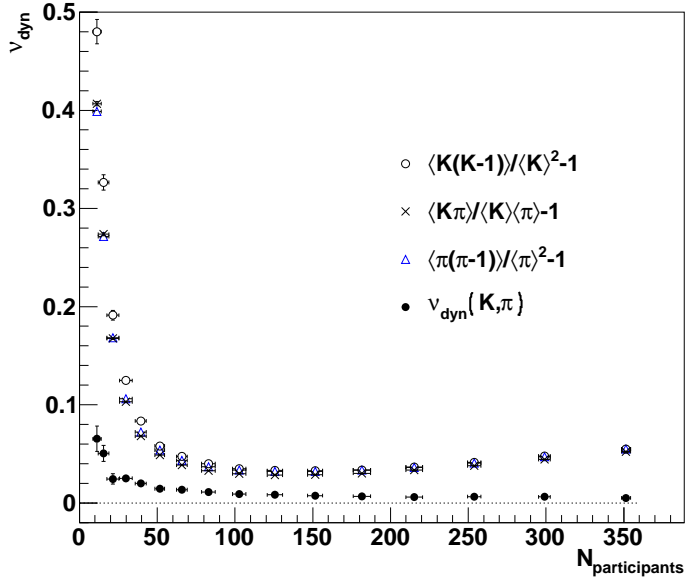


Figure 8.5: Centrality dependence of $\nu_{\text{dyn}}(K, \pi)$ constituent terms for the full EMCal acceptance.

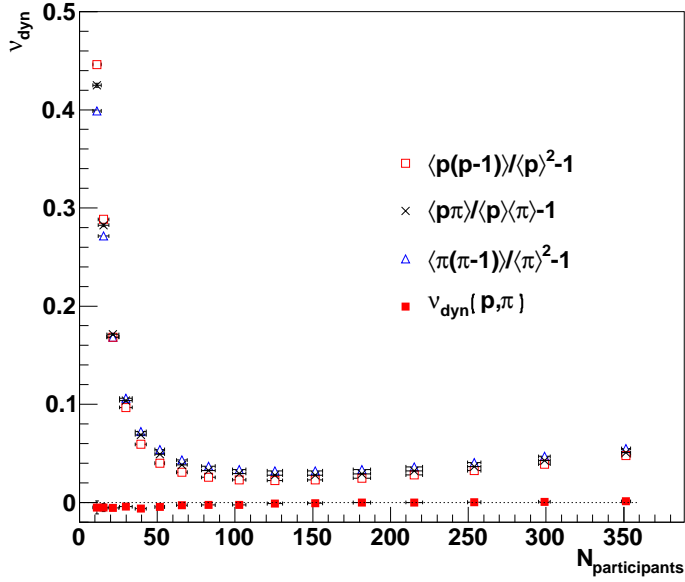


Figure 8.6: Centrality dependence of $\nu_{\text{dyn}}(p, \pi)$ constituent terms for the full EMCal acceptance.

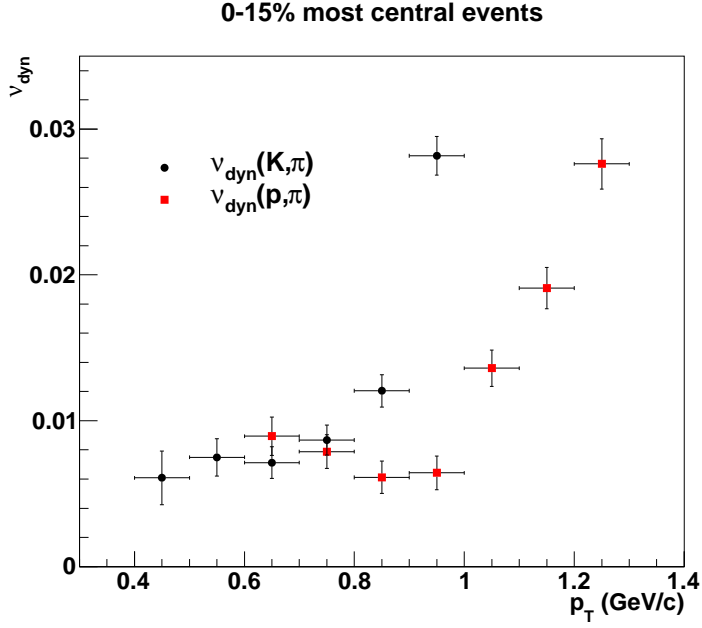


Figure 8.7: ν_{dyn} as a function of transverse momentum.

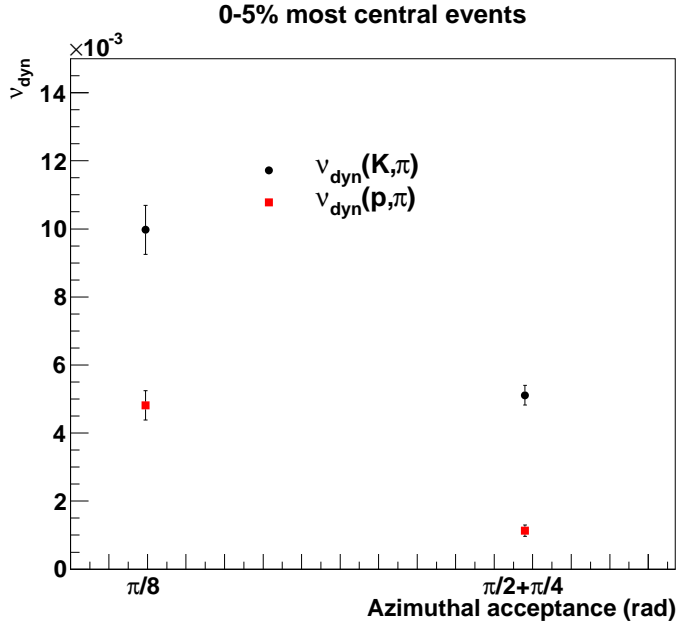


Figure 8.8: ν_{dyn} as a function of azimuthal acceptance. $\pi/8$ corresponds to one EMCAL sector and $\pi/2 + \pi/4$ corresponds to the full EMCAL acceptance.

8.3 Charge combinations

The inclusive ν_{dyn} measure can be resolved in its charged components, which have been studied in order to better understand the results. Figures 8.9 and 8.10 show all four charge combinations of $\nu_{dyn}(K, \pi)$ and $\nu_{dyn}(p, \pi)$, respectively. In the $K\pi$ -case the centrality dependence is very similar for all charge combinations but quite unlike the inclusive $\nu_{dyn}(K, \pi)$ shown in figure 8.3. Since decays will contribute more to the unlike sign combinations, the similar behaviour observed between like and unlike sign combinations indicate that the influence of particle decays on these results is small. Only for the most peripheral events with $N_{part} < 100$ there are signs of a separation between like and unlike sign combinations, with a dip in $\nu_{dyn}(K^+, \pi^-)$ and $\nu_{dyn}(K^-, \pi^+)$. The like sign combinations for peripheral events are consistent with the general trend of $\nu_{dyn}(K, \pi)$ for all charge combinations in mid-central and central events, which can be described as slightly positive and constant as a function of centrality. The positive values of $\nu_{dyn}(K, \pi)$ implies that kaons (and pions) are more likely to be produced in KK (or $\pi\pi$) pairs than they should be statistically.

Also in the $p\pi$ -case (figure 8.10) the behaviour for like and unlike sign combinations are similar. As in the $K\pi$ -case the centrality dependence is quite different from the corresponding inclusive case. The small separation between the proton and antiproton results can be attributed to the net-proton excess. The general behaviour of $\nu_{dyn}(p, \pi)$ charge combinations is well described by the $1/N_{participants}$ dependence discussed in section 3.1. The negative values of $\nu_{dyn}(p, \pi)$ in all but the most central events imply that protons and pions are more likely to be produced in $p\pi$ pairs than they should be statistically.

Contributing to the inclusive ν_{dyn} measure are also the particle-antiparticle correlations of pions, kaons and protons with different charges. Figure 8.11 shows the different centrality dependencies of $\nu_{dyn}(\pi^+, \pi^-)$, $\nu_{dyn}(K^+, K^-)$ and $\nu_{dyn}(p, \bar{p})$. These particle-antiparticle correlations are predominately negative indicating that unlike sign particles of the same species are produced in pairs, thereby reducing the fluctuations in the \pm -ratio. These correlations are included in the inclusive ν_{dyn} -distributions but not in the charge separated ones, as shall be shown in the next section using the sum rules discussed in Paper I.

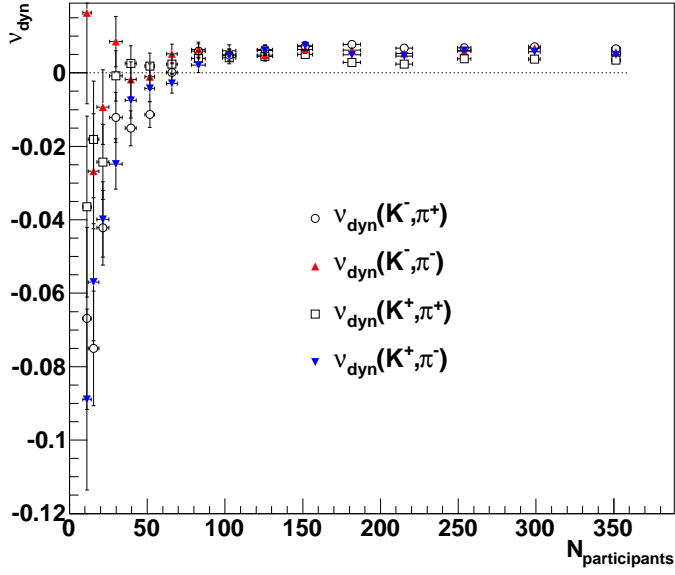


Figure 8.9: Centrality dependence of correlations between different charge combinations of pions and kaons for the full EMCal acceptance.

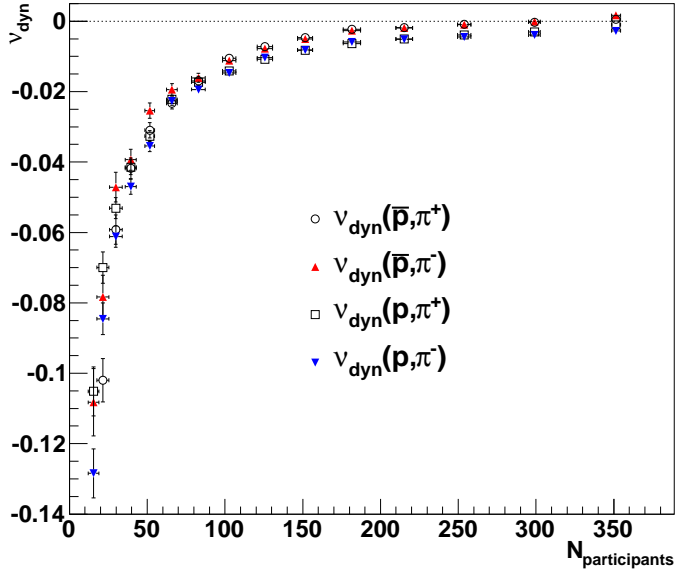


Figure 8.10: Centrality dependence of correlations between different charge combinations of pions and protons for the full EMCal acceptance.

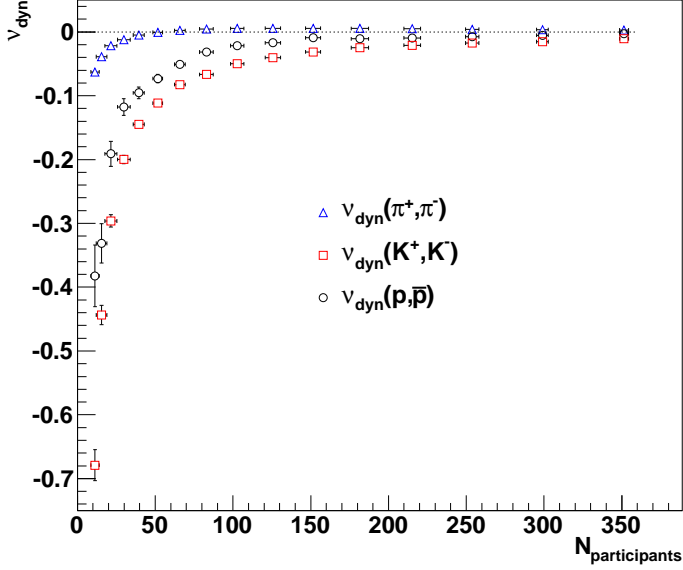


Figure 8.11: Centrality dependence of particle-antiparticle correlations between positively and negatively charged pions, kaons and protons for the full EMCal acceptance.

8.4 Application of sum rules

If there are equal numbers of particles and antiparticles, which is a good approximation, at least for pions and kaons cf. figure 6.13, the sum rules given in the paper on number-ratio fluctuations, included at the end of this theses, can be simplified, resulting in the following formula:

$$\begin{aligned} \nu_{dyn}(K^+ + K^-, \pi^+ + \pi^-) &= \frac{1}{4} (\nu_{dyn}(K^+, \pi^+) + \nu_{dyn}(K^+, \pi^-)) \\ &\quad + \frac{1}{4} (\nu_{dyn}(K^-, \pi^+) + \nu_{dyn}(K^-, \pi^-)) \\ &\quad - \frac{1}{4} (\nu_{dyn}(K^+, K^-) + \nu_{dyn}(\pi^+, \pi^-)) \end{aligned} \quad (8.1)$$

$$\begin{aligned} \nu_{dyn}(K^+ + K^-, \pi^+) &= \frac{1}{2} (\nu_{dyn}(K^+, \pi^+) + \nu_{dyn}(K^-, \pi^+)) \\ &\quad - \frac{1}{4} (\nu_{dyn}(K^+, K^-)) \end{aligned} \quad (8.2)$$

$$\begin{aligned} \nu_{dyn}(K^+, \pi^+ + \pi^-) &= \frac{1}{2} (\nu_{dyn}(K^+, \pi^+) + \nu_{dyn}(K^+, \pi^-)) \\ &\quad - \frac{1}{4} (\nu_{dyn}(\pi^+, \pi^-)) \end{aligned} \quad (8.3)$$

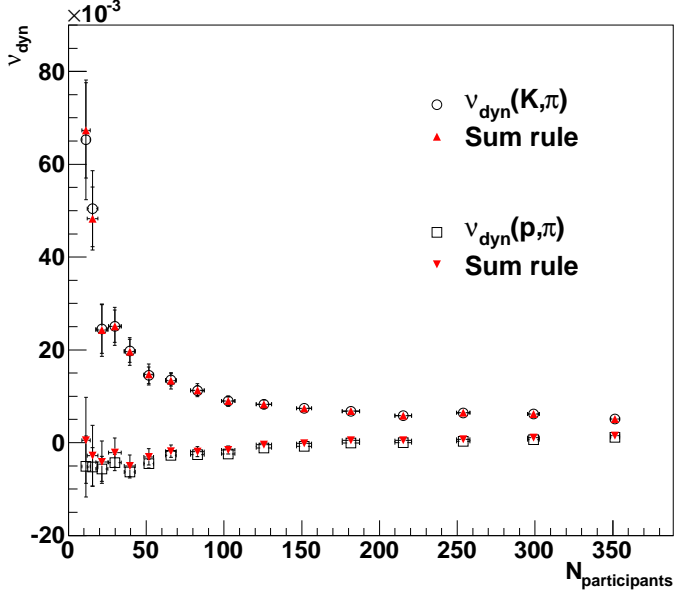


Figure 8.12: Inclusive ν_{dyn} measure compared with the sum rule given by equation 8.1.

There is an excellent agreement of the sum rules with $\nu_{dyn}(K, \pi)$, as shown in figures 8.12 and 8.13. Protons are slightly more numerous than the antiprotons which explains the small discrepancy between the sum rules and $\nu_{dyn}(p, \pi)$ in figures 8.12 and 8.14.

Figure 8.13 shows that $\nu_{dyn}(K^+, \pi^+ + \pi^-)$ is similar to $\nu_{dyn}(K^+, \pi^+)$ and $\nu_{dyn}(K^+, \pi^-)$ whereas $\nu_{dyn}(K^+ + K^-, \pi^+)$ more resembles the inclusive $\nu_{dyn}(K, \pi)$ -distribution, indicating that the method is more sensitive to correlated kaon pairs than to correlated pion pairs. This is expected since the more frequent pions provide a larger combinatorial background. In figure 8.14 the same observation is made in the $p\pi$ -case, again showing that the method is more sensitive to correlations amongst the rarer species.

From this one can conclude that particle decays giving rise to two oppositely charged kaons give a large contribution to the fluctuations observed in the inclusive $\nu_{dyn}(K, \pi)$ -distribution, whereas decays to different particle species only affect the fluctuations marginally. For the inclusive $\nu_{dyn}(p, \pi)$ -case the correlations from $p\bar{p}$ pairs effectively cancel out the fluctuations observed when charge combinations are studied. In order to better understand the mechanisms responsible for fluctuations it is thus of vital importance to study fluctuations for different charge combinations.

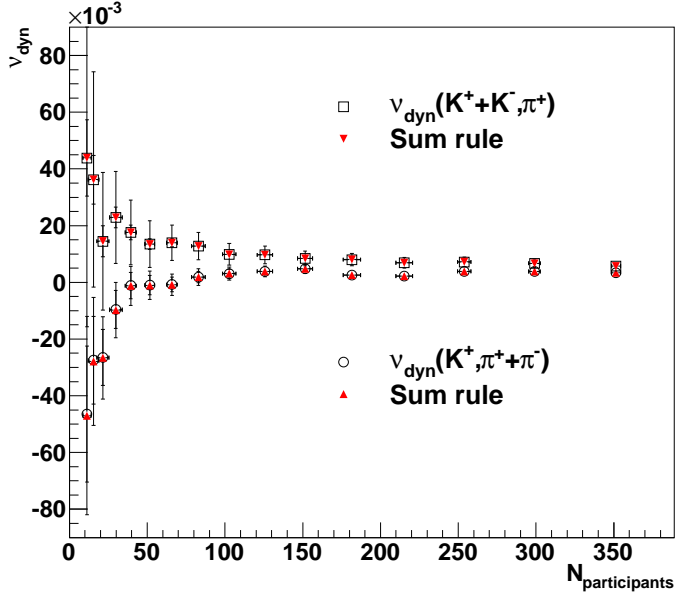


Figure 8.13: Semi-inclusive ν_{dyn} measures for $K\pi$ compared with the sum rule given by equations 8.3 and 8.2.

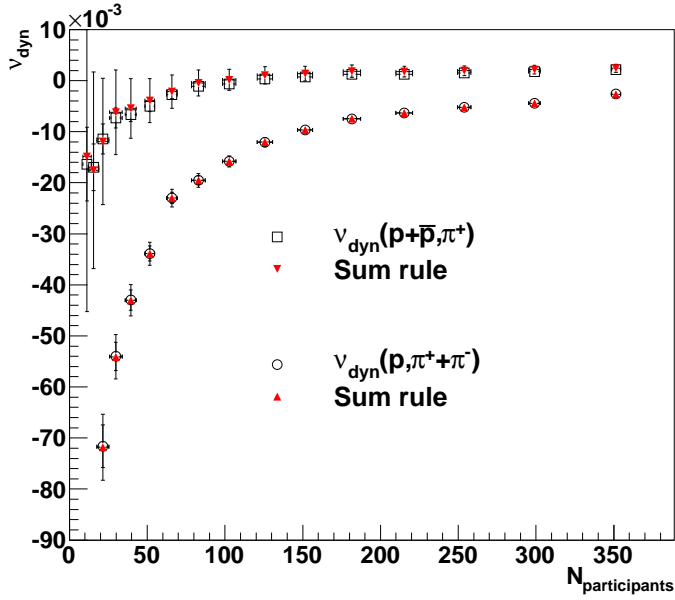


Figure 8.14: Semi-inclusive ν_{dyn} measures for $p\pi$ compared with the sum rule given by equations 8.3 and 8.2.

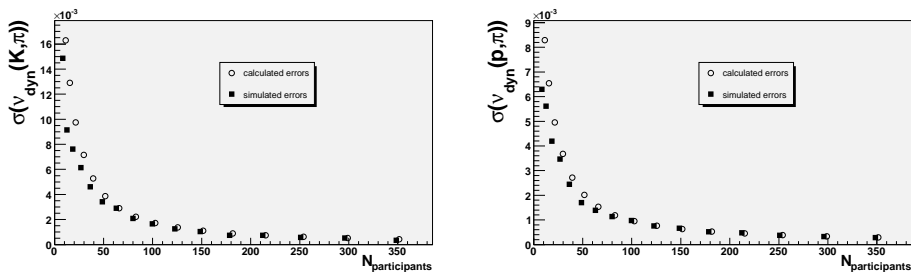


Figure 8.15: Comparison of statistical errors for ν_{dyn} . The calculated errors and the errors extracted from simulation are in very good agreement for both $\nu_{dyn}(K, \pi)$ (left) and $\nu_{dyn}(p, \pi)$ (right).

8.5 Error calculation

Statistical errors in ν_{dyn} are calculated according to an analytical approximation, see appendix D, taking into account all fluctuations. However, the approximation requires a sufficiently large number of events to be reliable. For comparison, errors are also extracted from a simulation where 100 sets of events are generated for each centrality bin. ν_{dyn} is calculated for every set and the error is taken as the width of the ν_{dyn} -distribution. The number of events in all sets for one particular centrality bin equals the number of events used to calculate ν_{dyn} from data. Thus, this method assumes the dynamical fluctuations to be negligible in comparison with the statistical fluctuations. The comparison of the calculated and simulated errors in $\nu_{dyn}(K, \pi)$ and $\nu_{dyn}(p, \pi)$ shows a very good agreement, as can be seen in figure 8.15. The small deviation for peripheral events can be explained by the different constraints of the two methods.

A simpler empirical formula is tested in figure 8.16 assuming that the statistical error is proportional to

$$\nu = \nu_{dyn} + \nu_{stat} = \frac{\langle \pi^2 \rangle}{\langle \pi \rangle^2} + \frac{\langle K^2 \rangle}{\langle K \rangle^2} - 2 \frac{\langle \pi K \rangle}{\langle \pi \rangle \langle K \rangle} \quad (8.4)$$

divided by the square root of the number of events, N_{evt} . With a proportionality constant of 1.4 there is a good agreement between this empirical formula and the errors calculated using the analytical formula, with only slightly smaller errors obtained with the empirical formula for peripheral events.

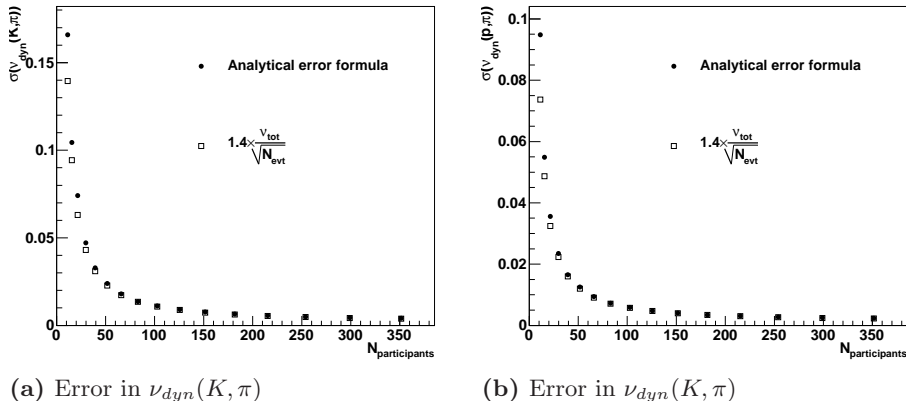


Figure 8.16: Comparison of the analytical error formula with an empirical formula over the full range of centrality bins, using a small subset of events.

8.6 Summary and outlook

In conclusion there is little room for dynamical fluctuations in the particle number ratios in Gold-Gold collisions at $\sqrt{s_{NN}} = 200$ GeV. Since noticeable fluctuations are expected from a phase transition, the results indicate a smooth cross-over at these collision energies.

The study of the observable ν_{dyn} clearly demonstrates how important it is to analyse charge combinations of different particle species separately in order to remove contributions from particle-antiparticle correlations. If there is a correlated production it is also useful to study ν_{dyn} at different rapidities and as a function of the width of the rapidity bin, as well as for varying azimuthal acceptance and momentum. This would provide information on the mechanism behind the fluctuations. The method can with advantage also be used in other situations like for example studies of forward-backward correlatations, where fluctuations between particles in two opposite regions of rapidity are studied as a function of an increasing rapidity gap.

The inclusive $\nu_{dyn}(K, \pi)$ of summed charges is consistent with results obtained by STAR [48] that are systematically lower by approximately a factor 1/3, which is not suprising considering that they measure in a lower range of momentum and their detector covers a much larger acceptance of 2π radians in azimuth and $|\eta| < 1$. Especially the difference in pseudorapidity coverage may be important for how frequently two particles in a decay are detected together. This may be the explanation for the fact that STAR, in contrast to what was found in this analysis, sees a small difference between like and unlike charge sign combinations of $\nu_{dyn}(K, \pi)$ over the full range

of centralities.

Searches for the critical point should be possible to conduct, selecting different regions of the phase diagram by varying the collision energy. I hope that our efforts to understand and clarify the method have contributed to this process.

Appendix A

Rapidity and pseudorapidity

The outline of rapidity and pseudorapidity below follows the one in appendix E of [4]. The rapidity, y , is defined

$$y \equiv \tanh^{-1}\beta = \frac{1}{2} \ln \frac{1+\beta}{1-\beta}, \quad (\text{A.1})$$

where $\beta \equiv v/c$, $v = v_z$ is the velocity along the z-axis and c is the speed of light. The rapidity is an analogue of the velocity along the z-axis since $y \simeq \beta$ for small β . The definition of rapidity is chosen because of its Lorentz invariance. The velocity or β are not linearly additive at relativistic velocities. Beta adds as

$$\beta = \frac{\beta_1 + \beta_2}{1 + \beta_1\beta_2} \quad (\text{A.2})$$

The rapidity then adds as

$$y = \frac{1}{2} \ln \frac{1 + \frac{\beta_1 + \beta_2}{1 + \beta_1\beta_2}}{1 - \frac{\beta_1 + \beta_2}{1 + \beta_1\beta_2}} = \frac{1}{2} \ln \frac{1 + \beta_1 + \beta_2 + \beta_1\beta_2}{1 - \beta_1 - \beta_2 + \beta_1\beta_2} = \frac{1}{2} \ln \frac{1 + \beta_1}{1 - \beta_1} + \frac{1}{2} \ln \frac{1 + \beta_2}{1 - \beta_2} \quad (\text{A.3})$$

so that $y = y_1 + y_2$ which is more convenient.

Often the expression for rapidity is rewritten using momentum, $\mathbf{p} = m\bar{v}c$, and energy, $E = mc^2$, instead of β as:

$$y = \frac{1}{2} \ln \frac{E + p_z}{E - p_z}, \quad (\text{A.4})$$

where $p_z = |\mathbf{p}|\cos\theta$ is the longitudinal momentum, i.e. the momentum component along the z-axis. The *transverse* momentum can also be defined as the momentum component in the plane transverse to the z-axis, $p_T = \sqrt{p_x^2 + p_y^2} = |\mathbf{p}|\sin\theta$. Then the transverse mass, m_T , is defined as

$$m_T^2 = p_T^2 + m^2, \quad (\text{A.5})$$

and the energy becomes

$$E^2 = p^2 + m^2 = p_z^2 + p_T^2 + m^2 = p_z^2 + m_T^2. \quad (\text{A.6})$$

Hence, the rapidity can also be written as $y = \ln \frac{E+p_z}{m_T}$, since

$$\ln \frac{E+p_z}{E-p_z} = \ln \frac{(E+p_z)^2}{E^2 - p_z^2} = \ln \frac{(E+p_z)^2}{m_T^2} = 2 \ln \frac{E+p_z}{m_T^2} \quad (\text{A.7})$$

The rapidity of a particle can only be computed if its mass is known, which is not trivially measured. Therefore a semi equivalent measure called the pseudo-rapidity, η , is defined using only the production angle of the particle:

$$\eta \equiv -\ln \left(\tan \frac{\theta}{2} \right). \quad (\text{A.8})$$

If the particle masses are negligible compared to the energies of the particles so that $E^2 = \mathbf{p}^2 + m^2 \approx \mathbf{p}^2$, the rapidity in equation A.4 reduces to the pseudorapidity since

$$\begin{aligned} y &= \frac{1}{2} \ln \left(\frac{E+p_z}{E-p_z} \right) = \frac{1}{2} \ln \left(\frac{1+\cos\theta}{1-\cos\theta} \right) = \frac{1}{2} \ln \left(\frac{2\cos^2\frac{\theta}{2}}{2\sin^2\frac{\theta}{2}} \right) \\ &= 2 \ln \left(\tan^{-2} \frac{\theta}{2} \right) = -\ln \left(\tan \frac{\theta}{2} \right) \end{aligned} \quad (\text{A.9})$$

Appendix B

Details of the particle identification

Distributions of mass squared, $m^2 - m_\pi^2$, $m^2 - m_K^2$ and $m^2 - m_p^2$, for the assumption that particles are pions, kaons and protons, respectively, with $m_\pi^2 = 0.019479785 \text{ GeV}^2/c^4$, $m_K^2 = 0.24371698 \text{ GeV}^2/c^4$ and $m_p^2 = 0.88035435 \text{ GeV}^2/c^4$ [1] are shown for 0.1 GeV/c wide bins in transverse momentum over the range used for particle identification for both EMCal and TOF. The filled area indicates the result of the momentum dependent $2\sigma_{m^2}$ including cut. Assymetries are due to the $3\sigma_{m^2}$ excluding cut from the other species. It should be remembered that the particle identification cuts were chosen tight in order to have as safe particle identification as possible. For this analysis a clean sample is favoured over a larger sample with poorer identification accuracy since average corrections can not be applied.

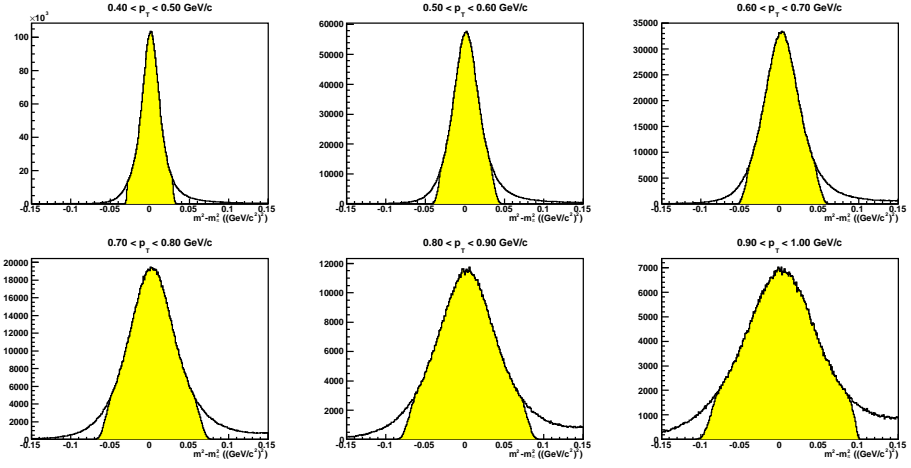


Figure B.1: Difference of m^2 to m_π^2 for positive charge in $0.4 < p_T < 1.0$ GeV/c, identified in the EMCal.

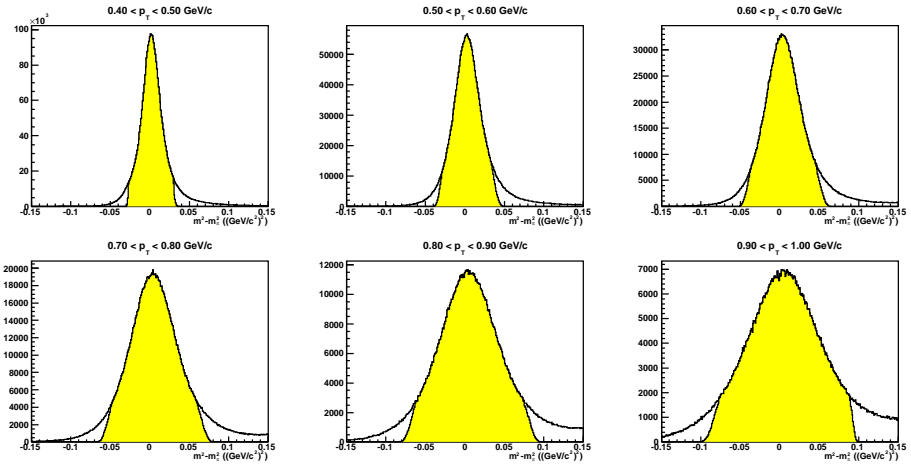


Figure B.2: Difference of m^2 to m_π^2 for negative charge in $0.4 < p_T < 1.0$ GeV/c, identified in the EMCal.

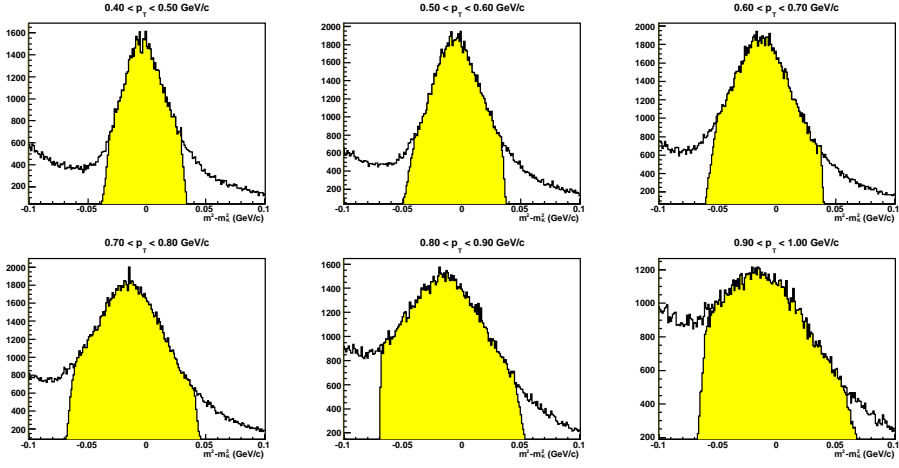


Figure B.3: Difference of m^2 to m_K^2 for positive charge in $0.4 < p_T < 1.0$ GeV/c, identified in the EMCal.

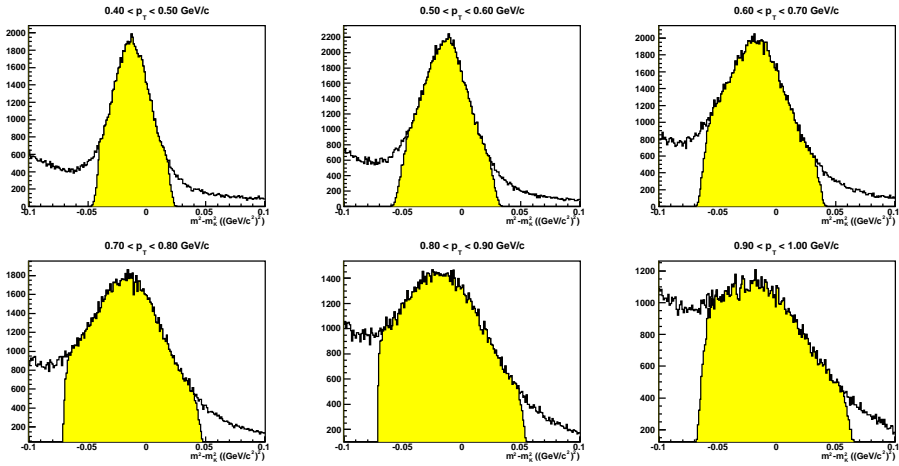


Figure B.4: Difference of m^2 to m_K^2 for negative charge in $0.4 < p_T < 1.0$ GeV/c, identified in the EMCal.

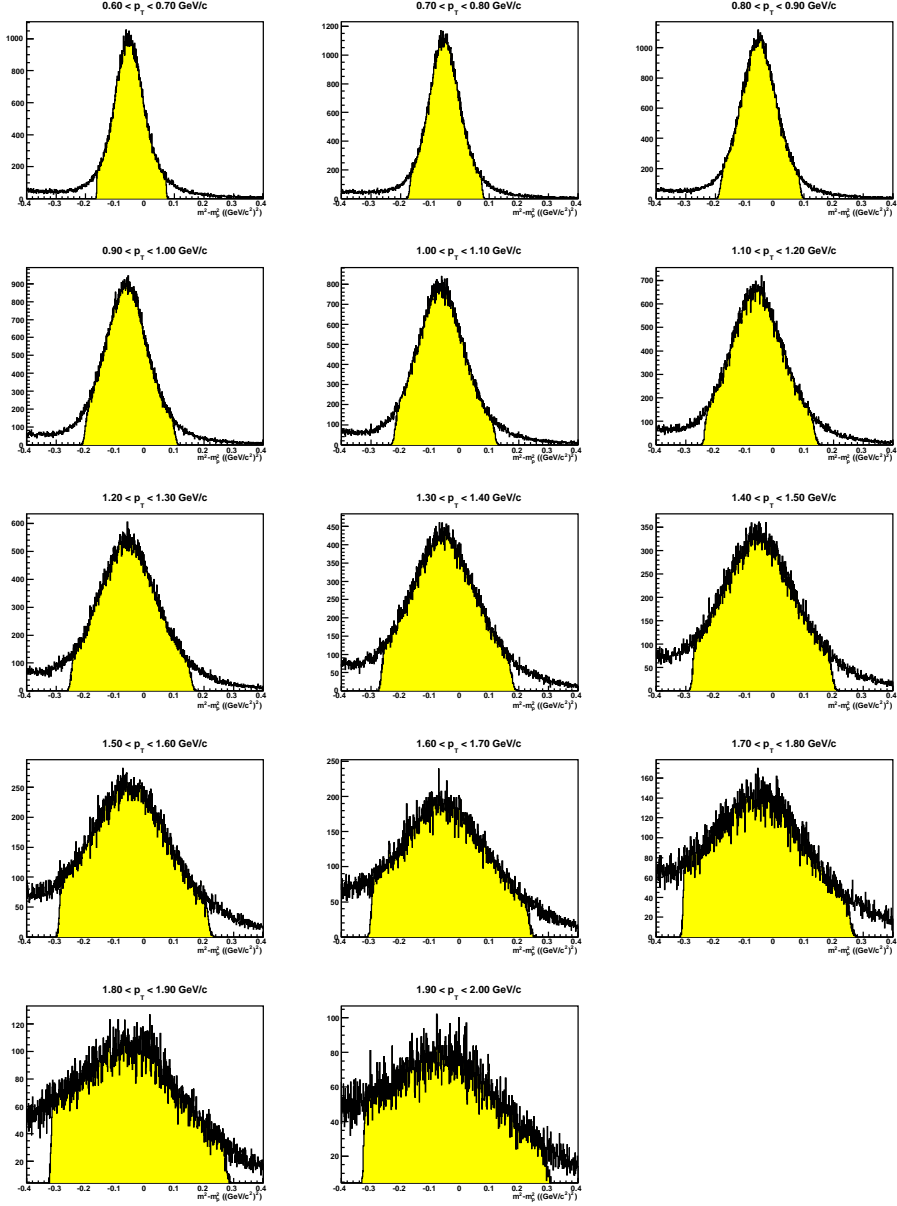


Figure B.5: Difference of m^2 to m_p^2 for positive charge in $0.6 < p_T < 2.0$ GeV/c, identified in the EMCAL.

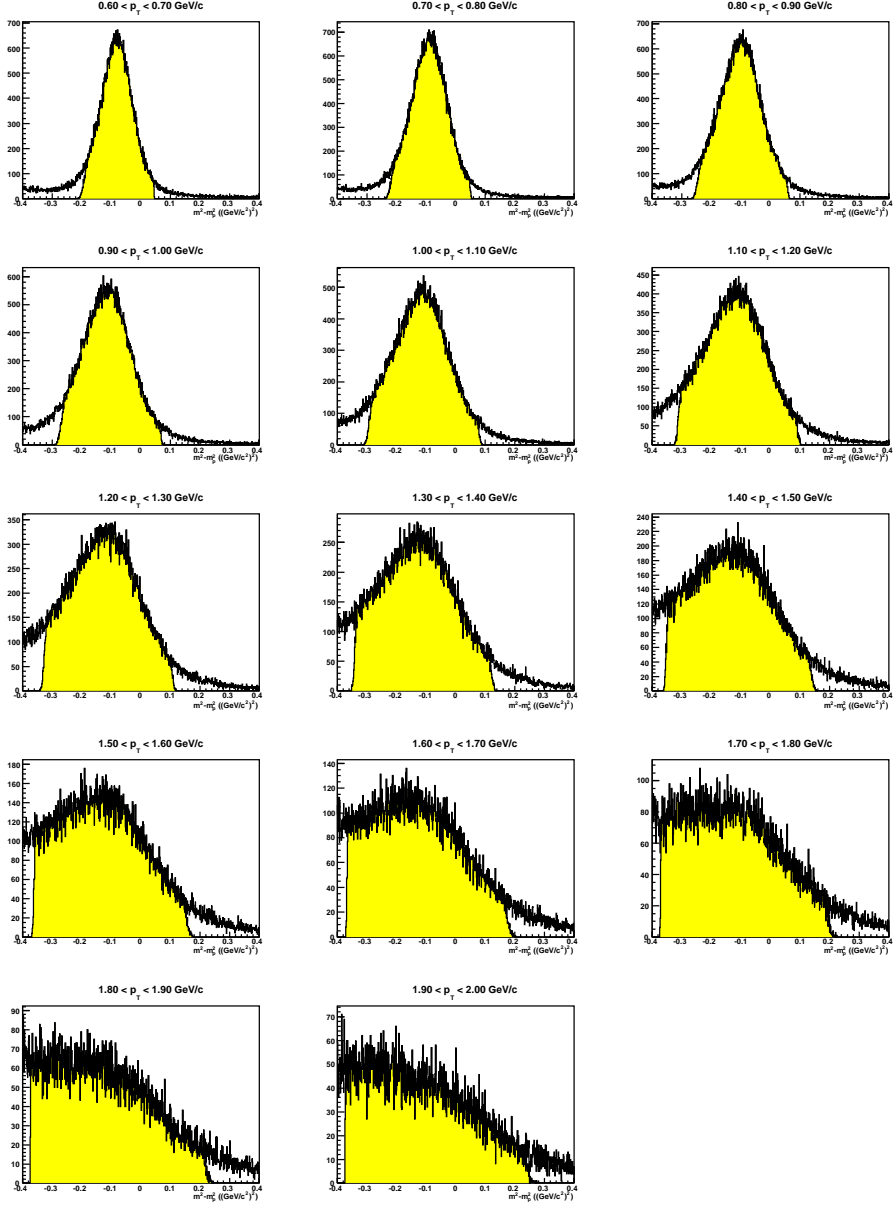


Figure B.6: Difference of m^2 to m_p^2 for negative charge in $0.6 < p_T < 2.0$ GeV/c, identified in the EMCAL.

Appendix C

Studies of track proximity

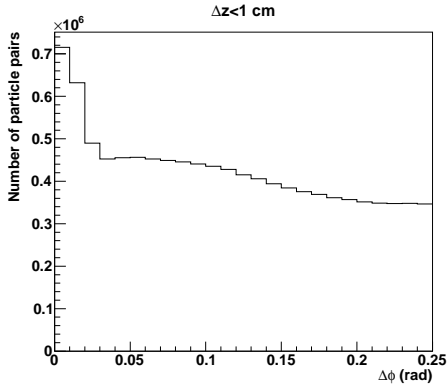
The following summarizes the results of an extensive study of track proximity in the detectors used for particle identification. Shown here are only track proximities in the azimuthal ϕ coordinate of the Drift Chamber, DC, and in the longitudinal z coordinate of the adjacent Pad Chamber layer, PC1, for tracks that pass all other track cuts and particle identification cuts. Track proximities in the outer Pad Chamber layers as well as in the Electromagnetic Calorimeter, EMCal (PbSc), and the Time-of-Flight, TOF, have also been studied but are not reported here since no additional cuts were applied on these parameters after rejecting all track pairs which are associated with the same EMCal cluster or TOF slat.

Figure C.1 shows the separation in ϕ in the Drift Chamber for track pairs with small z -proximity, $\Delta z < 1$ cm. Same sign pairs and opposite sign pairs are displayed separately. Clearly visible are the unphysical peaks at small $\Delta\phi$. For same signed tracks the peak appears between $0 < \Delta\phi < 0.02$ radians and for oppositely signed tracks between $0.02 < \Delta\phi < 0.06$ radians. For reference to the local dimensions at DC/PC1 one should note that the angular difference between two sense wire planes in the DC is about 0.02 radians which translates to 4.5cm at the DC reference radius.

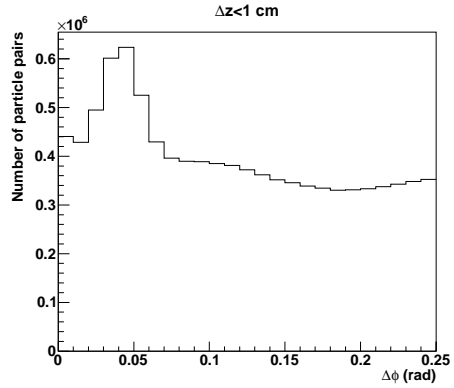
However, as can be seen in figure C.2 the peak away from zero is more prominent for tracks with a matching hit in the EMCal than for tracks with a matching hit in the TOF. Here the same momentum cut has been applied for both EMCal and TOF in order to obtain comparable results. The momentum range was selected to include all particle species.

The azimuthal proximity for track pairs at intermediate and larger longitudinal proximity is shown in figure C.3.

The longitudinal proximity is shown in figure C.4 for track pairs with $\Delta\phi$ inside and outside the peak region, respectively. This clearly shows that

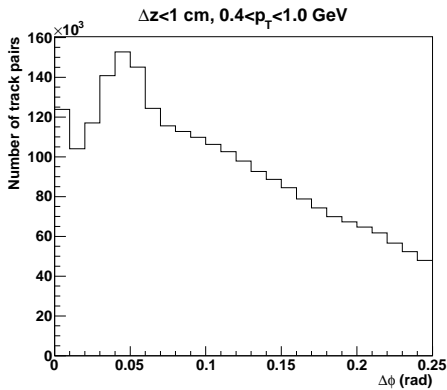


(a) Same charge sign

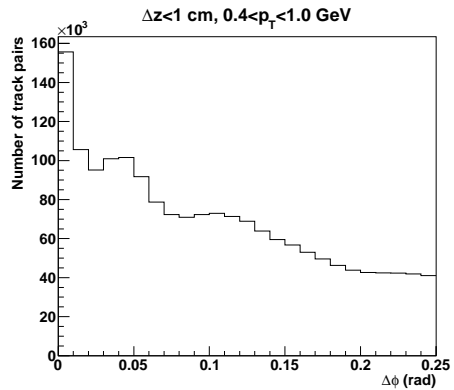


(b) Opposite charge sign

Figure C.1: Azimuthal proximity at small longitudinal proximity for tracks of same and opposite charge sign, respectively.



(a) EMCalPbSc sector 2W



(b) TOF sector 1E

Figure C.2: Difference in azimuthal proximity between tracks associated with EMCal sector 2 in the west arm and with the TOF sector for tracks at small longitudinal proximity in the 0-15% most central events.

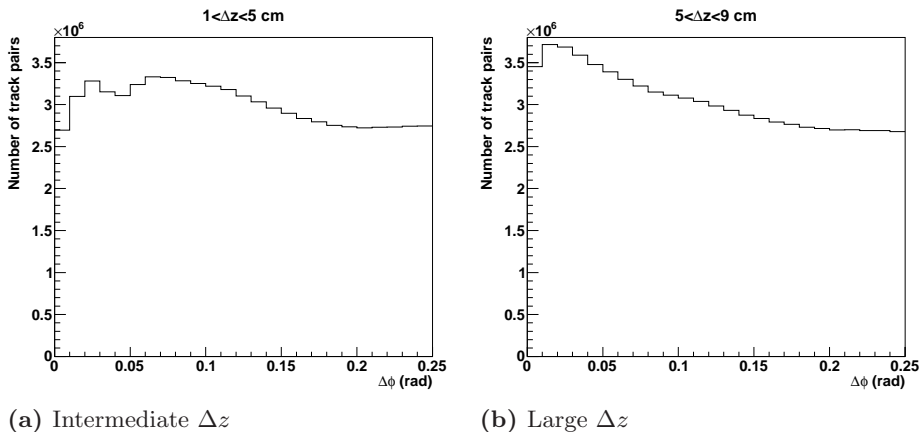


Figure C.3: Azimuthal proximity for track pairs with intermediate (a) and larger (b) longitudinal separation.

the dip at small Δz appears only behind the peaks.

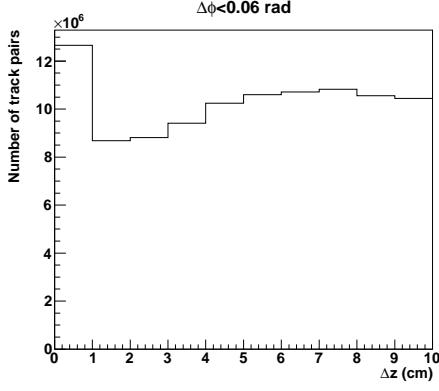
There is no direct relation between the spacial separation and the separation in momentum of the tracks. The double peak is persistent up to $\Delta p_T \simeq 0.5$ GeV as shown in figure C.5. In this context it has to be taken into account that the momentum range for kaons is much smaller than for protons and pions.

For the fluctuation analysis it is particularly problematic if nearby tracks affect the particle identification. Also, if the proximity is studied individually for pion, kaon and proton pairs as shown in figure C.6, it becomes apparent that the peaking structure for protons is different than for the other two species. A cut of $\Delta\phi > 0.06$ will remove the irregularities.

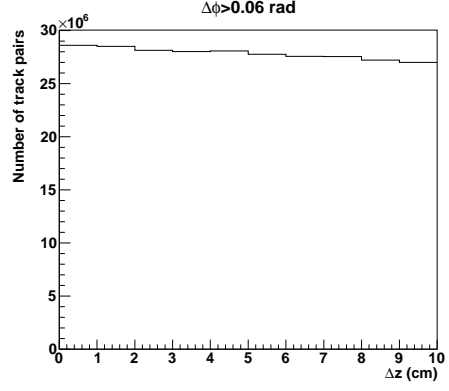
The variation of ratios of kaons-to-pions and protons-to-pions has been studied for varying track proximity. Given the multiplicity of particle pairs consisting of two kaons, $n_{pair}(KK)$, two pions $n_{pair}(\pi\pi)$ or a pion and a kaon, $n_{pair}(\pi K)$, the kaon-to-pion ratio is calculated as the number of kaons in a KK or $K\pi$ pair divided by the number of pions in a $\pi\pi$ or πK pair as given by equation C.1. The reason for calculating the ratio in this way is that the particle pairs are counted in the proximity bins rather than individual particles.

$$\frac{\langle K \rangle}{\langle \pi \rangle} = \frac{2n_{pair}(KK) + n_{pair}(\pi K)}{2n_{pair}(\pi\pi) + n_{pair}(\pi K)} \quad (C.1)$$

and equivalently for the proton-to-pion ratio. Figures C.7 shows particle ratios as a function of longitudinal proximity of two particles, both for particle pairs with a small azimuthal proximity inside the peak region,

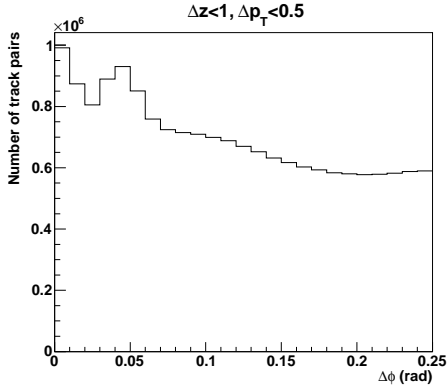


(a) Smaller $\Delta\phi$

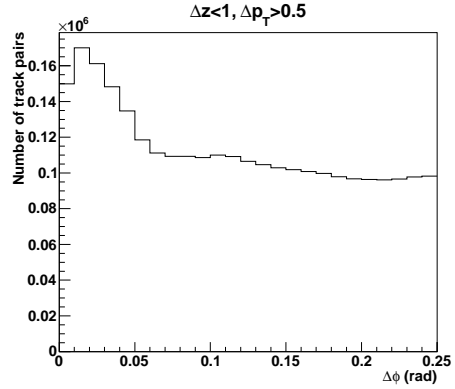


(b) Larger $\Delta\phi$

Figure C.4: Longitudinal proximity for track pairs with small (a) and larger (b) separation in ϕ .



(a) Smaller Δp_T



(b) Larger Δp_T

Figure C.5: Dependence of $\Delta\phi$ on the separation in momentum of the track pairs.

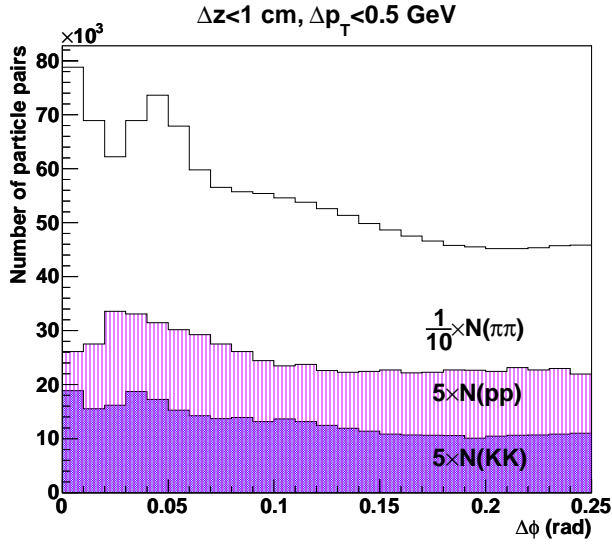
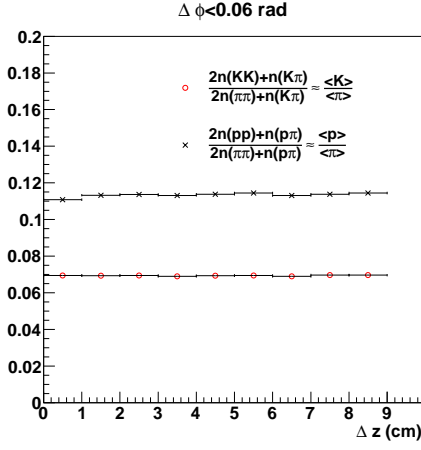


Figure C.6: Azimuthal proximity for pion, kaon and proton pairs, respectively.

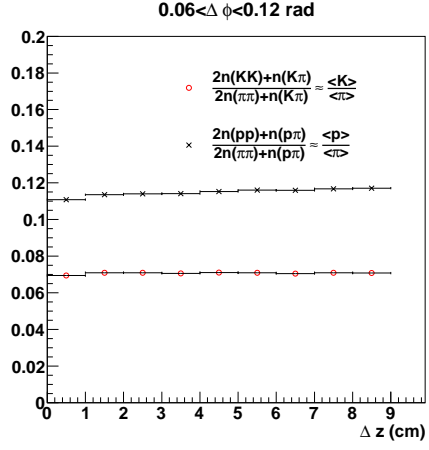
$\Delta\phi < 0.06$ rad, and for particle pairs with larger azimuthal proximity outside the peak region, $0.06 < \Delta\phi < 0.12$ rad.

Figure C.8 shows the ratios as a function of azimuthal proximity of two particles, both for particle pairs with a small longitudinal proximity inside the peak region, $\Delta z < 1$ cm, and for particle pairs with larger longitudinal proximity outside the peak region, $1 < \Delta z < 2$ cm.

Neither the peak regions nor the valley regions deviate from the surrounding regions to any significant extent.

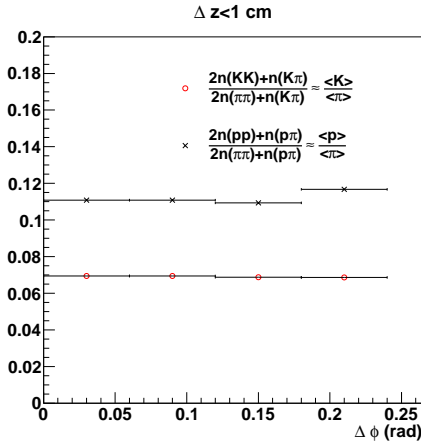


(a) In region of anomalous $\Delta\phi$

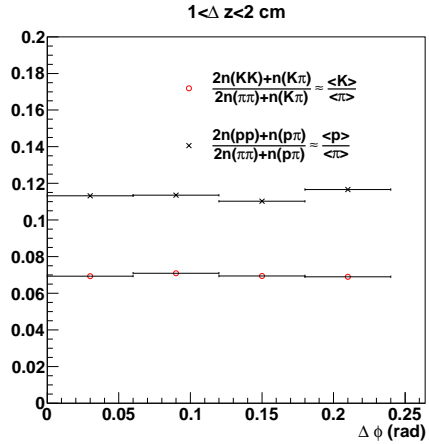


(b) Outside region of anomalous $\Delta\phi$

Figure C.7: K -to- π and p -to- π ratio as a function of longitudinal proximity. No error bars are plotted.



(a) In region of anomalous Δz



(b) Outside region of anomalous Δz

Figure C.8: K -to- π and p -to- π as a function of azimuthal proximity. No error bars are plotted.

Appendix D

Statistical error in ν_{dyn}

$$\sigma(\nu_{\text{dyn}}) = \sqrt{V[\nu_{\text{dyn}}]}$$

where, for $n = K, p$ and $m = \pi$, the variance V is calculated as:

$$\begin{aligned} V[\nu_{\text{dyn}}] = & \frac{1}{N} \frac{1}{\langle n \rangle^6 \langle m \rangle^6} \left[6 \langle n^2 m^2 \rangle \langle n \rangle^4 \langle m \rangle^4 - 4 \langle n^3 m \rangle \langle n \rangle^3 \langle m \rangle^5 - 4 \langle n m^3 \rangle \langle n \rangle^5 \langle m \rangle^3 \right. \\ & + 8 \langle n^2 m \rangle \langle n^2 \rangle \langle n \rangle^2 \langle m \rangle^5 + 8 \langle n m^2 \rangle \langle m^2 \rangle \langle n \rangle^5 \langle m \rangle^2 - 4 \langle n^2 m \rangle \langle n m \rangle \langle n \rangle^3 \langle m \rangle^4 \\ & - 4 \langle n m^2 \rangle \langle n m \rangle \langle n \rangle^4 \langle m \rangle^3 - 4 \langle n^2 m \rangle \langle m^2 \rangle \langle n \rangle^4 \langle m \rangle^3 - 4 \langle n m^2 \rangle \langle n^2 \rangle \langle n \rangle^3 \langle m \rangle^4 \\ & + 8 \langle n m \rangle^3 \langle n \rangle^3 \langle m \rangle^3 - 4 \langle n m \rangle^2 \langle n^2 \rangle \langle n \rangle^2 \langle m \rangle^4 - 4 \langle n m \rangle^2 \langle m^2 \rangle \langle m \rangle^2 \langle n \rangle^4 \\ & - 4 \langle n m \rangle^2 \langle n \rangle^4 \langle m \rangle^4 + 4 \langle n m \rangle \langle n^3 \rangle \langle n \rangle^2 \langle m \rangle^5 + 4 \langle n m \rangle \langle m^3 \rangle \langle m \rangle^2 \langle n \rangle^5 \\ & - 8 \langle n m \rangle \langle n^2 \rangle^2 \langle n \rangle \langle m \rangle^5 - 8 \langle n m \rangle \langle m^2 \rangle^2 \langle m \rangle \langle n \rangle^5 + 8 \langle n m \rangle \langle n^2 \rangle \langle m^2 \rangle \langle n \rangle^3 \langle m \rangle^3 \\ & + 4 \langle n m \rangle \langle n^2 \rangle \langle n \rangle^3 \langle m \rangle^5 + 4 \langle n m \rangle \langle m^2 \rangle \langle m \rangle^3 \langle n \rangle^5 + \langle n^4 \rangle \langle n \rangle^2 \langle m \rangle^6 \\ & + \langle m^4 \rangle \langle m \rangle^2 \langle n \rangle^6 - 4 \langle n^3 \rangle \langle n^2 \rangle \langle n \rangle \langle m \rangle^6 - 4 \langle m^3 \rangle \langle m^2 \rangle \langle m \rangle \langle n \rangle^6 \\ & + 4 \langle n^2 \rangle^3 \langle m \rangle^6 + 4 \langle m^2 \rangle^3 \langle n \rangle^6 - \langle n^2 \rangle^2 \langle n \rangle^2 \langle m \rangle^6 - \langle m^2 \rangle^2 \langle m \rangle^2 \langle n \rangle^6 \\ & - 2 \langle n^2 \rangle \langle m^2 \rangle \langle n \rangle^4 \langle m \rangle^4 + 2 \langle n^2 m \rangle \langle n \rangle^4 \langle m \rangle^4 + 2 \langle m^2 n \rangle \langle n \rangle^4 \langle m \rangle^4 \\ & - 4 \langle n^2 m \rangle \langle n \rangle^3 \langle m \rangle^5 - 4 \langle m^2 n \rangle \langle m \rangle^3 \langle n \rangle^5 + 4 \langle n m \rangle^2 \langle n \rangle^4 \langle m \rangle^3 \\ & + 4 \langle n m \rangle^2 \langle m \rangle^4 \langle n \rangle^3 - 4 \langle n m \rangle \langle n^2 \rangle \langle n \rangle^3 \langle m \rangle^4 - 4 \langle n m \rangle \langle m^2 \rangle \langle m \rangle^3 \langle n \rangle^4 \\ & + 4 \langle n m \rangle \langle n^2 \rangle \langle n \rangle^2 \langle m \rangle^5 + 4 \langle n m \rangle \langle m^2 \rangle \langle m \rangle^2 \langle n \rangle^5 - 4 \langle n m \rangle \langle n \rangle^5 \langle m \rangle^4 \\ & - 4 \langle n m \rangle \langle m \rangle^5 \langle n \rangle^4 + 2 \langle n^3 \rangle \langle n \rangle^2 \langle m \rangle^6 + 2 \langle m^3 \rangle \langle m \rangle^2 \langle n \rangle^6 \\ & - 4 \langle n^2 \rangle^2 \langle n \rangle \langle m \rangle^6 - 4 \langle m^2 \rangle^2 \langle m \rangle \langle n \rangle^6 + 2 \langle n^2 \rangle \langle n \rangle^4 \langle m \rangle^5 \\ & + 2 \langle m^2 \rangle \langle m \rangle^4 \langle n \rangle^5 + 2 \langle n^2 \rangle \langle n \rangle^3 \langle m \rangle^6 + 2 \langle m^2 \rangle \langle m \rangle^3 \langle n \rangle^6 \\ & + 2 \langle n m \rangle \langle n \rangle^4 \langle m \rangle^4 + \langle n^2 \rangle \langle n \rangle^2 \langle m \rangle^6 + \langle m^2 \rangle \langle m \rangle^2 \langle n \rangle^6 \\ & \left. - \langle n \rangle^6 \langle m \rangle^4 - \langle m \rangle^6 \langle n \rangle^4 - 2 \langle n \rangle^5 \langle m \rangle^5 \right] + O\left(\frac{1}{N^2}\right) \end{aligned}$$

References

- [1] K. Nakamura et al. (Particle Data Group), J. Phys. G 37 (2010) 075021
- [2] G. Bertone, D. Hooper, J. Silk, *Particle Dark Matter: Evidence, Candidates and Constraints*, Phys. Rept. 405 (2005) 279-390
- [3] J. Lesgourgues, S. Pastor, *Massive neutrinos and cosmology*, Phys. Rept. 429 (2006) 307-379
- [4] K. Yagi, T. Hatsuda, Y. Miake, *Quark Gluon Plasma*, Cambridge Monographs on Particle Physics, Nuclear Physics and Cosmology (2005)
- [5] I. Meshkov, *Status of NICA project*, CPOD2010
- [6] V. Friese, *The CBM Experiment - a status report*, CPOD2010
- [7] E. Kornasa for the NA49 Collaboration, Eur. Phys. J. C 49, (2007) 293296
- [8] K. Aamodt et al. (ALICE Collaboration), *Midrapidity Antiproton-to-Proton Ratio in pp Collisions at $s=0.9$ and 7 TeV Measured by the ALICE Experiment*, Phys. Rev. Lett. 105, 072002 (2010)
- [9] M. Kaneta, N. Xu, *Centrality Dependence of Chemical Freeze-out in Au+Au Collisions at RHIC*, nucl-th/0405068
- [10] T. Atsui, H. Satz, *J/ψ suppression by quark-gluon plasma formation*, Phys. Lett. B178 (1986) 416
- [11] R.L. Thews, M. Schroedter, J. Rafelski, *Enhanced J/ψ production in deconfined quark matter*, Phys. Rev. C63 (2001) 054905
- [12] STAR Collaboration, *Experimental and theoretical challenges in the search for the quark-gluon plasma: The STAR Collaboration's critical assessment of the evidence from RHIC collisions*, Nucl. Phys. A757 (2005) 102-183
- [13] PHENIX Collaboration, S. S. Adler et al., *Common Suppression Pattern of eta and pi0 Mesons at High Transverse Momentum in Au+Au Collisions at $\sqrt{s_{NN}} = 200$ GeV*, Phys. Rev. Lett. 96 (2006) 202301

- [14] PHENIX Collaboration, *Formation of dense partonic matter in relativistic nucleus-nucleus collisions at RHIC: Experimental evaluation by the PHENIX Collaboration*, Nucl. Phys. A757 (2005) 184-283
- [15] PHENIX Collaboration, S. S. Adler et al., *Identified Charged Particle Spectra and Yields in Au+Au Collisions at $\sqrt{s_{NN}} = 200$ GeV*, Phys. Rev. C 69 (2004) 034909
- [16] PHENIX Collaboration, A. Adare et al., *Scaling properties of azimuthal anisotropy in Au+Au and Cu+Cu collisions at $\sqrt{s_{NN}} = 200$ GeV*, Phys. Rev. Lett. 98 (2007) 162301
- [17] PHENIX Collaboration, A. Adare et al., *Detailed measurement of the $e+e^-$ pair continuum in $p+p$ and Au+Au collisions at $\sqrt{s_{NN}}=200$ GeV and implications for direct photon production*, Phys. Rev. C 81 (2010) 034911
- [18] PHENIX Collaboration, A. Adare et al., *Dihadron azimuthal correlations in Au+Au collisions at $\sqrt{s_{NN}} = 200$ GeV*, Phys. Rev. C 78 (2007) 014901
- [19] *The PHENIX Experiment at RHIC, Decadal Plan 2011–2020*, available from <http://www.phenix.bnl.gov/plans.html>
- [20] *RHIC Design Manual*, electronic version available online from <http://www.bnl.gov/cad/accelerator/>
- [21] M. Harrison, T. Ludlam, S. Ozaki, *RHIC project overview*, NIM A499, 235-244 (2003)
- [22] PHENIX Collaboration, M. Allen et al., *PHENIX Inner Detectors*, NIM A499 549-592 (2003)
- [23] PHENIX Collaboration, C. Adler et al., *The RHIC zero degree calorimeters*, NIM A470 488-499 (2001)
- [24] PHENIX Collaboration, K. Adcox et al., *PHENIX Central Arm Tracking Detectors*, NIM A499 489-507 (2003)
- [25] PHENIX Collaboration, S.H. Aronson et al., *PHENIX Magnet System*, NIM A499 480-488 (2003)
- [26] 2D TOSCA simulation done by Walt Sondheim, LANL
- [27] PHENIX Collaboration, M. Aizawa et al., *PHENIX Central Arm Particle ID Detectors*, NIM A499 508-520 (2003)
- [28] PHENIX Collaboration, L. Aphecetche et al., *PHENIX Calorimeter*, NIM A499 521-536 (2003)

- [29] PHENIX Collaboration, J. T. Mitchell et al., *Event reconstruction in the PHENIX central arm spectrometers*, NIM A482 491-512 (2002)
- [30] Private communication from E. Stenlund
- [31] PHENIX Collaboration, S.S. Adler et al., *Systematic studies of the centrality and $\sqrt{s_{NN}}$ dependence of the $dE_T/d\eta$ and $dN_{ch}/d\eta$ in heavy ion collisions at midrapidity*, Phys. Rev. C71 (2005) 034908; 049990(Errata)
- [32] M. L. Miller, K. Reygers, S. J. Sanders and P. Steinberg, *Glauber Modeling in High Energy Nuclear Collisions*, Annu. Rev. Nucl. Part. Sci. 57 (2007) 205
- [33] COBE web page <http://lambda.gsfc.nasa.gov/product/cobe/>
- [34] U. Heinz, B.V. Jacak, *Two-Particle Correlations In Relativistic Heavy-Ion Collisions*, Annu. Rev. Nucl. Part. Sci. 49 (1999) 529-579, and references therein.
- [35] S. Jeon, V. Koch, *Event by event fluctuations*, hep-ph/0304012, Review for "Quark-Gluon Plasma 3", Eds. R.C. Hwa, X.-N. Wang, World Scientific, Singapore (2004)
- [36] H. Heiselberg, *Event-by-event physics in relativistic heavy-ion collisions*, Phys. Rep. 351 (2001) 161-194
- [37] Bowley, Sanchez, *Introductory Statistical Mechanics, 2nd ed.*, Oxford 1999
- [38] M. Asakawa, U. Heinz, B. Müller, *Fluctuation Probes of Quark Deconfinement*, Phys. Rev. Lett. 85 (2000) 2072
- [39] S. Jeon, V. Koch, *Charged Particle Ratio Fluctuation as a Signal for Quark-Gluon Plasma*, Phys. Rev. Lett. 85 (2000) 2076
- [40] H. Heiselberg, A.D. Jackson, *Anomalous multiplicity fluctuations from phase transitions in heavy-ion collisions*, Phys. Rev. C63 (2001) 064904
- [41] PHENIX Collaboration, K. Adcox et al., *Net Charge Fluctuations in Au+Au Interactions at $\sqrt{s_{NN}} = 130$ GeV*, Phys. Rev. Lett. 89 (2002) 082301
- [42] A. Bialas, M. Bleszynski, *Multiplicity distributions in nucleus-nucleus collisions at high energies*, W. Czyz, Nucl. Phys. B111 (1976) 461
- [43] R. Korus, St. Mrowczynski, M. Rybczynski, Z. Wlodarczyk, *Transverse momentum fluctuations due to temperature variation in high-energy nuclear collisions*, Phys. Rev. C64 (2001) 054908

- [44] PHENIX Collaboration, S.S. Adler et al., *Measurement of Nonrandom Event-by-Event Fluctuations of Average Transverse Momentum in $\sqrt{s_{NN}} = 200$ GeV Au+Au and p+p Collisions*, Phys. Rev. Lett. 93 (2004) 092301
- [45] PHENIX Collaboration, A. Adare et al., *Charged hadron multiplicity fluctuations in Au+Au and Cu+Cu collisions from $\sqrt{s_{NN}}=22.5$ to 200 GeV*, Phys. Rev. C 78, 044902 (2008)
- [46] C. Roland et al. *Event-by-event Fluctuations of Particle Ratios in Central Pb+Pb Collisions at 20 to 158 AGeV*, J. Phys. G30 (2004) S1381-S1384
- [47] S. Das (for the STAR Collaboration) *Event by Event fluctuations in K/ π ratio at RHIC*, nucl-ex/0503023
- [48] B. I. Abelev et al. STAR Collaboration, *K/ π Fluctuations at Relativistic Energies*, Phys. Rev. Lett. 103 (2009) 092301
- [49] C. Pruneau, S. Gavin, S. Voloshin, *Methods for the study of particle production fluctuations*, Phys. Rev. C66 (2002) 044904
- [50] P. Christiansen, E. Haslum, E. Stenlund, *Number-ratio fluctuations in high-energy particle production*, Phys. Rev. C80 (2009) 034903
- [51] R. Brun, F. Rademakers, *ROOT - An Object Oriented Data Analysis Framework*, Nucl. Inst. Meth. in Phys. Res. A 389 (1997) 81-86. See also <http://root.cern.ch/>
- [52] M. Matsumoto, T. Nishimura, *Mersenne Twister: A 623-dimensionally equidistributed uniform pseudo-random number generator*, ACM Transactions on Modeling and Computer Simulation: Special Issue on Uniform Random Number Generation, Vol. 8, No. 1, January 1998, pp. 3-30.
- [53] XN Wang, M. Gyulassy, *code HIJING 1.383*, Phys. Rev. D 44 (1991) 3501
- [54] GEANT, CERN Program Library Long Writeup W5013, 1994.
- [55] T. Sjostrand, S. Mrenna, P. Skands, *PYTHIA 6.4 Physics and Manual*, JHEP 0605:026 (2006)
- [56] T. Sjöstrand, *The Lund Monte Carlo for jet fragmentation and e+e- physics - jetset version 6.2*, Comput. Phys. Commun. 39 (1986), 347
- [57] TW. Ludlam, A. Pfoh, A. Shor, *HIJET. A Monte Carlo Event Generator for P Nucleus and Nucleus Nucleus Collisions*. Brookhaven Natl. Lab. Tech. Rep. BNL- 51921, Brookhaven Natl. Lab., Upton, N.Y. (1985)

Paper I

Number-ratio fluctuations in high-energy particle production

P. Christiansen, E. Haslum and E Stenlund

Published in PHYSICAL REVIEW C **80**, 034903 (2009)